Monolithic Dual-Wavelength InP/AlGaInP Quantum Dot Lasers

Samuel Shutts

PhD Thesis

School of Physics and Astronomy

Cardiff University

September 2012

DECLARATION

This work has not been submitted in substance for any other degree or award at this or any other university or place of learning, nor is being submitted concurrently in candidature for any degree or other award.

Signed …… (candidate) Date ……

STATEMENT 1

This thesis is being submitted in partial fulfilment of the requirements for the degree of PhD.

Signed …… (candidate) Date ……

STATEMENT 2

This thesis is the result of my own independent work/investigation, except where otherwise stated. Other sources are acknowledged by explicit references. The views expressed are my own.

Signed …… (candidate) Date ……

STATEMENT 3

I hereby give consent for my thesis, if accepted, to be available for photocopying and for inter-library loan, and for the title and summary to be made available to outside organisations.

Signed …… (candidate) Date ……

STATEMENT 4: PREVIOUSLY APPROVED BAR ON ACCESS

I hereby give consent for my thesis, if accepted, to be available for photocopying and for inter-library loans after expiry of a bar on access previously approved by the Academic Standards & Quality Committee.

Signed …… (candidate) Date ……

Abstract

This thesis describes the development of a monolithic dual-wavelength laser based on an InP/AlGaInP quantum dot (QD) laser structure. Each wavelength is sourced from the same active region and can be operated simultaneously or independently, with light being emitted from a common aperture. The inhomogeneity of the QD material provides a wide distribution of energies, resulting in a broad and relatively flat-topped gain spectrum, which is ideal for sourcing multiple wavelengths. Measurements of optical absorption, gain and laser threshold current densities were used to characterise the optical properties of InP/AlGaInP QDs and ascertain a suitable structure from which to fabricate the dual-wavelength source.

A growth temperature of 710 °C resulted in the lowest threshold current densities, and the incorporation of tensile strain into the upper confining layers was found to reduce the temperature dependence. Optical gain measurements were used to assess how state-filling and temperature govern the gain-peak wavelength. For a fixed gain at low injection the wavelength dependence follows that of the band gap (≈ 0.17 nm/K), but at higher levels of injection it becomes relatively temperature-insensitive. A minima in wavelength sensitivity corresponded to a net gain of ≈ 28 cm^{-1}. Edge-emitting lasers with a wavelength temperature dependence as low as 0.03 nm/K were demonstrated for temperatures up to 107 °C (380 K).

An Ar-Cl_2 based inductively-coupled plasma (ICP) etch process, suitable for fabricating sub-micron features, was developed to create the necessary device architecture. Using the effects of state-filling and spectrally preferential feedback, coupled-cavity ridge-waveguide lasers with unequal length sections were used to generate two wavelengths, with separations up to 61.5 ± 0.2 nm. Time resolved spectra were used to demonstrate dual-mode operation, where both wavelengths were observed to emit simultaneously. This is a promising result as it suggests that this device could potentially be used as a compact terahertz source.

Acknowledgement

Firstly, I would like to thank my supervisor Peter Smowton for taking me on as a PhD student, the experience has been thoroughly rewarding. The support, advice and general guidance throughout this project has been greatly appreciated. I would also like to thank Peter Blood for generating enthusiasm and fuelling insightful Friday morning discussions.

I would like to mention the people who shared my 'second home' - the cleanroom. Foremost, I must thank Gareth Edwards for his patience and passing on knowledge in the quirks of the Raith50 and idiosyncrasies of the ICP. I'm also grateful of the support and knowledge of Angela Sobiesierski, Chris Dunscombe, Dave Westwood, Karen Barnett, Steven Baker, Rob Tucker for his electronic expertise, and Hugh Lang for his ability to fix equipment at a seconds notice.

Thanks to other members of the Photons and Matter group, especially Rob Thomas, Stella Elliot and for their social antics, Ian O'driscoll and Matthew Hutchings.

Finally, a special thanks to my friends and family for their encouragement and unconditional support. Particularly my parents, for providing a retreat from the PhD and distracting me with endless jobs!

Contents

Chapter 1. Introduction

1.1. Thesis Rationale

Since the invention of the double-heterostructure and the incorporation of quantum confined structures to localise carriers in an injection semiconductor laser, there has been a flurry of device optimisation. Pioneering work in epitaxial growth techniques has been pivotal in improving material quality and has permitted the fabrication of nanoscale regions where carriers can be confined for efficient generation of photons. Formation of 'self assembled' quantum dots (QD)s was first achieved using a Stranski-Krastanov growth mode, where InAs QD clusters were formed in a GaAs matrix by a *strained-layer heteroepitaxy* process [Goldstein et al. 1985]. Since then many other QD material systems have been grown with the principal interest to establish whether the advantages of quantum confinement in three dimensions could be realised.

Research interest has shifted slightly in recent years, from the fundamental concepts, to the exploitation of laser diodes, generating a plethora of technological applications, ranging from bio-medical diagnostics to ultra-fast telecommunications. The most mature of the QD lasers are those formed from 1.3 - 1.6 µm emitting InAs/GaAs, where extensive research was stimulated by the technological demands of the telecommunication industry.

More recently, InP-based QDs have encroached on a wavelength regime that extends from 650 nm to 750nm, extending the upper limits of compressively strained GaInP quantum well lasers. Early developments on InP-GaInP QDs grown by solid-source molecular beam epitaxy (SSMBE), reported threshold current densities of 2.3 $kAcm^{-2}$ for 2 mm long devices emitting at 728 nm [Manz et al. 2000]. Devices grown by metal-organic vapour phase epitaxy (MOVPE), operating at a shorter wavelength of 645 nm, were reported for 200 µm long cavities with threshold currents of 4.25 $kAcm^{-2}$ [Walter et al. 2004]. These current densities were much higher than those achieved with InAs QDs, which around that time, were as low as 26 Acm^{-2} [Liu et al. 1999]. It was later

realised that the shortcoming of InP QD lasers was related to the growth parameters, namely the temperature [Krysa et al. 2007]. Previous MOVPE growth runs were carried out at temperatures between 580 and 650 °C; increasing this to the region of 700 °C vastly improved the material quality and as a result 2 mm long lasers emitting at 741 nm were fabricated with record low threshold currents of 190 Acm^{-2} at 300 K [Smowton et al. 2005]. The aim of part of this PhD, was to understand how the growth temperature affects the nature of the dot formation. In addition, studies have revealed how the width of the barrier layer separating each dot layer can affect device performance and how the incorporation of strain in the upper confining layers can reduce the threshold current temperature dependence [Smowton et al. 2010; Elliott et al. 2012]. To date, threshold current densities as low as 145 Acm^{-2} have been achieved for 2 mm long lasers. With improvements in performance these sources are becoming attractive for biomedical uses, since this wavelength regime minimises the scattering, absorption and auto-fluorescence of bio-substrates. Such applications include activation of photosensitizers used in Photodynamic Therapy (PDT) for the treatment of certain cancers, and excitation of fluorescent dyes used in imaging and diagnostics via bio-conjugation.

Growth by self assembly inherently gives rise to a fluctuation in dot size and as such the energy states of the ensemble are *inhomogeneously broadened*. Although not desirable in all respects, it means that optical gain can be achieved over a relatively large spectral range, and this discloses a fruitful array of device applications. For example, a broad gain spectrum can be used to generate ultra-short light pulses from mode-locked lasers [Kuntz et al. 2007] or source multiple wavelengths, by using the appropriate feedback mechanisms. The latter, specifically when applied to the concept of a dual-wavelength lasers was the aim of this PhD and forms the crux of the thesis. Various methods have been employed to generate multi-wavelength sources and this was enthused by a wealth of technological applications including wavelength division multiplexing, CD and DVD read-write compatibility and in more recent years, the potential to generate terahertz radiation. Device architectures vary; there are those which consist of: two independent in-plane sources; to Y-branch surface etched lasers

[Price et al. 2007]; multi-section devices incorporating distributed Bragg reflectors (DBR)s [Roh et al. 1999]; lateral coupled distributed feedback LC-DFB lasers [Pozzi, et al. 2006]; VCSELs formed from intermixing active layers of GaInP (red) and AlGaAs (Infra-red) [Thomas L. Paoli, 1997]; and devices which make use of external cavities to switch wavelengths [Daghestani et al. 2011]. There are advantages to all of these devices, but from a technological stand-point the device should be stable in operation, emit both wavelengths from a common aperture, be compact and inexpensive to fabricate.

There have been several reports of using dual-wavelength diode lasers as a means to generate terahertz emission. Methods include *difference frequency generation* (DFG) for example parametric frequency conversion in non-linear crystals [Scheller et al. 2010] and photo-mixing in photo-conductive antennas [Matsuura et al. 1997; Tanoto et al. 2012]. Other sources include *quantum cascade lasers* (QCLs) [Kumar et al. 2011], however these must be cryogenically cooled which increases cost and footprint. The advantage of using single diode lasers operating on two modes mitigates the problem of alignment issues and a drifting beat-note which can occur when using two separate lasers [O'Brien et al. 2010].

Dual-wavelength sources are also attracting attention for biomedical applications, and as stated above, they are of particular interest when operating at the emission wavelengths encompassed by InP QDs. Techniques such as *laser speckle contrast imaging* (LSI) and *2D photo-acoustic imaging* use pulsed dual-wavelength lasers to study multiple vascular physiological parameters such as concentration of haemoglobin, blood flow and oxygen saturation [Qin et al, 2012; Allen et al 2007]. Treatment or eradication of leg veins has also been shown to be more successful when using two wavelengths [Sadick, 2002].

The nature of QDs (namely the broad gain-spectra and the fast carrier dynamics), lends itself as a suitable active material for dual-wavelength lasers and these traits have already been exploited in an InAs based material system [Naderi et al. 2010; Daghestani et al. 2011]. In these devices dual-mode operation typically comes from the

ground and first excited state transitions. InP/AlGaInP QD laser structures exhibit a gain spectrum which is not only broad but also relatively flat-topped, due to the wide distribution of energy states. The advantages of this are two-fold: not only does it allow access to a large range of wavelengths, it also reduces the temperature dependence of the threshold current in devices which provide spectrally preferential feedback (e.g. DBRs and DFBs).

The ability to etch anisotropic features is pivotal in achieving the device architectures anticipated in this thesis. Developing an etch recipe for InP/AlGaInP using an inductively coupled plasma (ICP) source was a key focus of this project. The need to etch sub-micron high aspect ratio features is also becoming increasingly important with the movement towards 'lab on a chip' type devices and photonic interconnects such as those envisaged in the field of silicon photonics. The etching of photonic structures draws on another favourable aspect of QDs, in that the non-radiative processes associated with carrier diffusion to surface states is lower than it is for QWs [Reithmaier et al. 2002], [Naidu et al. 2010].

1.2. Thesis Structure

The thesis starts with a brief account of basic laser theory, in relation to the context of the succeeding chapters. Chapter 3 is concerned with the key process steps that constitute the fabrication of the lasers investigated in this project and it describes the experimental techniques used to obtain the results presented in the thesis. Chapter 4 focuses on the developments made in dry etching the anisotropic sub-micron features required for the devices featured in Chapter 6. Chapter 5 gives an account of the measurements made to determine the optical properties of InP/AlGaInP QD materials. Following this, Chapter 6 describes the design, fabrication and characterisation of a novel monolithic dual-wavelength laser, which is realised through developments made in the preceding chapter.

Chapter 2. Background Theory

2.1. Introduction

The purpose of this chapter is to serve as a relevant foundation for the topics covered in this thesis. It reviews some of the principles of laser diodes, including DBR lasers, and defines some general terms used throughout the proceeding chapters. Numerous textbooks provide a more detailed explanation of these topics and details of these can be found in the reference section.

2.2. The laser diode

The basic ingredients necessary to achieve laser action include a gain medium and a resonant cavity. To provide amplification of light the gain medium must be 'pumped' so that carrier *population inversion* is achieved and photon emission by de-excitation of carriers will dominate over absorption. The resonant cavity should provide optical feedback into the mode of the cavity, while also allowing a proportion of light to escape as a useful output. In addition to these basic requirements, there must be a mechanism to confine the light in both the resonant mode of the cavity and the region where carriers radiatively recombine. An example of two types of laser diodes is shown in Figure 2-1. Both of these devices are referred to as *edge-emitting* or *in-plane*, as the light is emitted from the device in the plane of the gain medium, or *active region*. In device (A) the current is only permitted to flow into the device along the central stripe where no oxide layer exists between the metal contact and the semiconductor. A device with this type of geometry is known as an *oxide-isolated stripe* laser. Device (B) is based on a *ridge-waveguide* (RWG) structure where the current path into the active region is defined by the sidewalls of the ridge. Devices with this type of geometry are know as *ridge* lasers.

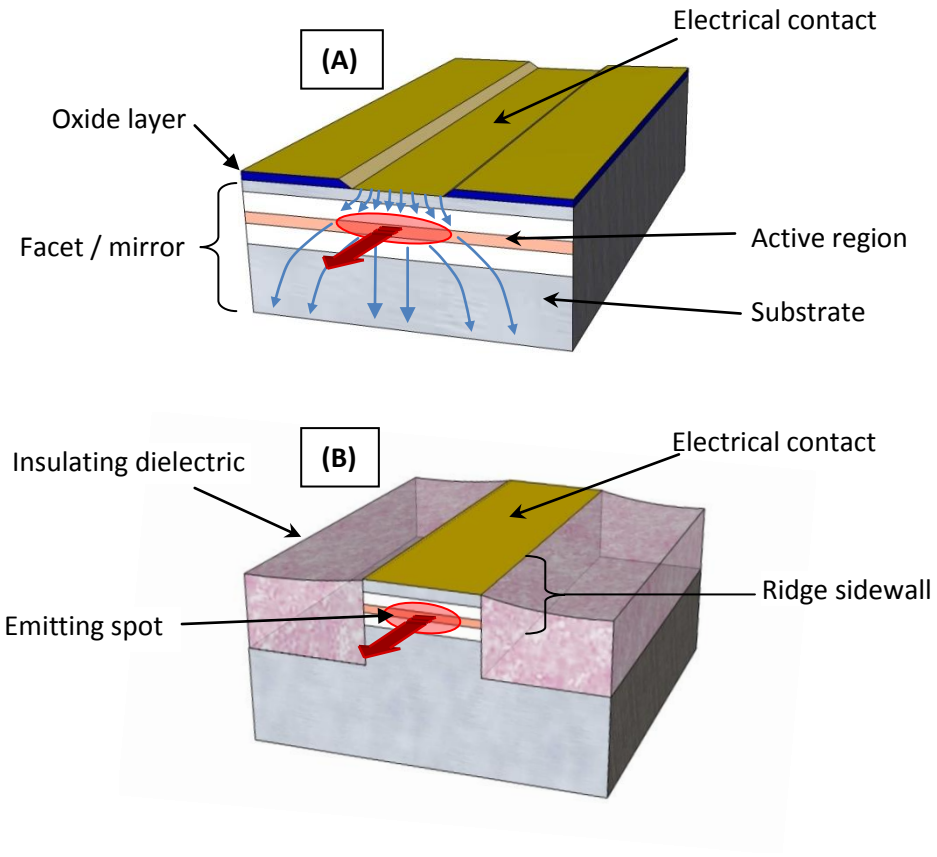

Figure 2-1: Illustration of edge emitting lasers, (A) Oxide-isolated stripe, (B) Ridge waveguide

2.3. Gain medium

2.3.1. Carrier recombination and photon emission

In a semiconductor the atomic energy levels intermix to form electronic bands. The highest occupied states of the constituent atoms combine to form the valence band and this is nearly filled with electrons when in thermal equilibrium. The next highest atomic states split to form to conduction band and this is nearly empty in the absence of excitation. If energy is given to the system, electrons can be excited into the conduction band and in doing so leave a *hole* in the valence band. The electron can return to the valence band via radiative recombination of an electron-hole pair. The photon released in this process has energy equal to the separation of states between the conduction-valence bands. Inter-band transitions are limited to certain electron-hole states which preserve the same k-vector - ensuring momentum is conserved.

There are four processes that result in electron transitions between the conduction-valence band state pairs, including: 1) spontaneous recombination (incoherent photon emission), 2) stimulated generation (absorption of a photon) 3) stimulated recombination (coherent photon emission) and 4) non-radiative recombination [Coldren, L.A. & Corzine, S.W., 1995].

2.3.2. Population inversion and Fermi-factors

In a laser diode carriers are injected into the gain medium using a current source and as such the process of generating photons is referred to as electroluminescence. If electrons are injected into the upper states of the conduction band they relax down to the bottom (lower states) via *electron-electron* interactions or *phonon-assist* processes in the timescale of a picosecond. Inter-band transitions on the other hand, occur on a slower timescale of approximately a nanosecond and this favours the ability to achieve population inversion.

In thermal equilibrium, the electrons and holes share a common Fermi energy (level), but when carriers are injected it breaks the equilibrium of the system and Fermi statistics cannot be applied. Instead quasi-Fermi levels are assigned separately to the conduction and valence band and this is considered a viable approach as the scattering process within each band ensures an 'internal' equilibrium is maintained. For amplification of light the net downward transitions must exceed the upward transitions and to sustain laser action carriers must be injected into the system to maintain *population inversion*. Under this condition the probability of an electron occupying a particular state in the conduction band, $fc_e(E_c)$, must exceed that of a corresponding state in the valence band, $fv_e(E_v)$. With the absence of an electron being represented by the presence of a hole, it follows that in the valence band:

$$fv_e(E_v) = 1 - fv_h(E_v)$$

Equation 2-1

Hence the Fermi functions are written as:

$$fc_e(E_c) = \frac{1}{1 + e^{\frac{E_c - E_{f(c)}}{k_B T}}}$$

Equation 2-2

$$fv_h(E_v) = 1 - fv_e(E_v) = 1 - \frac{1}{1 + e^{-\frac{E_v - E_{f(v)}}{k_B T}}}$$

Equation 2-3

Finally applying the condition for population inversion:

$$fc_e(E_c) > fv_e(E_v)$$

Equation 2-4

We arrive at the inequality:

$$E_{f(c)} - E_{f(v)} > E_c - E_v$$

Equation 2-5

This expression, referred to as the Bernard and Duraffourg condition, states that for population inversion the quasi-Fermi level separation must be greater than the band-gap *(E_g)* and hence the energy of the photons released. Below the band-gap the semiconductor is transparent to light, and in a small region above positive gain can exist. At higher energies the material becomes strongly absorbing, but in the transition from positive gain to absorption the semiconductor is again transparent i.e. the stimulated emission balances the absorption and $fc_e(E_c) = fv_e(E_v)$. The photon energy at which this occurs is equal to the quasi-Fermi level separation, so the region over which positive gain exists, extends from here down to the bandgap:

$$E_g < hv < E_{f(c)} - E_{f(v)}$$

Equation 2-6

Increasing the injection level will increase the quasi-Fermi level separation and therefore the gain bandwidth, but at some point the peak modal gain will match the losses and laser action will occur. Once a steady state is reached, typically after a few nanoseconds, any increase in the number of electrons being injected into the gain medium will be stimulated to recombine, raising the photon density which will further increase the stimulated emission rate. This process ensures that the gain does not exceed the losses, with the carrier density and quasi-Fermi level separations being restrained or *pinned* to their threshold values. This concept is known as *Fermi-level pinning*.

2.3.3. Threshold current

The current density *(J)* flowing through the *p-n* junction must balance with the total electron-hole recombination rate across the bandgap. At threshold the recombination rate in an ideal gain medium would be due to the spontaneous emission rate (R_{spon}) only, which can be obtained by integrating the spontaneous emission spectrum, $r_{spon}(hv)$ [Blood, 1991]. Multiplying the electronic charge *(e)* to convert to current density:

$$J_{th} = J_{spon}\left(\Delta E_{f(c,v)}\right) = eR_{spon} = e\int r_{spon}(\Delta E_{f(c,v)}, hv)dhv$$

Equation 2-7

where $\Delta E_{f(c,v)}$ is the quasi-Fermi level separation at an energy (hv).

2.3.4. Non-radiative recombination

In a real laser diode there are also 'parasitic' non-radiative recombination processes, which ultimately raise the threshold current density. The key processes are introduced below:

(i) Impurity or defect recombination

This extrinsic process relates to the successive capture of an electron and hole via a spatially located mid gap defect and is sometimes referred to as deep-state recombination, or Shockley-Reed-Hall. The energy released in the recombination event leads to a vibration of the lattice, generating heat. The process requires the presence of an electron and hole, so the capture rate is determined by the slower of these two processes. Assuming that the capture of electrons is the limiting process, the non-radiative recombination rate for *n* electrons is:

$$R_{nr} = \frac{n}{\tau_{nr}}$$

Equation 2-8

where τ_{nr} is the non-radiative lifetime which is proportional to the number of defect states.

(ii) Auger recombination

This is an intrinsic process, whereby an electron recombines indirectly with a hole in the valence band with an excess of momentum being transferred to an electron (*k*-conservation), causing an intra-band transition. The electron then loses energy via scattering processes, transferring energy to the lattice. Assuming the whole process involves two electrons and one hole, then the rate is given by:

$$R_A = C_A n^2 p$$

Equation 2-9

where C_A is the Auger coefficient and *p* is the number of holes. The process is illustrated in Figure 2-2. Similarly to the case with electrons, a hole in the heavy-hole (HH) band can transfer excess energy to another hole. This can occur in two ways; a

hole is pushed into either the light-hole (LH) band or the split-off (SO) band. Therefore, altogether three main Auger processes can occur in III-V semiconductors.

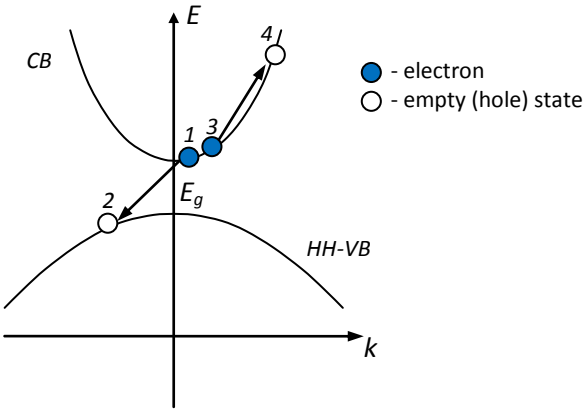

Figure 2-2: Electron energy vs. wave vector plot showing an Auger recombination process involving three electron states in the conduction band (CB) and a heavy-hole (HH) state in the valence band (VB). Arrows indicate transitions of electrons between states 1-2 and 3-4.

(iii) Surface Recombination

This is a process similar to defect recombination but is often dependent on the way a laser device is fabricated. It is most prevalent in ridge lasers where the formation of the ridge structure causes an abrupt discontinuity of the crystal lattice resulting in unmatched bonds. Unlike the localised states due to defects or impurities, the high density of surface states results in a mini-band forming at the edges of the active region. The recombination rate is characterised by a capture velocity, which is governed by the capture rate of a carrier within some capture distance of the surface.

2.3.5. Gain-Current relations

The plot in Figure 2-3 shows a typical gain-current curve of a laser diode. It can be constructed theoretically or by fitting data obtained from experimentation, for example using the peak-gain values and internal loss obtained using the segmented contact method described in Chapter 3. Using this relation the total current density for a laser fabricated from the same material can be estimated provided the internal loss, facet reflectivity and cavity length is known. The labels on the plot indicate the components which make up the total current density required to reach transparency (J_t) and overcome the loss (J_L) for a particular device.

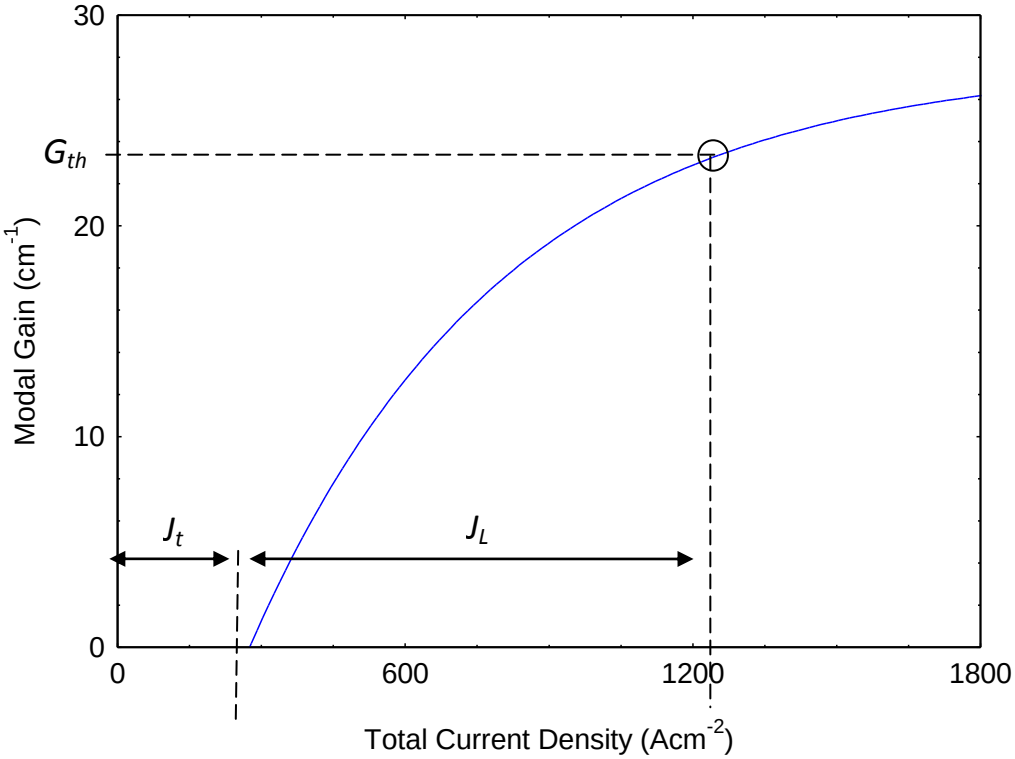

Figure 2-3: Plot of a typical gain-current relation showing the transparency *(J_t)* current and the current (J_L) required to reach threshold in a device of a specific length.

2.3.6. Quantum dots as a gain medium

Offering quantum confinement of electrons in all three dimensions, a quantum dot with its delta-like density of states theoretically possesses many of the traits associated with an ideal gain medium. Models based on arrays of identical dots predicted improvements such as reduced threshold current with lower temperature sensitivity and higher differential gain [Asada, et al. 1986]. The rationale behind these predictions is partly due to the large separation of energy states associated with the size of the dots. For instance, if the ground state of the dot is responsible for the gain and if the separation between the next energy state (1st excited state) is significantly larger than k_BT, then the carriers cannot redistribute to higher lying states and so the threshold would be temperature-insensitive [Blood, 2009]. In reality these properties have not yet been fully realised; however QDs have led to enhanced device performance in several aspects and offer superior performance over quantum well (QW) lasers. Apart from achieving low threshold current densities [Liu et al. 1999; Deppe et al. 2009], the gain-peak wavelength can be less temperature dependent [Thompson, et al. 2001; Klopf et al. 2002]. This particularly benefits devices used for frequency stabilisation,

such as DFBs VCSELs and DBR lasers [Reithmaier et al. 2002; Crawford et al. 1995], where a separation of the gain peak from the Bragg-frequency would cause an increase in threshold current. Intensity modulation can also compromise wavelength stability and this effect is characterised by the linewidth enhancement factor or *chirp.* It has been shown that chirp can be less prevalent in QD lasers and they are therefore attractive for high-speed telecoms [Saito et al. 2000].

Some of the shortcomings of QDs as an ideal gain medium are due to the nature of dot formation, which tends to give rise to statistical fluctuations in dot size and as such the energy states of the system are *inhomogeneously broadened*. Optical gain is achieved over a large energy range, producing spectra that are often broader than those observed for QW active regions. Ironically, this inability to grow dots of a uniform size does have benefits for various device applications. For example, a broad gain spectrum can be used to source multiple wavelengths using the appropriate feedback mechanism [Naderi et al. 2010] and this forms a key aspect of the work in this thesis. Under certain conditions, Fourier analysis reveals that a broad gain spectrum can be used for generating ultra-short pulses such as those produced in mode-locked lasers [Kuntz et al. 2007]. In such a device the time-average power of the laser is not changed but the peak-pulse power can be very high as all the modes of the cavity are 'locked' in phase. For a fixed gain bandwidth, the pulse duration is governed by a quantity known as the *time-bandwidth product* which is *transform-limited*. The smallest time-bandwidth product which can be achieved is therefore determined by the spectral width and such devices are said to be *bandwidth-limited*. Mode-locked lasers can be used to achieve pulse widths which are very close to this limit. Another favourable aspect of QDs in the context of devices which incorporate deep-etched grating structures, is the reduction in non-radiative processes associated with carrier diffusion to surface sates [Reithmaier et al. 2002; Naidu et al. 2010].

A growth technique known as the Stranski-Krastanov mode forms 'self assembled' dots by a *strained-layer heteroepitaxy* process. In this process a semiconductor material is deposited on another which has a slightly different lattice parameter. After the first few mono-layers have been deposited (wetting layer), the constituents of the

subsequent layers begin to nucleate into pyramidal shaped islands, relaxing the compressive strain to a more energetically favourable state [Ustinov et al. 2003].

2.3.7. Confinement of charge carriers and photons

Transverse confinement:

Inverting the carrier population of the gain medium requires an efficient way of injecting electrons and holes into the conduction and valence bands respectively. In addition, confining the optical mode to the region of the gain medium is necessary to achieve the high stimulated emission rate necessary for laser action. The advantage of diode lasers is that electroluminescence can be achieved by directly injecting carriers into the active region using a *p*-*n* junction. An effective way of confining the carriers is to sandwich the intrinsic material of the active region between two extrinsic materials of a larger bandgap, referred to as confining or cladding layers. This *p*-*i*-*n* configuration is known as the double heterostructure (DH). Unlike a conventional *p*-*n* junction, the wider bandgap of the cladding layers acts as a barrier to the electrons and holes ensuring that under forward bias, they recombine within the i-region and are not swept across the heterojunction on either side. A refinement of this design is to incorporate an additional thinner layer into the i-region which further localises the carriers in a quantum confined state. This configuration is referred to as a *separate confinement heterostructure* (SCH) and a sketch of the corresponding band structure is shown in Figure 2-4 (A).

Both the DH and the SCH design benefit from the convenient nature of semiconductors, in that a reduction in the bandgap gives rise to an increase in the refractive index. This feature of diode lasers is profoundly useful because a graded index structure which aids the capture of the carriers also guides the light to this same region. In the context of the structure discussed here, the outer cladding layers have a slightly lower refractive index than the intermediate (*barrier*) layers surrounding the active, and thus forms a *dielectric slab-waveguide*. The transverse confinement of photons created by the slab waveguide ensures that the optical mode propagates in the plane of the active, centred on the quantum confined region where radiative recombination occurs. The refractive index profile and the electric field profile for a

mode propagating in the plane of the active region are shown in Figure 2-4 (B) and (C). The dashed lines in (A) and (B) highlight the portion of the optical mode which is coupled to the region where light generation occurs.

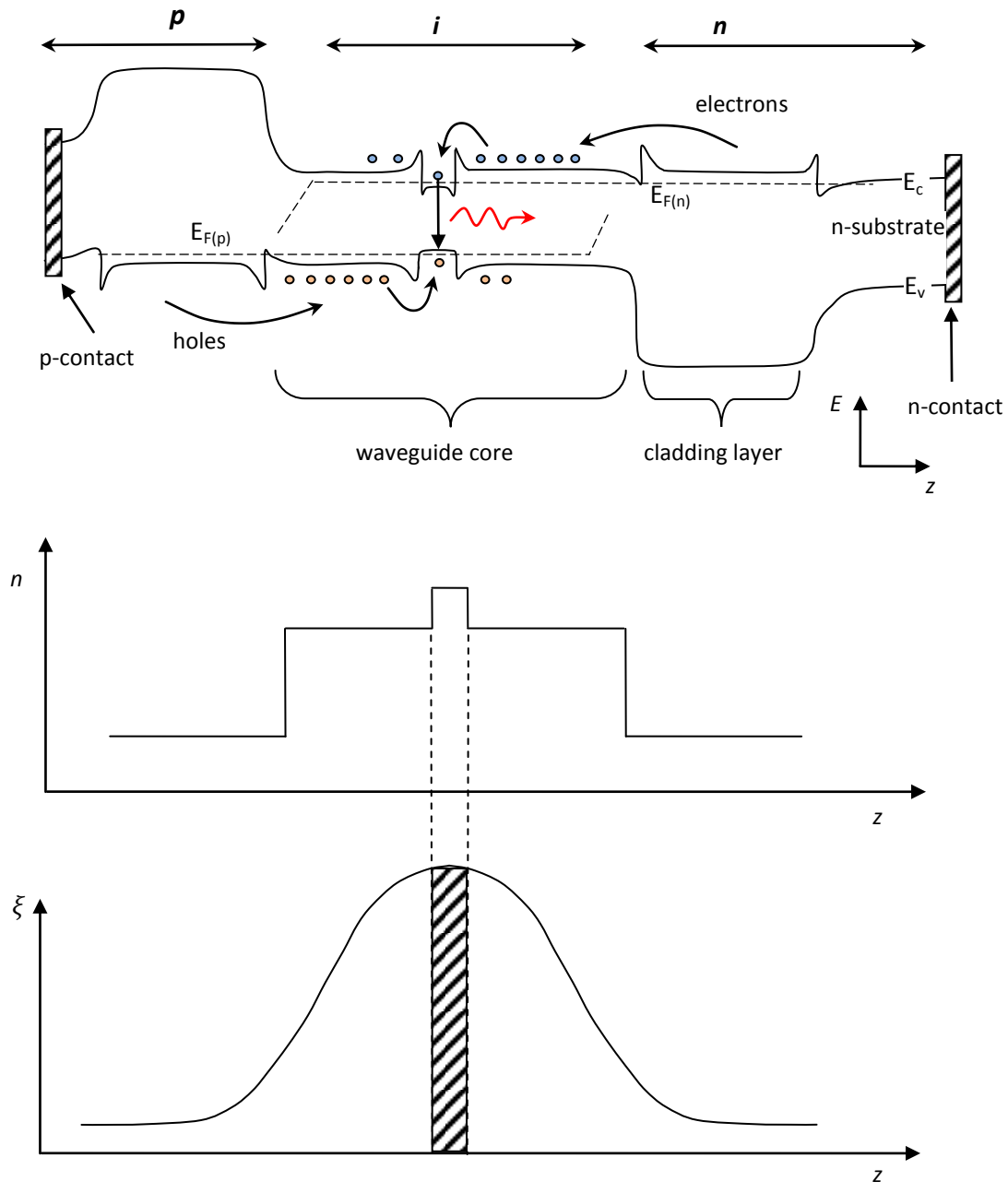

Figure 2-4: (A) Band diagram of a separate confinement heterostructure (SCH) under forward bias. Electrons and holes are injected into the active region via the *n* and *p* contacts respectively. (B) Refractive index profile (C) Electric field profile for mode travelling in the plane of the active.

The DH is pivotal to the efficient operation of the laser diode and selecting the epitaxial layers which optimise the efficiency of carrier confinement and the coupling to the optical mode is the key to their design.

An increase in the number of carriers recombining via stimulated emission will increase the intensity of the whole mode and this is characterised by the modal gain *(G)*. More specifically, *G* is the fractional increase in energy experienced by the whole mode per unit distance. The *material gain (g)* is the degree of amplification or optical gain which would incur if the entire mode was coupled to the region generating the light. It is related to the modal gain by a fractional quantity known as the *confinement-factor* (Γ):

$$G = g\Gamma$$

Equation 2-10

The value of Γ is approximately the dimension of the quantum-confined region divided by the width of the waveguide core (≈λ). More formally, Γ is the ratio of the time-averaged Poynting vector integrated over the active region, to that integrated over infinity. In the context of a laser gain medium this quantity is split into two components, the ratio of the energy velocities of the mode and the active, and the fraction of the mode coupled to the gain medium. It essentially describes the electron-photon overlap, which influences the stimulated photon generation rate and hence the modal gain. In a conventional diode laser, the energy velocities are approximately equal and so this factor is usually ignored, it only becomes significant when dealing with sub-wavelength cavities.

Lateral Confinement:

In an oxide-isolated stripe laser the light is said to be gain guided towards the region under the stripe where the carrier concentration is initially the highest. In ideal circumstances, the optical mode takes on a shape that resembles a single Gaussian, and is described as a zero order lateral mode. The high number of charge carriers in the active region reduces the refractive index via free carrier plasma interaction, but as the photon density increases the number of carriers in the centre of the active region

falls (due to stimulated recombination) and this has the effect of increasing the refractive index. This causes constriction of a filament and a stable 'self focused' profile is produced. In this situation, an effective dielectric waveguide is created where the losses are reduced, the profile becomes more defined and the laser output increases.

In ridge lasers the optical mode experiences lateral guiding due to the step in refractive index which occurs at the interface between the ridge-walls and the surrounding dielectric. This is referred to as *index guiding* and the strength of the guiding depends on the etch depth and the contrast in refractive indices. In shallow etch ridges, (etched above the active) only a fraction of the mode 'sees' the refractive index step and the gain-guiding can still play a role. In deep-etched devices more of the optical mode penetrates into the surrounding media and index-guiding is therefore enhanced. The devices fabricated in this work were based on 4 µm wide ridge waveguides which were etched down to the substrate, a depth of approximately 3 µm. Depending on the width and the etch depth, a ridge waveguide can support a number of lateral modes. Using a software package called *Fimmwave*, the modes of a ridge waveguide were solved for the appropriate epitaxial layer design and device geometry. The model illustrated the presence of five Transverse electric (TE) modes occurring within proximity of the active layer. Reducing the etch depth lowered the number of modes which the ridge supported, but for a depth of 3 µm the ridge width needed to be under 1 µm to support only the fundamental TE. The first two modes for a 4 µm wide ridge waveguide is shown in Figure 2-5(A, B) and the fundamental mode for an 0.8 µm wide ridge is shown in Figure 2-5(C).

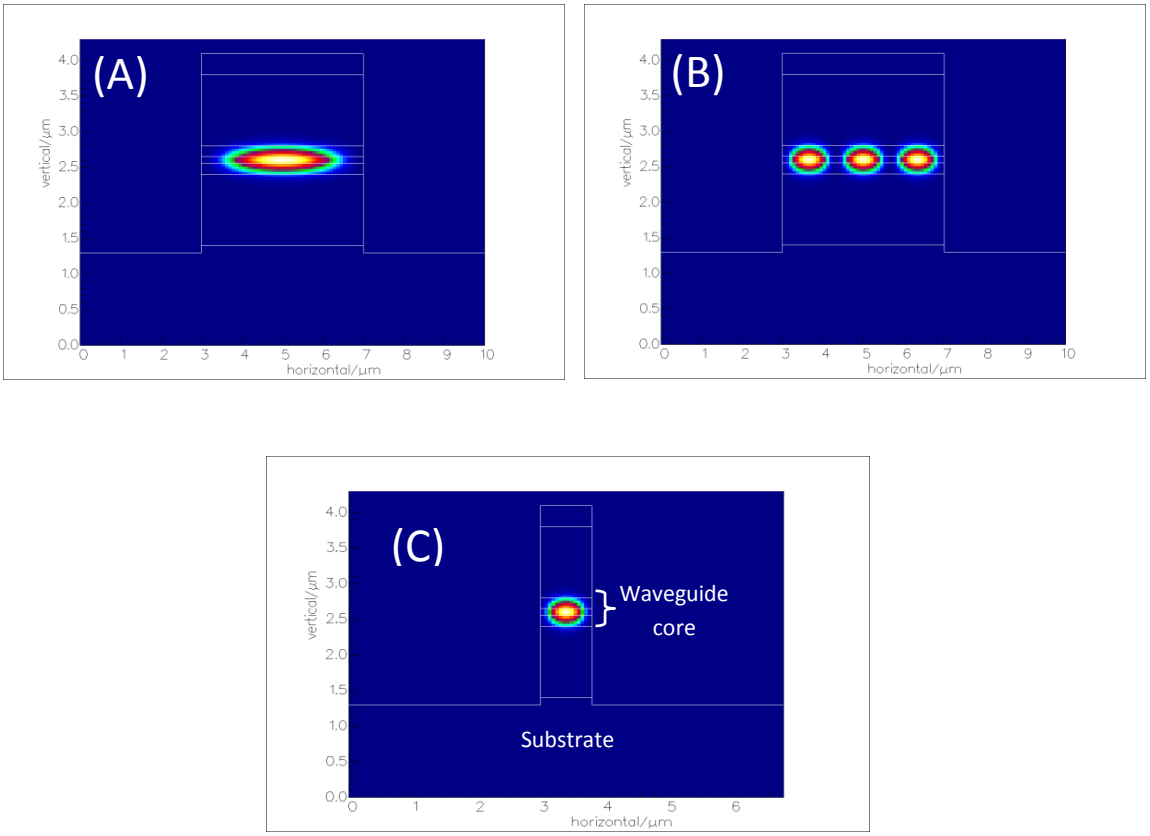

Figure 2-5: The lateral TE modes of a ridge waveguide core with intensity represented by a thermal map-scheme. (A) 4 µm -wide ridge with elliptically shaped fundamental mode, (B) higher order mode (C) 0.8 µm wide ridge supporting only the fundamental mode.

2.4. Optical resonator: The Fabry-Perot cavity

The optical feedback in a Fabry-Perot cavity is provided by the light reflected at the semiconductor-air interface defined by the cleaved facets at the two ends of the device. The contrast in refractive index between these two media gives a reflectivity of approximately 30 percent for normal incidence (assuming the *facets* preserve the planarity of the semiconductors crystal structure).

Light originating at the end of the cavity propagates though the gain medium with a time-varying amplitude and phase that can be represented by a plane wave electric field:

$$\xi(x) = \xi_0 e^{\frac{1}{2}(G-\alpha_i)x} \cdot e^{-i\beta x} e^{i\omega t}$$

Equation 2-11

ξ_0 is the magnitude of the field; *G* refers to the optical intensity gain experienced by the mode per unit length; α_i is the internal optical intensity loss of the gain medium; ω is the optical (angular) frequency and β is the propagation coefficient, related to the wavelength by $\beta = 2\pi n/\lambda$, where *n* is the refractive index for the mode. Strictly speaking *G* is wavelength dependent, but here we only need consider its fixed peak value.

The light passes along the length of the cavity (*L*) and is partially reflected off both end facets to complete one round-trip of the cavity. If the gain is sufficient to compensate for the losses imposed by the cavity, the amplitude of the electric field is unchanged. The expression derived from Equation 2-11 when applying this round-trip condition defines the threshold gain of a laser:

$$G_{th} = \alpha_i + \frac{1}{2L} ln\left(\frac{1}{R_1 R_2}\right)$$

Equation 2-12

where R_1 *and* R_2 are the intensity reflectivity's of the end facets. The last term on the right hand side of the equation is referred to as the mirror loss (α_m). The phase condition is satisfied when the exponential term containing the propagation coefficient equals unity. This requires that $\beta L = m\pi$, where *m* is the longitudinal mode number. A given length cavity will support resonant modes at integer values of half wavelengths. Since the gain spectrum has a finite width several optical modes will be expressed. The wavelength separation between modes can be found by differentiating λ with respect to *m,* which gives:

$$\Delta\lambda = \frac{\lambda^2}{2\tilde{n}_g L}$$

where $\tilde{n}_g$ is the group effective index.

Equation 2-13

2.5. Photonic structures in semiconductor lasers

The periodic structure of a crystalline lattice is the property which allows electrons to freely propagate through a conducting material, provided they have the appropriate energy. The energy criterion for allowable propagation is defined by the energy band structure of the material and is dependent on the constituent atoms and their spatial arrangement. A gap in the energy band structure prevents the propagation of carriers with certain energies and is termed the energy band-gap. In analogy to this, photonic crystals possess a photonic bandgap, where the nature of the light being prohibited from propagating may depend on several factors such as frequency, direction and polarisation. In this work, the propagation of light is only controlled in one dimension by the fabrication of grating structures which are used to influence the reflectivity of the laser mirrors.

2.5.1. One-Dimensional photonic crystal

A photonic band-gap is achieved by creating a medium which has a periodically varying dielectric constant. This medium or grating can be designed to control the reflectivity and transmissivity of the light. Bragg's law is obeyed when the reflection from each of the interfaces of the grating are in phase, constructively adding up to a large net reflection. To qualify for this condition the following expression must be satisfied:

$$2dsin\theta = mn\lambda$$

Equation 2-14

where *d* is the spacing, θ is the angle of incidence from the normal and *m* is the order and *n* is the refractive index.

A *quarter-wave stack* is a relatively simple way of satisfying this condition with maximum reflectance being achieved. The stack consists of alternating layers of material with high and low refractive indices. Light with a particular wavelength incident on the medium is partially reflected at each interface and for *N* pairs of layers a maximum in reflection occurs when:

$$n_1 d_1 = n_2 d_2 = \frac{\lambda}{4}$$

Equation 2-15

where n_1, *and* n_2 are the refractive indices of layers with thickness d_1, *and* d_2 respectively. This arrangement of alternating layers produces a reflectivity spectrum which peaks at the wavelength around which the layers were designed. The characteristic width of the spectrum is referred to as the stop-band. The index ratio n_2/n_1 is responsible for the width of the stop-band and *N* determines the peak magnitude. In general, the stop-band can be made broader by increasing the index ratio and the reflectivity improved by increasing *N.*

2.5.2. Lasers with Bragg gratings.

Incorporating a photonic crystal of this nature into the ends of a laser cavity can increase the mirror (facet) reflectivity, which is ordinarily around 30 percent for a cleaved facet. A laser device which makes use of this structure is called a Distributed Bragg Reflector (DBR) laser [Avary et al. 2001; Raffaele et al. 2001; Yuan et al. 1997]. The highly reflective mirrors, or Bragg reflectors placed at the ends of a laser cavity can provide numerous advantages. Due to the increased optical feedback, it allows smaller devices to be fabricated without increasing the threshold gain requirement. They can also be used to enhance single longitudinal mode emission; for example, in vertical cavity surface emitting lasers (VCSELs) the length of the cavity can be made small enough that only a single cavity mode falls within the reflectivity stopband.

It should be noted that improvements in feedback may come at the expense of introducing scattering or diffraction losses. In addition, if a portion of the gain medium is replaced by the Bragg reflector there is less amplification of light within this section

of the device. A modified version of the Fabry-Perot relation for threshold gain given in Equation 2-12 takes into account for the loss induced by the grating:

$$G_{th} = \alpha_i + \frac{1}{2L_{DBR}}\left\{ln\left[\frac{1}{\left|R_{g1}(\lambda)R_{g2}(\lambda)\right|}\right] + 2ANd\right\}$$

Equation 2-16

where L_{DBR} includes the active length of the cavity, any passive sections and the effective length of the grating as seen by the optical field. The absorption loss induced by the grating is given by the last term in the equation, where *A* is the loss occurring at each layer pair, *N* is the number of periods and d is the thickness. Here $R_{g1,2}(\lambda)$ are the wavelength dependent reflectivity's of each Bragg mirror. Using an appropriate model, the scattering and diffraction loss could be taken into account when calculating the reflectivity. Figure 2-6 is a schematic of a typical grating profile used in a DBR laser, which is created by etching into the device's structure. If the etched slot does not completely penetrate the active region, then the optical mode is only partially affected by its presence. In this situation, the field reflectivity of light at the interface between segments 1 and 2 can be approximated by inserting the effective indices of the segments into Fresnel's equation:

$$\tilde{r} = \frac{\tilde{n}_2 - \tilde{n}_1}{\tilde{n}_2 + \tilde{n}_1} = \sqrt{R}$$

Equation 2-17

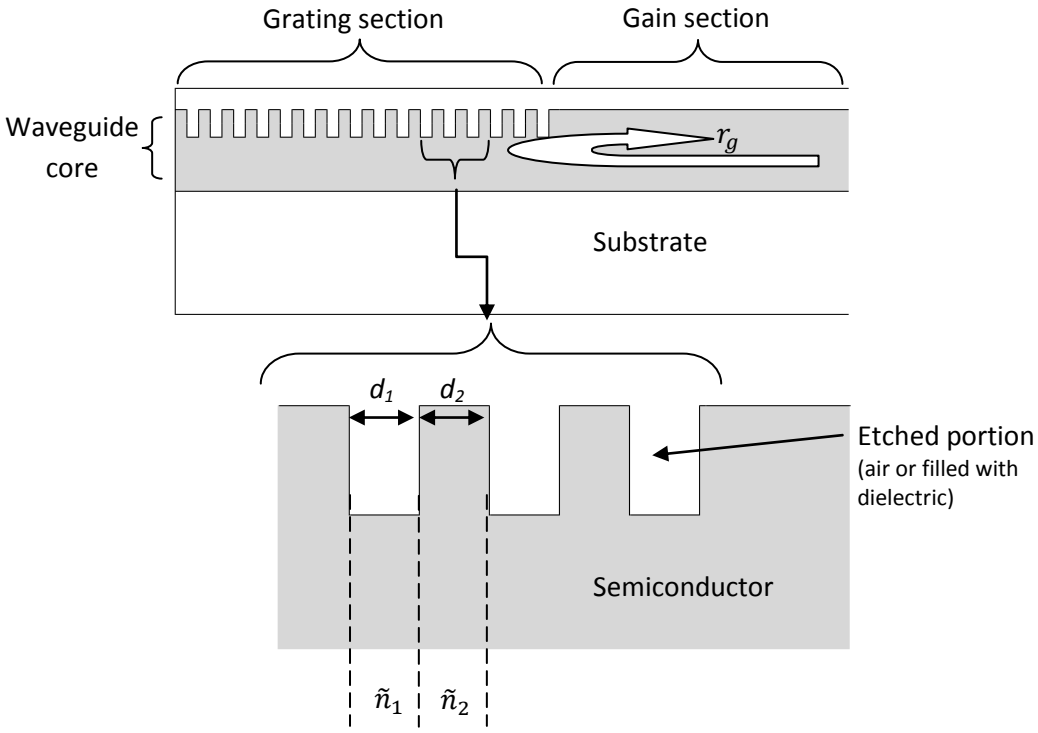

Figure 2-6: Side-profile schematic of a grating structure used for an in plane DBR laser. The remainder of the waveguide (not shown) extends to the right. The curved arrow in the waveguide core illustrates light being coupled back along the cavity due to the net reflection of the grating section.

At the Bragg frequency, the field reflectivity of the whole grating can be approximated by $r_g \sim 2N\tilde{r}$ provided that the reflections at each interface are relatively weak [Coldren, L.A. & Corzine, S.W., 1995]. For the grating structures fabricated in this project the reflectivity at each interface causes the field intensity to fall off rapidly and so a more sophisticated calculation is required, as described in section 2.5.3.

Although shallow etched gratings can be more selective in terms of feedback to a particular mode, they require many repeats to achieve a high reflectivity. In addition, due to the vertically varying refractive index they can have the effect of pushing the mode down towards the substrate. Deep-etched gratings on the other hand, extend down through the active region of the device and can offer the same reflectivity for fewer repeats, without influencing the transverse location of the mode. These types of grating structure have been employed in the devices fabricated in this thesis and their resulting reflectivity stop band was modelled using a *transfer matrix model* (TMM),

which is a standard method of solving problems of light propagation through multilayer films [Hecht, E., 1998]. When incorporating deep-etched structures the length of the grating section can be made much less than the length of the cavity and therefore the second loss term in Equation 2-16 can be negligible.

2.5.3. Reflectivity calculation of DBR gratings

The design of the DBR gratings was based on one-dimensional quarter-wave stacks with the TMM being used as a tool to estimate the form of the reflectivity stop-band. The model does not take into account losses due to diffraction and assumes that each grating portion is homogeneous and isotropic. Taking the optical mode to have a Gaussian form, the diffraction loss across each grating portion is expected to be low because the dimension of the grating portions are within the near-field regime or the so-called Rayleigh range, with the beam waist across the grating not increasing by more than a few percent. The model only considers light propagation normal to the grating interfaces and with the dimensions in the plane of the layers taken to be semi-infinite. The assumption, in the context of DBR lasers, is that the grating portions are etched vertically down to the substrate so that the entire optical mode is coupled to the grating. Based on a TMM, an expression for the field reflectivity coefficient for a multilayer Bragg stack, with refractive indices, n_s and n_0 for the semiconductor and etched gap respectively, is given by:

$$r = \frac{m_{11}\Upsilon_s + m_{12}\Upsilon_s\Upsilon_0 - m_{21} - m_{22}\Upsilon_0}{m_{11}\Upsilon_s + m_{12}\Upsilon_s\Upsilon_0 + m_{21} + m_{22}\Upsilon_0}$$

Equation 2-18

where

$$\Upsilon_{s,0} = \sqrt{\frac{\varepsilon_0}{\mu_0}} n_{s,0}$$

Equation 2-19

And m_{ij} (i, j = 1,2...) are the elements of a matrix which are obtained by multiplying the individual characteristic 2×2 matrices which relate the tangential components of the

fields across two adjacent boundaries. In matrix notation, the linear relations between the magnetic and electric fields across a two-layer boundary are given by:

$$\begin{bmatrix} E_0 \\ H_0 \end{bmatrix} = \begin{bmatrix} \cos k_0 d & \dfrac{i \sin k_0 d}{\Upsilon_s} \\ \Upsilon_s & \cos k_0 d \end{bmatrix} \begin{bmatrix} E_s \\ H_s \end{bmatrix}$$

Equation 2-20

where k_0 is the propagation vector ($= 2\pi/\lambda$) and *d* is the layer thickness. The product of these two parameters describes the phase shift that occurs when the wave undergoes one traverse of a layer.

Despite being a simplistic model, it does provide useful information on how the form of the reflectivity stopband is influenced by changes in the grating's structure. The reflectivity spectra computed for a uniform semiconductor/dielectric multi-period DBR grating is shown in Figure 2-7. It illustrates the effect of varying the order of reflection (A) and the refractive index of the gap media (B). The plot in (C) demonstrates how the number of periods (or max reflectivity) varies the threshold gain requirement for cavities of various lengths. Increasing the order of the grating reduces the width of the stop-band but also reduces the maximum reflectivity, and similarly for increasing the refractive index of the gap material. For any permutation of order or refractive index, increasing the number of periods enhances the maximum reflectivity. However, the incremental increase in reflectivity with adding subsequent layers begins to saturate after approximately four repeats and this is reflected in the threshold gain requirement (Figure 2-7 C). It is therefore unnecessary to include anymore than four or five repeats when fabricating deep-etched DRBs.

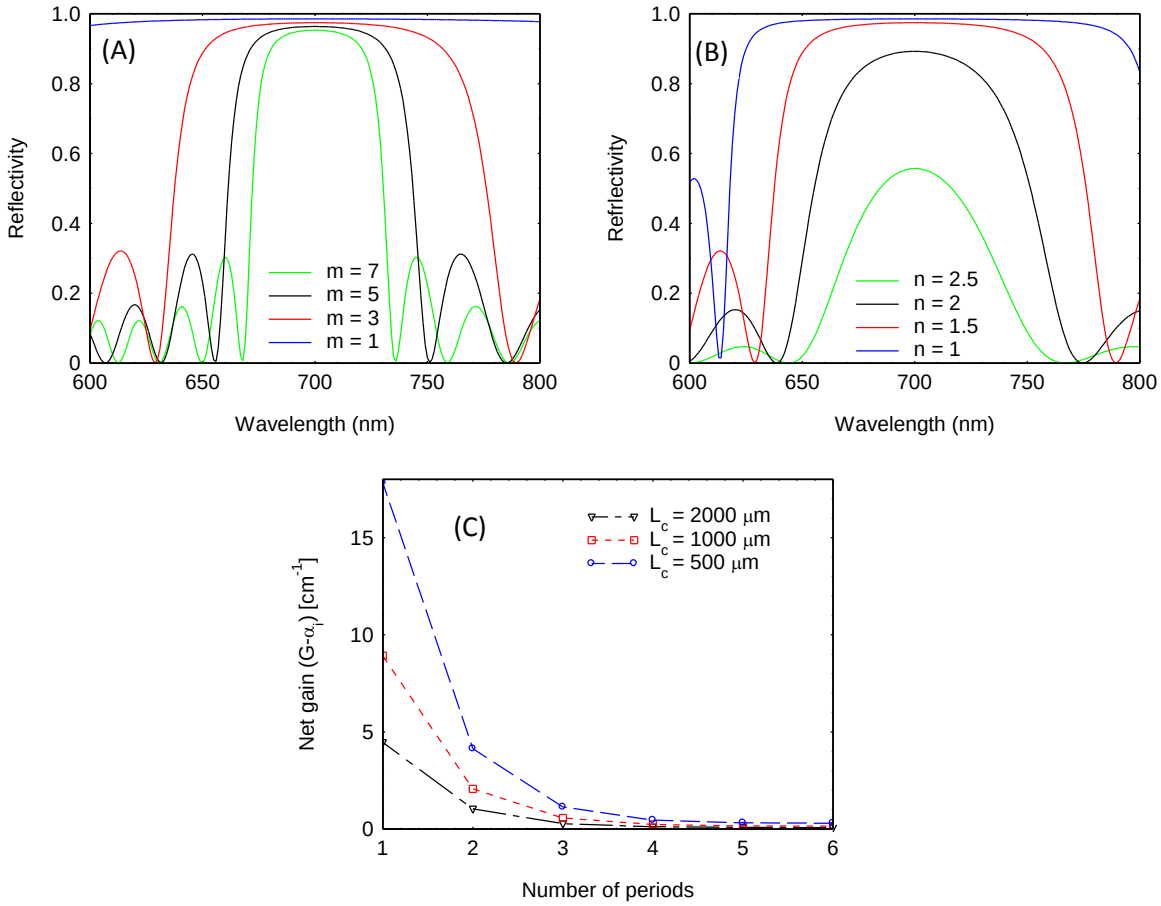

Figure 2-7: Computed reflectivity spectra using TMM showing: (A) effect of varying the order, m (m/4λ), (B) varying refractive index of the gap material, *n* and (C) effect the number of periods (max reflectivity) has on the threshold gain.

In practical terms, it is important to use grating dimensions which are within the limitations of the fabrication processes. The formation of deep-etched structures becomes particularly difficult as the dimensions of the gratings are reduced and this will become apparent in Chapter 4. The size of the grating portions in the direction of periodicity depends on the order (*m)*, the refractive indices, and wavelength of light. For an m_{th} quarter-wave DBR design the thickness of the layers can be calculated using:

$$d = \frac{m\lambda}{4n}$$

Equation 2-21

2.6. Summary

This chapter dealt with the necessary background to support the work described in this thesis. The two essential ingredients for laser action where identified as the gain medium and a resonant cavity. Two main types of waveguide geometries were introduced, which make use of gain-guiding and index-guiding to confine the optical mode in the transverse direction. The amplification of light by stimulated emission within the gain medium is achieved by electrical injection, which acts as a pump source maintaining population inversion. The concept of using quantum dots as a gain medium can offer several advantages for devices conceived in this project. For example the inhomogeneous size distribution of dots gives rise to a broad gain spectrum which can be used to source multiple wavelengths from one active material. In addition, the low surface recombination (lower than that found in QWs) becomes important when forming deep-etched structures on which the devices in this work are based on. The need for the gain to overcome the loss induced by the cavity was discussed, and finally the use of gratings to increase the feedback of the optical mode was explained, where a transfer matrix model was used to estimate the form of the reflectivity stop-band for deep-etched gratings. It was found that the width of the stop-band was influenced by the contrast in refractive indices of each portion of the grating and the order of periodicity. The number of repeats determines the maximum reflectively, and for deep-etched gratings it was found to saturate after four repeats. The information obtained from the model was used in designing the devices fabricated in this work and was useful in interpreting measurements.

Chapter 3. Device Fabrication and Experimental Techniques.

3.1. Introduction.

Several types of laser and non-lasing (multi-section) devices have been explored during this study, which have been based on either an oxide-isolated stripe or ridge-waveguide (RWG) geometry. This chapter provides details on the process steps and developments used to fabricate devices based on RWGs only, since the former type were fabricated using standardised processes. The chapter begins with an overview of these processes where details of each step are given sequentially, in the order they occur in the process flow. Although dry etching is introduced here, the development of an optimised etch recipe used for InP/AlGaInP is explained later in Chapter 4. Following this, the experimental setups and methods used to characterise each device are described, with comments on essential criteria which need be met in order to achieve accurate results. Finally, the post fabrication device tests are explained, with reference to their importance in a particular measurement and the process steps responsible for the outcome of each test.

3.2. An overview of fabrication processes

All post-growth fabrication processes were carried out by the author in a class 1000 cleanroom with a class 100 enclosure used for optical lithography. There are numerous steps which constitute an entire laser process, but these can be generalised into eight main categories, beginning with sample preparation and ending with the final chip mounting and wire bonding required for electrical injection. An example process flow is given in Appendix A.

3.2.1. Sample Preparation

A sample of sufficient size (typically 10×10 mm) is cleaved from the wafer, with reference to the major flats, along the crystallographic plane. Since the substrate (001) in these samples is orientated 10° towards [111] it is essential that alignment of the RWGs is such that they run parallel to this, ensuring that the cleaved facets of the laser

are perpendicular to the RWG. After cleaving the sample, it is cleaned using multiple solvents to remove contaminants such as grease and cleaving debris. The four solvents used (trichloroethylene, acetone, methanol and isopropanol) are dispensed into separate glass beakers and placed on a hotplate set at 80 °C. The sample is placed in each solvent for 5 minutes.

3.2.2. Lithographical Patterning

Exposure of resist patterns, used to define etch-masks for RWGs and any incorporated photonic structures, was carried out using Electron Beam Lithography (EBL). Two types of EBL system were used: a Raith50 comprising of a Phillips XL SEM with a Lanthanum Hexaboride (LaB_6) emission tip and a Raith150 e-Line with a Tungsten field emission tip. Both of these systems also provided high resolution imaging capability and were useful for verifying feature dimensions and assessing the quality at certain stages of the process. Samples were spin-coated with Microchem 950K Polymethyl-methacrylate (PMMA) at 6 krpm for 45 s and then placed on a hotplate at 180 °C for 3 minutes. Preparation of the PMMA results in a film thickness of ≈ 200 nm.

Many of the devices fabricated in this work involved creating submicron features inside or at the end of a RWG. The size of the patterned features was well within the capabilities of the equipment available; however the particular design of the pattern brought about complexities with regard to achieving the correct exposure. Firstly, write times were often several hours, so if the beam current drifted over time then there was a variation in dose (relative exposure of resist to electrons) received by different areas of the pattern. This will of course vary the size of the photonic features and if it were, for example, a Bragg grating this would affect the associated reflectivity stop-band. This drift can partly be accounted for by patterning all the critical portions of the pattern first. The only issue with this approach is that the stage may not return back to the original location after traversing across the whole sample due to hysteresis effects. A LaB_6 tip is typically more emissive than one made from tungsten, so the Raith50 has the advantage of a shorter write time; however the e-Line system proved to be far superior in terms of current stability and was therefore essential for generating patterns which contained large areas of submicron features.

During exposure the electrons are subject to forward scattering as they propagate through the resist, and back scattering from the underlying semiconductor. As a consequence the exposed patterns are not the same as the design drawing used to define the pattern. This is known as the proximity effect, which leads to pattern dependent line-width variations and becomes particularly important for dense features [Rai-Choudhury, P., 1997]. When patterning a grating within a RWG the proximity effect can result in a significant variation in the line-width of the grating portions and it is therefore essential to correct for it. The SEM image in Figure 3-1 illustrates how the line-widths of a grating are affected when a ridge is exposed in close proximity. Here the grating portion closest to the ridge is 62 nm wider than the end portion and the extent of the variability depends on many factors such as resist thickness, energy of the electrons, size of the features and their relative spacing. The shape of the ridge itself is also affected by the proximity effect, in that the edges appear curved. The simplest way to correct for the proximity effect is to modulate the dose received by different areas of the pattern. Proximity correction tools built into proprietary software of the Raith system do this by dividing the pattern into a number of polygons and assigning a dose to each one. However, the exposed pattern resulting from these corrections seldom achieves the desired line-widths. Instead it's more appropriate, although somewhat tedious, to use the software to divide the pattern into a number of polygons and then manually assign the doses. This often entails constructing a dose matrix pattern, whereby a number of doses are applied until the correct line-widths are achieved.

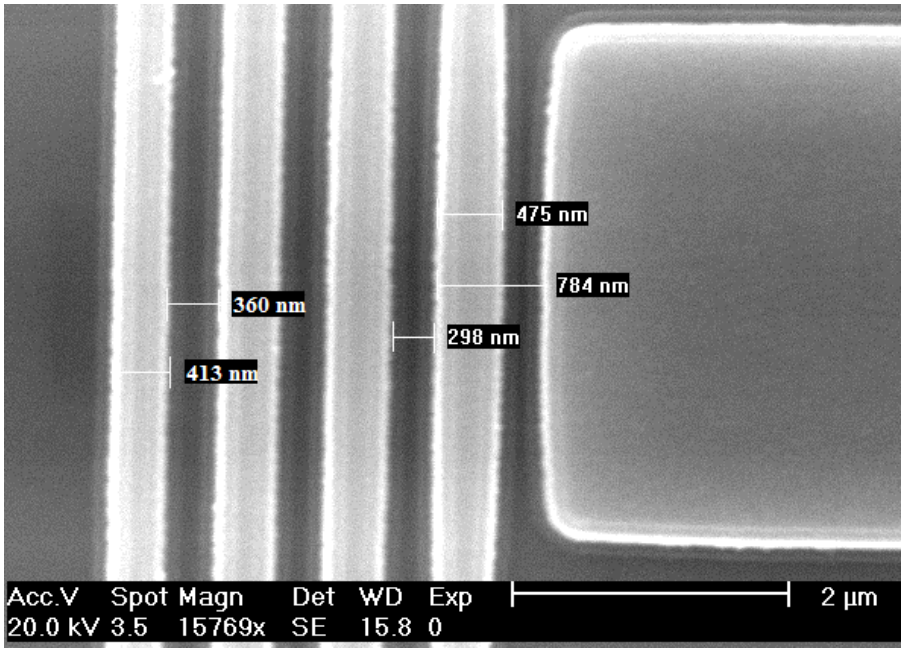

Figure 3-1: SEM image of grating showing proximity effect caused by the presence of a ridge exposure.

3.2.3. Etch Mask Definition

The semiconductor etch mask can be defined by two methods: (1) Deposition of mask material prior to lithography, followed by etching of the exposed regions, or (2) Post exposure deposition followed by a *lift-off process* (a solvent dissolves unexposed resist and the mask material is 'lifted off' in these regions). As discussed above, the patterning of sub-micron features requires the use of EBL and due to ease of alignment it is desirable to also expose larger features using this technique provided the write time is acceptable. An added advantage of using EBL over photo-lithography is that patterns are free of mask defects and designs can easily be changed in the Raith software.

Since PMMA is a positive tone resist (exposed regions dissolve away after development) and the patterned features cover a small area of the sample, it is preferable to use method (2) for mask definition as it minimises write time.

The resist profile at the exposed edges and the thickness of the deposited mask material are two important factors to consider when performing a lift-off process. An under-cutting resist profile is preferable, but a vertical one will also give good results. The second factor critical to a successful lift-off is the thickness of the mask material

relative to the resist. Ideally, the resist's thickness should be 50 % more than the mask. To be an effective etch mask, the outer edges need to well defined and sharp, as any imperfections or roughness will transfer into the semiconductor during an etch process. This will lead to scattering of the optical mode and in addition, it is likely to increase the overall surface recombination rate since the total surface area would be greater [Coldren, L.A. & Corzine, S.W., 1995; Naidu et al. 2010]. To improve the edge profile of the mask it was necessary to expose the outer edges of the patterned features with a higher dose. For example, when patterning a 5 µm RWG it was sufficient to expose the outer 500 nm with a dose 1.5 times higher than the inner regions of the ridge. The effect of this, together with the appropriate proximity correction can be seen in the resulting *lift-off* shown in Figure 3-2. Image *A* and *B* illustrate examples with and without the dose correction applied, respectively.

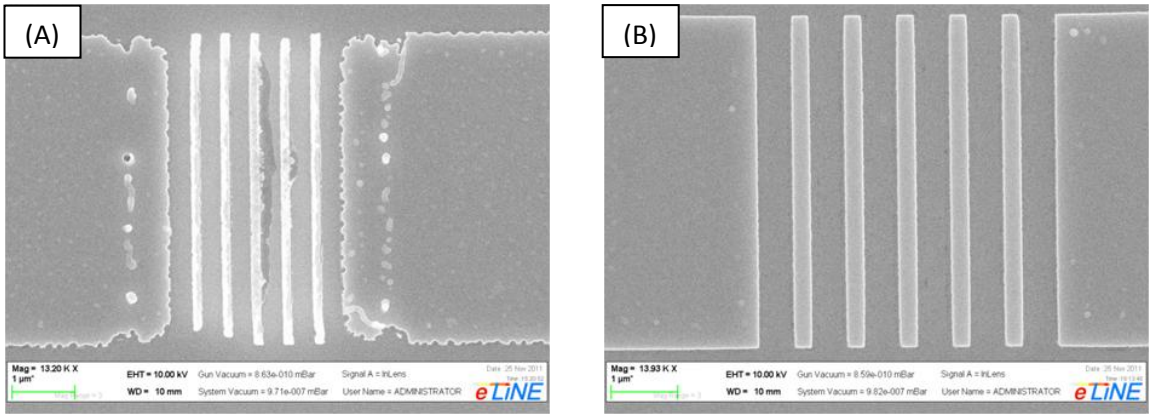

Figure 3-2: SEM images of nickel mask lift-off used to define RWG and DBR grating. Image (A) shows rough outer edge of the mask as a result of insufficient exposure, which is avoided by increasing the dose to the outer regions of the pattern, as shown in image (B).

3.2.4. Etching

As explained in Chapter 2, gratings are used to form the reflecting mirrors of the laser cavities featured in this work. To be effective (maximum reflectivity for fewest repeating units) the gratings need to be deep-etched and have vertical sidewalls so the reflection is normal to the plane of the laser cavity. To produce these high-aspect ratio (typically 20:1) features it is necessary to use a dry-etch method. This type of etching uses a plasma-assisted process which is both chemical and physical in nature. A reactive species, composed of the gases introduced to the chamber, chemically etch

the surface of the semiconductor, while the energetic ions present in the plasma cause a physical sputtering, enhancing the chemical etch rate (ion-assited chemical etching) and to some extent, facilitate the removal of the etch product. This results in highly directional etching, producing an anisotropy that is not achievable with wet-etch techniques.

RWGs and incorporated photonic structures were dry etched, typically to a depth of 2.5 microns, using an Inductively Coupled Plasma (ICP) process in an Oxford Instruments Plasmalab 100 system with an ICP380 chamber design. Details of the etch recipe specifically for InP/AlGaInP are given in Chapter 4.

3.2.5. Planarisation

Planarization of a semiconductor wafer usually involves spin-coating the surface with a dielectric polymer. A “back-etch” procedure is then performed to reveal the tops of raised mesa structures, allowing metal contacts to be made. Planarization is done for two reasons: firstly it acts as an insulator to prevent shorting of the metallurgical junction during metallisation of the top-contact and secondly it removes the topography of the surface, simplifying subsequent lithography steps. In addition it also protects the surface, and the value of the dielectric constant can prove useful for its function as a grating portion in a Bragg stack.

Two different types of spin-on dielectric polymers were used for planarity of the etched samples, including Cyclotene 3022-46, derived from benzocyclobutene (BCB) monomers, and hydrogen silsesquioxane (HSQ), under the trade name *FOx* (Flowable Oxide).

Both of these spin-on polymers proved to have excellent gap filling properties, but HSQ was observed to have a maximum crack-free thickness of one micron when using the recommended curing procedure. For this reason BCB was preferable for deep etched features and became the standardised method. Uniformity of planarization is essential for high device yield and to achieve this it is important that the sample is free of contaminates and moisture. An oxygen plasma is used to *de-scum* the surface and a two minute bake on a hotplate at 100 °C is used to dehydrate the sample prior to

planarization. The quality of the BCB film, the planarity and profile surrounding topographical features, is also sensitive to the way in which it's applied, in terms of the spin speeds and the curing procedure. Application of BCB first requires an adhesion promoter (AP3000), which is spun in two stages: 200 rpm for 5 seconds (allowing it to spread out evenly), then spun dry at 2500 rpm for 20 seconds. Similarly, the BCB is first spun on at 600 rpm and then ramped to 4000 rpm for 30 seconds to fully spin-coat the sample to a thickness of approximately 2.6 microns. The sample is then placed on a hotplate at 100°C for 2 minutes to drive off solvents and add stability to the film. A soft cure is then carried out in a nitrogen atmosphere at a temperature of 210°C, which achieves 75 – 80 % polymerisation. It is important to raise the temperature slowly (5 $°Cmin^{-1}$) between temperatures 100 to 210°C to retain good morphology. After back etching the BCB and deposition of metal contacts the BCB can be fully cured at 300°C for 60 minutes.

3.2.6. Metallisation and Contact Isolation

When forming metal-semiconductor contacts, for the purpose of delivering carriers for electroluminescence, there are two important criteria which must be met. The contact must be made ohmic (inherently rectifying if not alloyed), producing *I-V* characteristics which are stable with time and temperature, and secondly it must adequately adhere to the semiconductor surface. The way in which this is achieved depends on the extrinsic properties of the semiconductor. In p-type materials the barrier height at the interface (ϕ_b) is determined mainly by the group-V element and for n-type by the group-III. The barrier height, and hence the resistance between the interface, decreases with increasing atomic weight and for this reason the alloying process is more critical for n-type GaAs.

Figure 3-3 illustrates the band structure of a metallurgical junction which is formed by the contact of a metal to an n-type semiconductor. Upon contact, charge flows between the metal and semiconductor creating a *depletion region* and the energy bands of the semiconductor are 'bent' to insure that in equilibrium the Fermi-level is continuous across the junction (see Figure 3-3-B). The potential barrier inhibiting the flow of charge across the interface is dependent on the work function of the metal (ϕ_m) and the electron affinity of the semiconductor (χ_s), such that, $\phi_b = \phi_m - \chi_s$. In most cases $\phi_m > \chi_s$, therefore to from an ohmic contact the semiconductor must be alloyed by annealing the metal contact, this increases χ_s relavtive to ϕ_m and removes the potential barrier, as illustrated in Figure 3-3-C. The extent of the band-bending in either case is given by the *contact potential (eV_0)* and is equal to $|\phi_m - \phi_s|$.

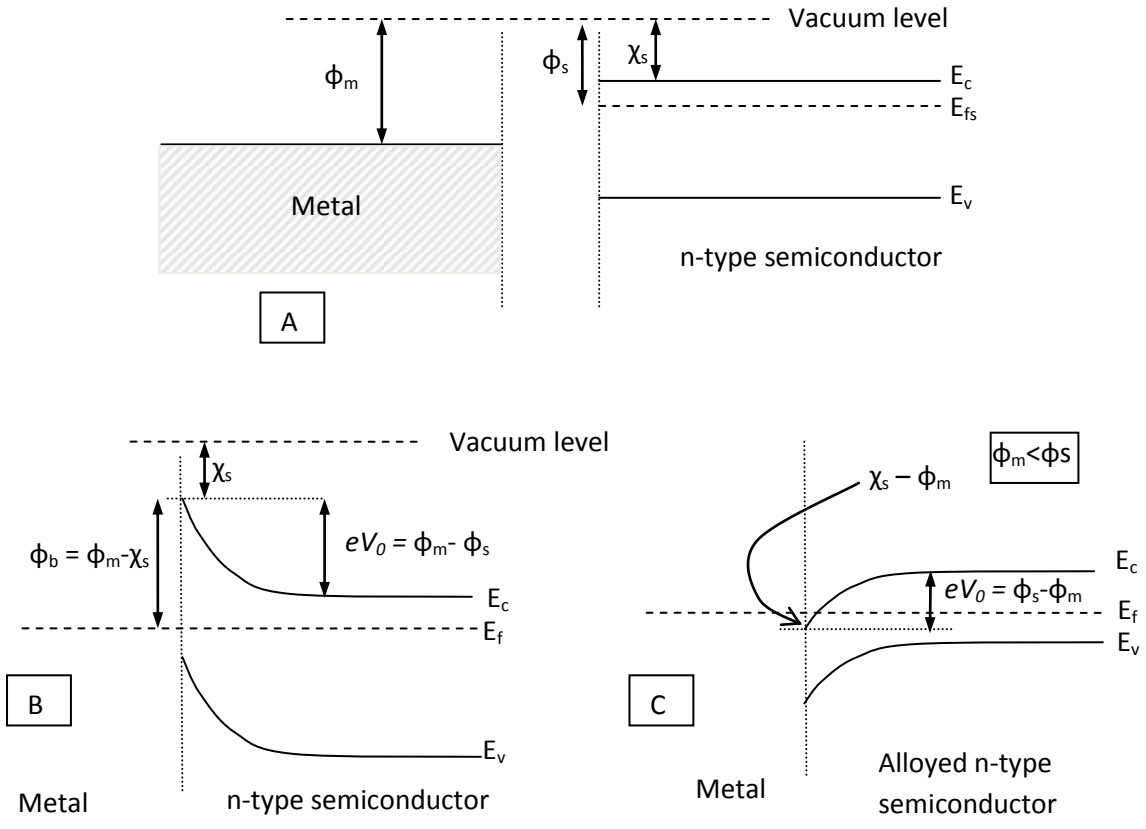

Figure 3-3: Band diagrams describing the formation of a metal-semiconductor interface. A) Band structure of n-type semiconductor and metal before contact is made, B) Formation of a metallurgical junction (Shockley barrier) and C) Alloyed semiconductor; formation of ohmic contact by removing potential barrier (ϕ_b).

n-type GaAs: AuGe/Ni/Au was used with thicknesses of 100 nm/28 nm/ 300 nm. Under the alloying process (occurring between 355 - 385°C) the germanium inter-diffuses with the GaAs and replaces some of the gallium which itself diffuses into the gold. Nickel is thought to act as an anti-balling agent improving the morphology of the surface and may also aid inter-diffusion of germanium into GaAs [Williams, R.E., 1984]. The overlaying gold is applied to improve the sheet resistance and provide a suitable surface for wire bonding.

p-type GaAs: For p-type metallisation there is a greater selection of metals which can be used to form ohmic contacts. However, since RWGs fabricated here offer only a small area of contact (typically 5 microns in width) it is important that the metals have good adhesion. Zn/Au, the standard contact applied on 50 micron oxide-isolated stripe lasers, was initially used but the adhesion was poor and in some cases lifted away from the ridge tops. Instead Cr/Au and Ti/Au contacts were investigated, both of which are known to have very good adhesion to GaAs. In order to ascertain the suitability of these two contacts and decide on the most appropriate to use, it was necessary to perform Transmission Line Model (TLM) measurements [Williams, R.E., 1984] and adhesion tests.

An important parameter when deciding which contact would be most suitable (electrically) is the anneal temperature at which an ohmic behaviour can be achieved. Dow Chemicals, the manufactures of BCB, specify that the curing temperature should not exceed 350°C. In view of this the anneal temperature of the p-contacts did not exceed 350°C when preparing TLM test structures. A TLM pattern consists of 100 × 100 µm contact pads arranged in a grid on a sample of semiconductor wafer. The pads are formed by evaporating the desired metals onto a patterned resist followed by a *lift-off* process. The separation between pads *(L)* is varied from 5 to 35 µm and the resistance between pads is measured using a four-probe method. This entails passing a constant current between adjacent pads and measuring the voltage dropped between them. This is performed for each pad separation over a range of currents to generate I-V curves. Figure 3-4 shows I-V curves for a Ti/Au contact on p-GaAs which had not been annealed, together with a Ti/Au and Cr/Au contacts annealed at 350°C. It is evident from the plot that the as-deposited Ti/Au contact is rectifying. Annealing at 350°C

shows significant improvement but the Cr/Au contact proved to form the best ohmic contact. In addition the deposition and annealing process of Cr/Au resulted in a better surface morphology, with a superior adhesion to GaAs. Therefore Cr/Au became the metallisation of choice for p-contacts. By obtaining the resistance for each I-V curve and plotting against *L* (separation between pads), the contact resistance between the metal and the underlying semiconductor can be found, and since the area of the pads is known, the specific contact resistance *(r_s)* can also be obtained (typically $r_s \approx 7\times10^{-5}$ Ωcm^{-2}).

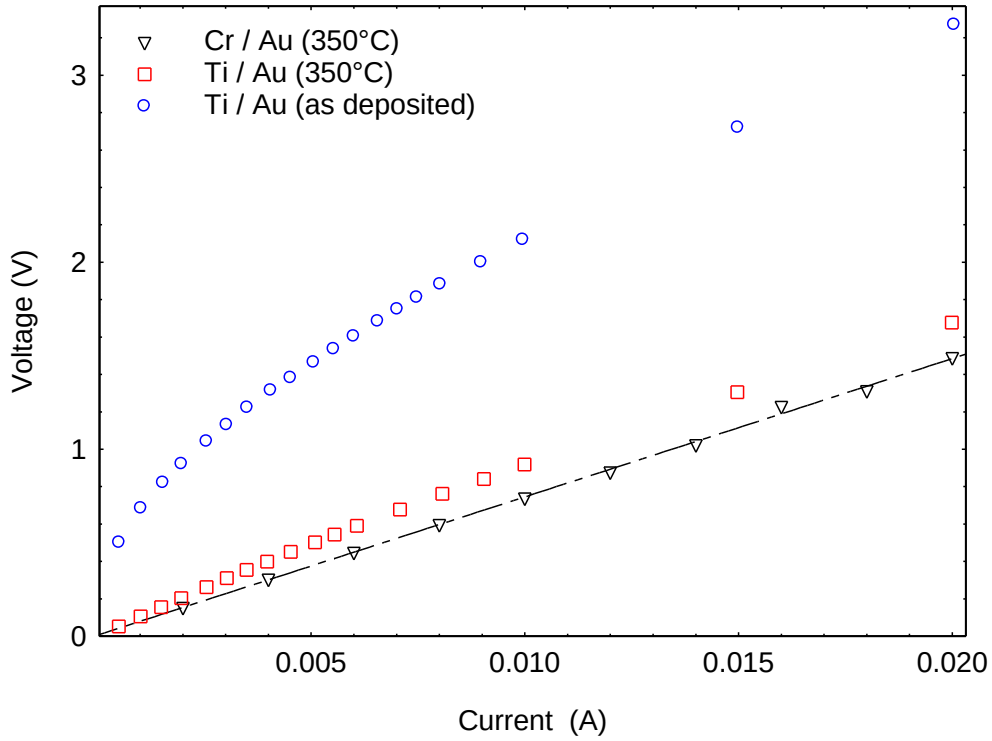

Figure 3-4: I-V characteristics for metal-semiconductor interfaces, including Ti / Au as-deposited on p-GaAs, together with Ti / Au and Cr / Au annealed at 350°C.

Several of the lasers required separate contact pads so that injection into those regions of the device could be controlled independently. This required forming contact breaks in the metal film which was otherwise continuous across the sample. Due to the size of the contact breaks (typically 1 to 5 µm) and alignment tolerances, it was necessary to use EBL and then remove the metal using a suitable etchant with the resist acting as a mask.

3.2.7. Wafer Thinning and Chip Cleaving

For the sample to be cleaved into individual lasers it must first be thinned, typically to 100 µm by lapping the backside with a rotating silicon-carbide disc. As the samples are mounted *epi-side up* and GaAs is a poor thermal conductor (0.55 $Wcm^{-1}K^{-1}$) the thinning process also improves heat extraction from the active region of the laser, which is particularly important when operating at high duty cycles.

3.2.8. Chip Mounting and Wire Bonding

For convenience all experimental setups are designed to accept 3-lead T05 transistor headers. Laser chips are mounted (n-side down) on these via copper heat sinks using Epo-Tex H20E silver loaded epoxy, which is also used to secure the 50 µm diameter gold wires connecting the transistor terminals to the laser contact. Two lasers or one multi-section device can be mounted per transistor header, with the casing of the header acting as a common earth.

3.3. Experimental Techniques

3.3.1. Segmented Contact Method

The segmented contact method or multi-section technique is a stripe length method based on the study of the amplified spontaneous emission (ASE) as a means to obtain the optical gain and absorption spectra of a light-emitting semiconductor material [Blood et al. 2003; Thompson, et al. 1999]. The device structure used for this technique, shown in Figure 3-5, is essentially the same as a standard edge-emitting laser diode but with 4 µm breaks in the *p-side* metal contact made at 300 µm intervals. Electroluminescence is produced from two of the sections which are connected to a pulsed current source in a way which allows them to be driven independently. Conventionally the two front sections are driven with the remaining sections acting as passive absorbers. This suppresses the round trip amplification so that the light emitted from the front facet results from a net single pass modal gain. It is often desirable to make additional measures to reduce optical feedback by damaging the rear facet. The light is then scattered by the irregular interface with only a small fraction being reflected back into the waveguide.

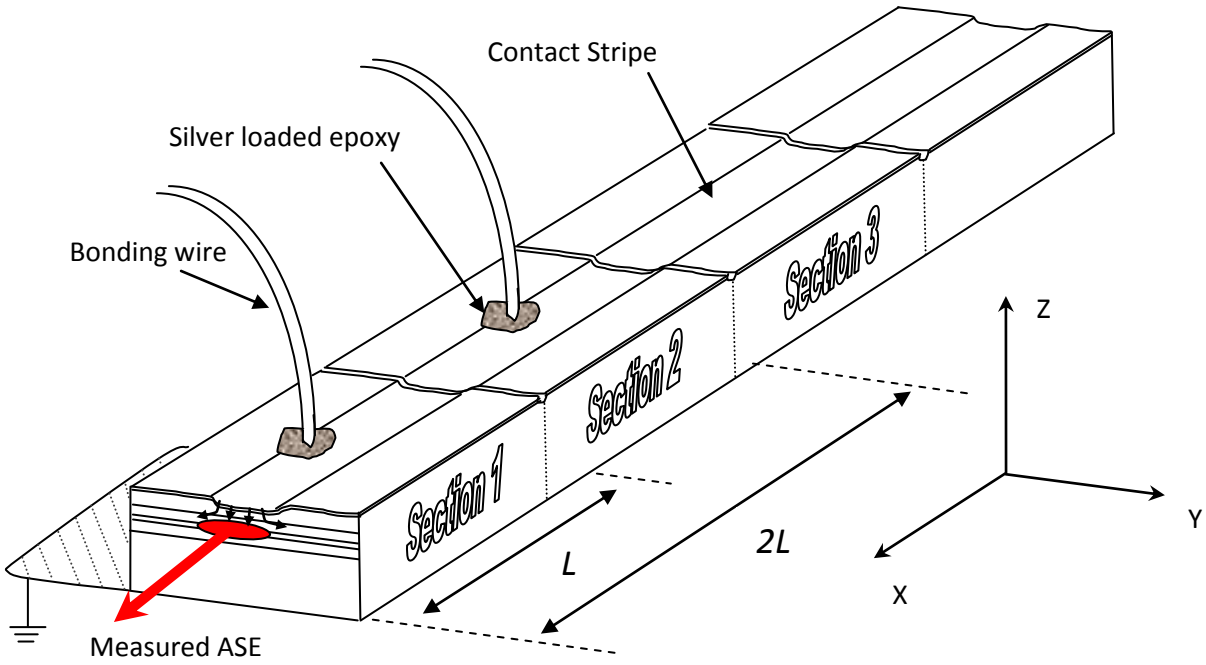

Figure 3-5: Schematic of multi-section device used to produce ASE. Gold wires are connected to the two front sections to provide electrical injection.

With reference to the axis labels in Figure 3-5, the light propagates along the waveguide in the x-direction, the y-axis is in the plane of the active region and the z-axis is normal to it. If a spontaneous emission event occurs in the active region (x-y plane), the rate of emission into a particular polarisation, per unit energy, per second, per unit area is given by I_{sp}. Amplification of the optical mode propagating in the x-direction $I(x)$, subject to a net gain $(G-\alpha_i)$, is represented by:

$$I(x) = \beta I_{sp} e^{(G-\alpha_i)x}$$

Equation 3-1

The coefficient β represents the fraction of spontaneous emission coupled into the waveguide along the x-direction. The ASE emerging from the front facet of the device after propagating a length L is found by integrating Equation 3-1:

$$I(L) = \int_0^L \beta I_{sp} e^{(G-\alpha_i)x} dx$$

Equation 3-2

$$I(L) = (\beta I_{sp}) \frac{e^{(G-\alpha_i)L} - 1}{G - \alpha_i}$$

Equation 3-3

Measuring the ASE originating from the front section alone, $I_{(1)}$ (*length, L*) and the front two sections together $I_{(1+2)}$ (*length, 2L*) the gain spectrum can be obtained. The net modal gain, which is the modal gain *G(λ)* minus the internal optical loss is given by:

$$G(\lambda) - \alpha_i = \frac{1}{L} ln \left[\frac{I_{1,2}(\lambda)}{I_1(\lambda)} - 1 \right]$$

Equation 3-4

The net modal absorption spectrum, given by the modal absorption *A (λ)* plus the internal optical loss, is obtained in a similar way except the ASE measured over the entire length *(2L)* is done without injecting current into section 1:

$$A(\lambda) + \alpha_i = \frac{1}{L} ln \left[\frac{I_1(\lambda)}{I_2(\lambda)} \right]$$

Equation 3-5

When taking ASE measurements to determine absorption spectra it is important to ground the section which is not being electrically driven. This ensures that any carriers leaking into the adjacent section are swept to ground, avoiding recombination in that section.

Typical ASE spectra obtained for each of the injection conditions described above are shown in Figure 3-6. The resulting gain and absorption spectra obtained by applying equations Equation 3-4 and Equation 3-5 are shown in Figure 3-7.

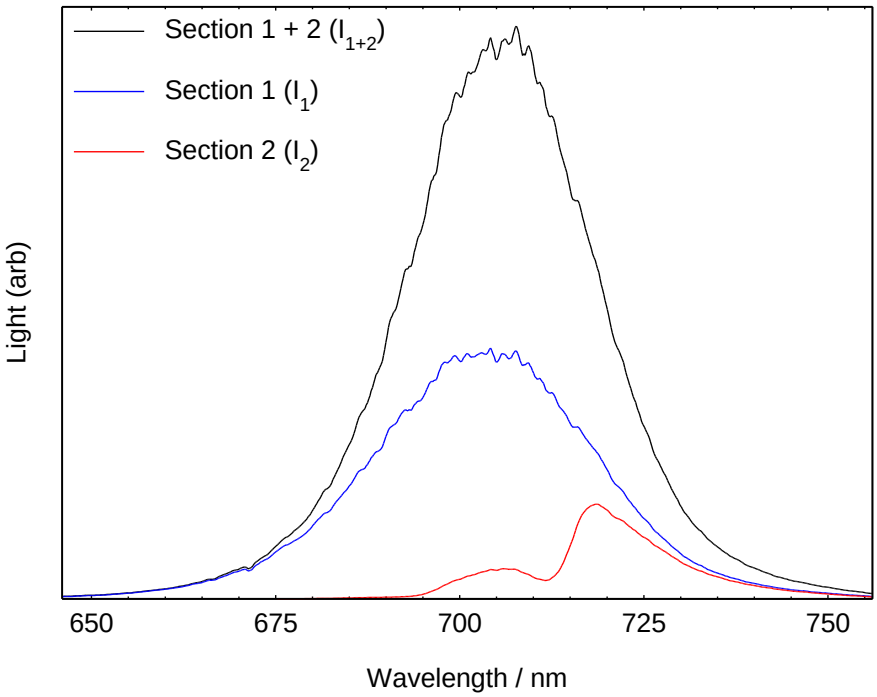

Figure 3-6: Amplified spontaneous emission spectra (ASE) generated by pumping section one only, section two only (with section one ground) and section one and two together. The noticeable kink in section 2 spectrum (~715nm) is due to absorption of dot states in section 1.

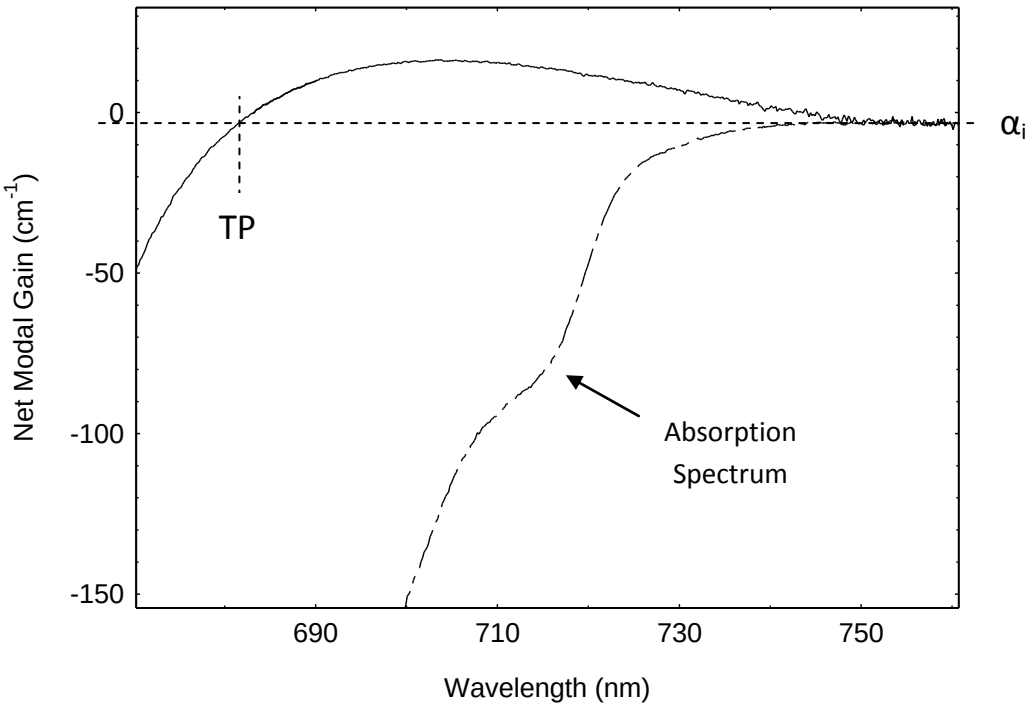

Figure 3-7: Gain spectrum (solid line), with absorption (shown here as negative gain) calculated from the ASE using Equation 3-4 and Equation 3-5. The dashed line indicates the point at which the internal optical loss (α_i) is measured and at high energy this line bisects the gain curve at the transparency point (TP).

At energies below the absorption edge (AE) the gain and absorption spectra converge to a value which represents the internal optical loss (α_i) of the material. The value of α_i is increased by processes such as scattering by defects or rough interfaces and therefore can reflect the quality of the material structure. For the example spectra shown in Figure 3-7, α_i is 3.5 cm^{-1} and the range of values quoted for this material system range from 2.5 to 6 cm^{-1}. Values below 1 cm^{-1} have been reported for InAs QD lasers with long cavities operating at low threshold current densities [Deppe et al. 2009]. Assuming that the internal loss is spectrally independent, the point at which the modal gain is zero at energies above the AE is called the transparency point (TP) and corresponds to the quasi Fermi-level separation *(ΔE_f)*. It is the TP which reflects the level of injection into the available states and quantifies how hard a device is being driven in terms of radiative processes. In this thesis the injection level is quantified by measuring the TP with respect to the AE, i.e. Injection level = |TP-AE|. The condition that gain can only be achieved at energies below the transparency point was stipulated by Bernard and Duraffourg, stating that the quasi-Fermi level separation must be greater than the energy of the photons released. The mathematics that describes this condition was derived from the Fermi-functions in Chapter 2.

3.4. Experimental Setup

Included in this section is a description of the experimental apparatus used to conduct measurements of: gain and absorption (using multi-section technique); lasing wavelengths; current-voltage-light-temperature *I-V-L-T* characteristics; power-current *P-I* (using an integrating sphere); near and far-field measurements and time resolved spectroscopy (using a Streak camera).

3.4.1. Multi-Section Measurements

The schematic in Figure 3-8 contains the components of the experimental setup used to measure the ASE from a multi-section device in order to obtain the optical gain and absorption spectra.

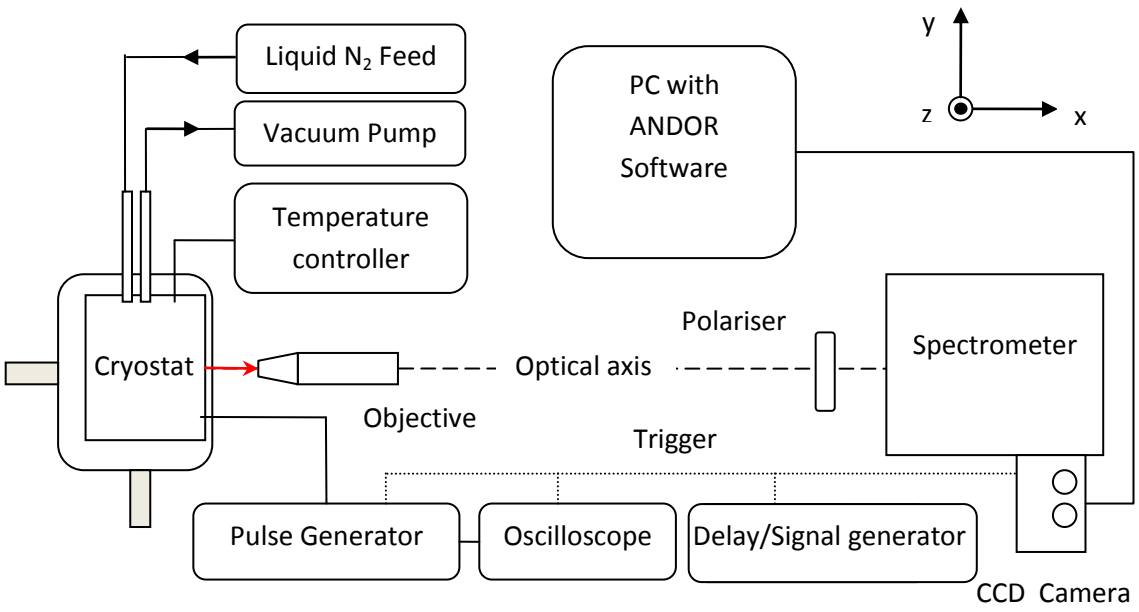

Figure 3-8: Schematic of the experimental setup used to measure ASE from a Multi-section device.

The device is situated in an Oxford Instruments MicrostatN cryostat which has a feed for liquid nitrogen, a vacuum line, electrical connections and a heating element which is controlled by an Oxford Instruments ITC601 temperature controller. This system allows measurements to be made in a temperature range of 80 – 400 ± 0.1 K. Current is delivered to the device by a pulse generator (built in house by Mr R. Tucker) outputting a 1 µs square pulse with a 1 kHz repetition rate. A switch box allows each section to be driven separately or together, allowing measurements of the appropriate ASE spectra. The light is collected by a lens which focuses the light from the facet of the device onto the entrance slit of an Oriel 74050 grating spectrometer via a polariser adjusted to accept either transverse electric (TE) or transverse magnetic (TM) polarised light. The device is aligned to the optical axis so that the plane of the active region is orientated in the x-y plane, orthogonal to the entrance slit of the spectrometer using a micro-positioning stage with six degrees of freedom. The spectrally resolved light falls onto a charge coupled device CCD array which has an image intensifier. The CCD is gated to the current pulse driving the multi-section device using a Stanford Research Systems digital delay/pulse generator, which itself is triggered by the current pulse generator.

The spectrometer disperses the light into the x-y plane of the CCD array so that the acquisitioned read out displays wavelength on the x-axis and vertical far field on the y-axis. Andor, the proprietary software of the camera, allows calibration of the CCD to display wavelength in terms of pixel number. This is achieved using an Oriel Hg/Ar spectral lamp and associated 'look-up' chart. Alignment of the device can be optimised by maximising the light signal, as viewed in real time. To improve the SNR of the measured spectra, a number of accumulations were taken, firstly of the background and then the signal.

There are certain requirements of the experimental setup which are essential to achieving good quality data. This often comes down to the geometry of light collection and the symmetry of electrical injection delivered to each section of the device (discussed in section 3.4.6). The former requirement manifests in the issue of collecting light from ‘un-pumped’ regions of the device, outside of the stripe width. The light emerging from such a region has been subject to passive absorption and a varying degree of dispersion than light passing along the waveguide under the stripe. Avoiding collection of unwanted light requires careful alignment of the device to the optical axis, correct choice of lens (numerical aperture NA and magnification) and the slit width on the spectrometer. Thorough descriptions of these issues are beyond the scope of this thesis but many of them are discussed in detail by Julie Lutti in her thesis [Lutti, 2005].

3.4.2. I-V-L-T Laser measurements

An experimental setup, built originally by K. Griffiths, was used to perform automated measurements of Current-Voltage-Light *(I-V-L-T)* characteristics as a function of temperature. The device is placed inside an evacuated cryostat comprising of a cold finger and heating element, which allows the temperature of the device to be varied from 150-400 K. Current to the device is provided by a constant-current pulse generator via a potential divider which is controlled by a stepper motor. The *I-V-L-T* measurement uses a boxcar integrator where the gates are set, using an oscilloscope, to coincide with the current/light pulse of the laser. The output of the boxcar and the

control input of the ancillaries are interfaced with a computer using an A to D card [Griffiths, 1997].

3.4.3. Near-Field and Far-Field measurements

A setup was created to measure near-field distribution of light emerging from the facet of a laser or multi-section device. The device is placed in a mount which provides electrical current via a pulse generator and the light from the facet is focussed onto a camera using a microscope lens. Since the width of the facet is known, the near-field can be calibrated by capturing an image of the facet at the same focal point at which the near-field was measured. Pixel number can then be converted to position along the facet and hence the characteristic full width half maximum (FWHM) of the near-field can be obtained. The near-field profile reflects the degree of current spreading in the active region of the device and since the length of the device is known, the current density can be calculated. However, as previously discussed (Chapter 2.) the optical profile evolves as the rate of stimulated emission increases and in this regime, the FWHM does not correspond to the level of current spreading. Current dependent changes in the near-field profile are only significant for emission that is close to the lasing wavelength. Therefore, as a solution, band-pass filters which pass only light from the tail of the ASE (i.e. at wavelengths where guiding is less prevalent), were positioned in the optical path of the laser.

The optical wave fronts are approximately planar in the near field, but spread out to show curvature in the far-field as described by Huygens' principle. This transition occurs at roughly w^2/λ, where w is the characteristic FWHM. A setup for characterising the far-field profile was created by Stella Elliott and is incorporated into the existing *I-V-L-T* rig. A preset current is passed through the device which is mounted at the centre of a turn-table and a photo-detector is used to collect light from the device as the turn-table rotates. This system allows the far-field beam profile to be characterised in both the vertical and horizontal plane [Elliott, 2010].

3.4.4. The Integrating Sphere

An integrating sphere allows the power output of a divergent light source to be measured in real units and was used in this work to obtain the *P-I* characteristics of the fabricated laser diodes.

The specific apparatus used here consists of a Nova II power meter and an Ophir 3A-IS detector head containing two spheres. The first sphere has a small hole into which the laser device is inserted and the mount for the laser is designed such that the amount of light entering or exiting the sphere is minimised. The inside surface of the sphere is coated with a highly reflective material which is insensitive to polarisation. After multiple reflections, the light passes into a second sphere, where it is incident on a detector. The output of the detector is interfaced with a power-meter which gives background corrected readouts. When measuring the power output of a device the main source of error manifests in how the device is orientated within the sphere. Due to the highly divergent nature of the laser beam, some of the light emitted from the facet can pass straight through to the second sphere and onto the detector, thus giving an incorrect value of 'integrated' power. The way in which the device is mounted means that the amount of light passing directly into the second sphere depends on the orientation of the header/laser device. To eradicate this issue, the devices are always placed in the sphere in the same orientation so that comparatively measurements are accurate, to at least 5%.

3.4.5. Streak Camera System: time resolved spectra

A Streak Camera system provides a means to determine time resolved images of short light pulses (resolution of ≈ 200 fs is offered by the best commercially available cameras) [Hamamatsu Photonics]. The output image preserves the spatial distribution of the source in one dimension, or spectrally if used in conjunction will a spectrometer placed between the device and the entrance slits. This provides a powerful tool for obtaining time-resolved near-fields and emission spectra of laser diodes.

The Streak camera used to obtain results in this thesis was manufactured by Hamamatsu, consisting of a C5680 Streak unit incorporating a C4742-95 CCD. A Bentham monochromator, with a 150 line/mm (650 nm blaze wavelength) grating, was

used to provide a spectral range of approximately 80 nm. At the compromise of high spectral resolution, this grating was necessary when measuring the output of the dual-wavelength devices featured in Chapter 6, as the range it offered allowed the temporal evolution of both light pulses to be observed simultaneously.

The camera has an external trigger input, which was utilised to synchronise light capture with the current pulse delivered to the laser device. An example image of a laser diode emission spectrum taken over a 500 ns pulse width is shown in Figure 3-9.

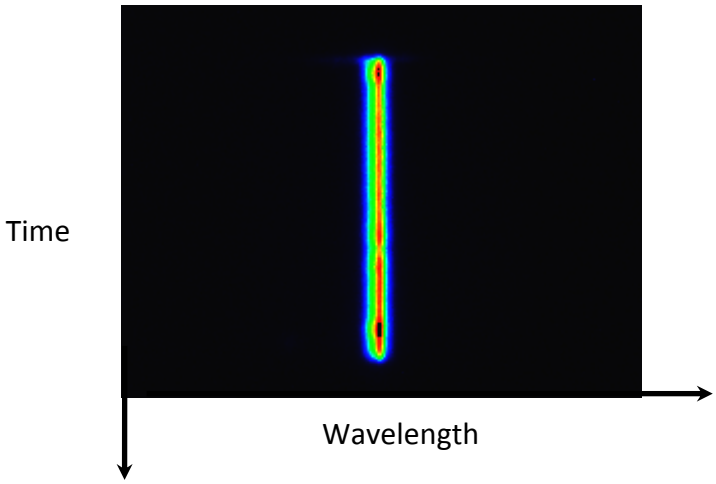

Figure 3-9: Streak Camera image capturing the light pulse over a 500 ns duration. Colours indicate the relative intensity of the light, graded from blue (low intensity) to red (high intensity).

3.4.6. Device Checks

Device checks made on the multi-section devices include measuring the current-voltage *(I-V)* characteristics, near field profiles and the inter-contact resistance between the two sections. *I-V* characteristics of both sections must show agreement so that one can ensure that an equal portion of current is delivered to each section when they are driven together with a single pulse generator. A difference in the *I-V* traces implies that the effective area of electrical contact is not the same for each section. This may be due to either unequal length sections or problems with metallisation uniformity and oxide isolation along the stripe. The near-fields of both

sections should be approximately Gaussian-like and although the exact shape is not crucial, it is important that the profiles from each section are the same. Another important check is the inter-contact resistance (resistance between the two adjacent sections), which are typically between 500 and 1 KΩ, depending on the amount of doping in the cladding and dimensions of the etched gap. If the inter-contact resistance is too low then there will a significant current leakage from one section to the next and as a result the ASE will be amplified over a larger distance than intended. In addition this will also lead to incorrect current density calculations.

In certain instances, such as using a device comprising of few sections, the third section of the device can be earthed to further prevent any roundtrip amplification. This method also suppresses recombination in section three, by removing carriers leaking in from section two. If measurements are made in this way it is important to account for the loss of carriers from the pumped section to ground via the inter-contact. Failure to do this will lead to inaccurate calculations of the current densities within the pumped section. Figure 3-10 is a simple illustration of the current paths that occur within the device when driving the various sections (S1, S2).

Case a)

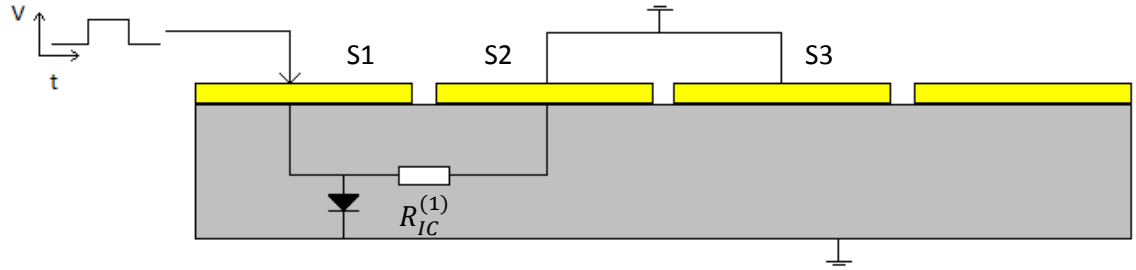

Case b)

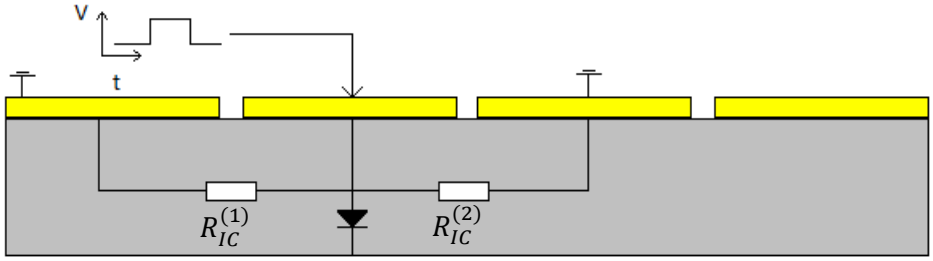

Case c)

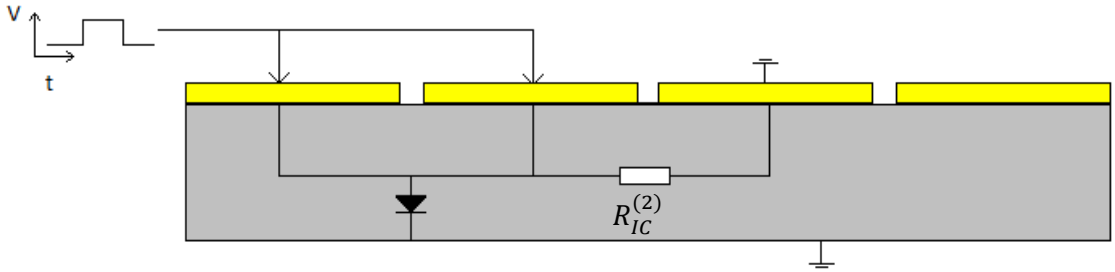

Figure 3-10: Leakage paths when driving a) S1 with S2 at ground b) S2 with S1 at ground c) S1 and S2

The inter-contact resistance in Figure 3-10, represented by a resistor R_{IC}, is in parallel with a diode corresponding to the *p-n* junction characteristic of the device. The influence of this resistor can be seen in the *I-V* plot of the device shown in Figure 3-11, where it is responsible for the extended linear portion before the diode 'turns on'. Fitting a straight line to this ohmic portion of the *I-V* plot allows the current passing through the resistor at each voltage to be found and hence the leakage through the inter-contact. This method of obtaining the leakage can be verified by measuring it directly for particular values of total drive current. To do this the voltage dropped across the device (V_{device}) for each drive current is measured and this is then divided by the appropriate value of R_{IC}, depending on which of the three cases in Figure 3-10 applies. Hence, the leakage current is:

$$I_{leakage} = \frac{V_{device}}{R_{IC}}$$

Equation 3-6

The current then contributing to the ASE is simply the total drive current minus the leakage. Failure to account for the leakage current may produce ASE spectra which leads to incorrect calculations of gain, in terms of the spectral dependence, the internal optical loss and the magnitude of the gain peak.

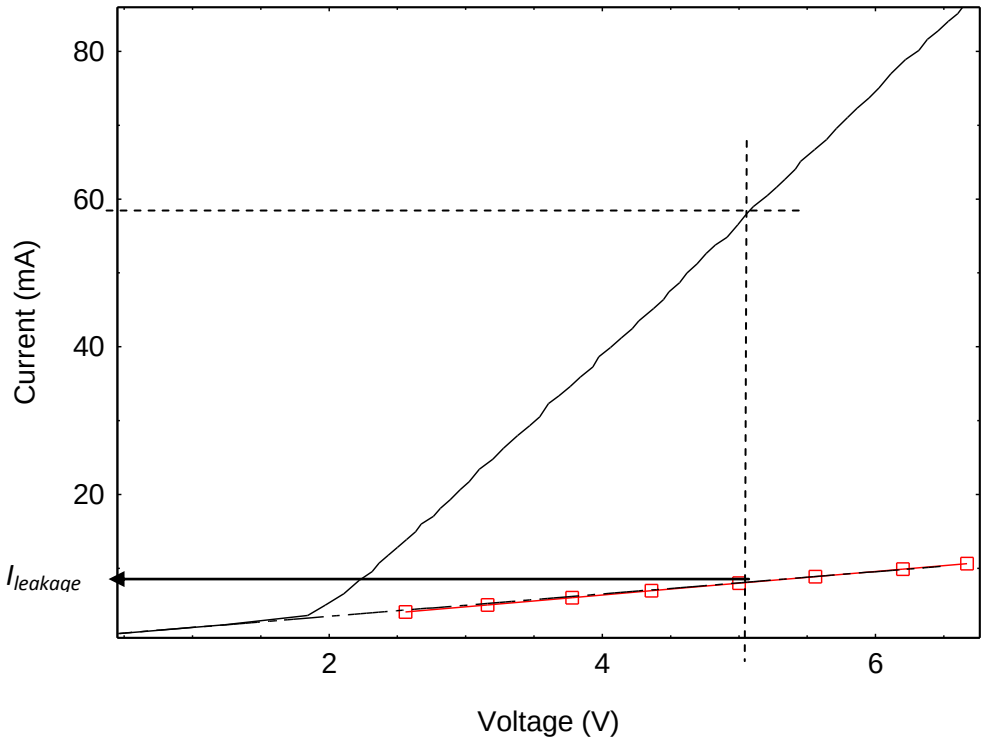

Figure 3-11: I-V characteristic for Case C) in Figure 3-10 with section 3 ground. Red squares show the I-V characteristic of the inter-contact. Arrow indicates example of finding $I_{leakage}$ from total drive current, with the difference being the current contributing to ASE.

3.5. Summary

This chapter has provided an overview of the key process steps which constitute the fabrication of RWG lasers investigated in this project. Included in this were details of some of the developments made in relation to incorporating deep etched photonic structures into RWGs with awareness to fabrication complexities. The remainder of the chapter described the experimental techniques used to obtain the results presented in this thesis and provided details on device testing criteria.

Sub-micron gratings were exposed using a Raith EBL system and the etch mask was defined using a *lift-off* process. Due to the proximity effect, the dose received by each feature needed to be adjusted in order to achieve desired line-widths. To establish the appropriate dosing required test pattern exposures were carried out using dose matrices. The profile of the resist and resulting mask definition was further enhanced by increasing the exposure of the PMMA along the outer regions of the ridge. Investigations into p-contact metallisation revealed that Zn/Au was not appropriate for contacting RWGs due to poor adhesion. Instead Cr/Au and Ti/Au contacts were tested and although both adequately adhered, Ti/Au was not suitable as the contact was still rectifying at an annealing temperature of 350 °C (upper limit at which BCB retains morphology). Therefore Cr/Au became the p-contact metallisation of choice for RWG lasers producing ohmic contacts with a specific contact resistance of $\approx 7\times10^{-5}\ \Omega cm^{-2}$ when annealed at 350 °C.

The segmented-contact stripe length method was performed on non-lasing test structures to obtain optical properties of each laser structure used, including modal gain and optical loss spectra (modal absorption plus internal optical loss). It became apparent that current leakage between adjacent sections could result in incorrect measurements of gain and absorption, since light was then amplified over distance greater than the contact length. To eradicate the effect, all adjacent sections not being electrically driven were earthed, preventing carriers from recombining across the junction. This technique of current compensation is particularly important when the inter-contact resistance between sections is low, which is often the case for sample which have highly doped cladding.

Chapter 4. Dry Etching Anisotropic Structures in InP/AlGaInP

4.1. Introduction.

In Section 2.5.3, it was established that the feature size of photonic structures in the smallest dimension depends on the refractive index, the order and the wavelength of light. The typical portion size of a grating fabricated in this work is between 100 and 500 nm. With an etch depth of 2.5 microns this results in aspect ratios as high as 25:1. To ensure effective coupling of light back into the cavity mode, it is important that the light is incident normal to each reflecting interface of the grating. For this reason it is desirable to have etched features with vertical sidewalls and relatively smooth surfaces. Producing an etch process which fulfils the above criteria can only be achieved using a dry etch method which is highly anisotropic. The etch mechanisms that need to be optimised in order to realise such an etch recipe for an InP/AlGaInP based material systems is the subject of this chapter. Plasma etching is a vast subject area and a full treatment of it is beyond the scope of this thesis. Developments which have been made build on the work done by Gareth Edwards and a detailed account of dry etching using an ICP source can be found in his thesis [Edwards, G.T., 2007]. The first two sections are intended to provide only a brief overview of plasma-assisted etching; however the level of detail provided is sufficient to understand the results presented in the sections that follow.

4.2. Plasma-Assisted Etching

There are several characteristics of dry etching which distinguish it from wet-etch methods. Dry etching provides greater control over the directionality and allows the vertical etch rate to proceed more quickly than the horizontal rate. The highly anisotropic features that can be formed in this way are not easily achieved using wet-etch methods. Although it can be made to preferential etch along a certain crystal direction, there is normally some undercutting of the masking material, especially for GaAs. In addition the reactive species of a wet-etch chemistry are generally more selective of particular epitaxial layers due to varying compositions and therefore is not

as suitable for etching high aspect ratio features. Wet-etching does offer a greater ability to selectivity etch a particular material, but in the context of etching RWGs or photonic crystals, this is seldom a sought-after characteristic. Moreover, best anisotropy is achieved when each layer in the structure is etched through at the same rate.

Plasma etching is a process whereby the material is chemically etched in the vicinity of the plasma by the reactive ion species which it contains. By giving kinetic energy to the ions of the plasma the etch rate can be enhanced; this is referred to as a *kinetically assisted chemical reaction.* This type of etching is both chemical and physical in nature and forms the basis of *reactive ion etching* (RIE). In the simplest explanation, the reactor of an RIE machine consists of two parallel plate electrodes (driven at a RF) and a feed for the gases, of which a small fraction is ionised to form the plasma. The electrode on which the sample sits is usually the RF driven with the other being RF ground. Due to electromagnetic effects, there is a region surrounding the electrode which the plasma is excluded from and this is referred to as the *sheath* [Williams, R.E., 1984]. The sheath potential can be increased in the vicinity of the sample electrode by making it smaller than the ground electrode. The magnitude of the DC *self-bias,* which is induced between the plasma and the sample electrode, is what determines the kinetic energy of the ions striking the sample. The velocity of the ions as they approach the electrode is perpendicular to the surface of the sample and it is this effect which is vital for anisotropic etching.

4.2.1. Etch Mechanisms

The plasma would typically contain a mixture of positive ions, electrons, radicals, neutral gases and photons. The common gases used to create the reactive species are oxygen, fluorine and chlorine. The process by which material is etched from the surface occurs in three stages: 1) the reactive species is *adsorbed* into the material surface, 2) a chemical reaction occurs and 3) desorption of the etch product. A detailed account of these processes is not required to understand the results in this thesis, but can be found in the literature [Coburn et al. 1979; Williams, R.E, 1984]. The overall etch rate is affected by each of these three stages and it is useful to determine which is

the limiting factor. Achieving the optimum etch conditions requires an understanding of the key etch mechanisms described below.

Chemical Etching:

If the etch is purely chemical then it requires no extra energy from ions arriving at the sample surface. The reactive species proceed to chemically etch the surface and as with wet-etching, the process is often isotropic, selectively etching the material which is most reactive. This can result in an undercut profile which is not ideal for etching photonic microstructures. The rate-limiting factor of chemical etching is often the removal of the etch product from the surface of the sample. If the etch products have low vapour pressures (low-volatility) then they will begin to accumulate on the surface, inhibiting the etch process. A schema of chemical etching is shown in Figure 4.1.

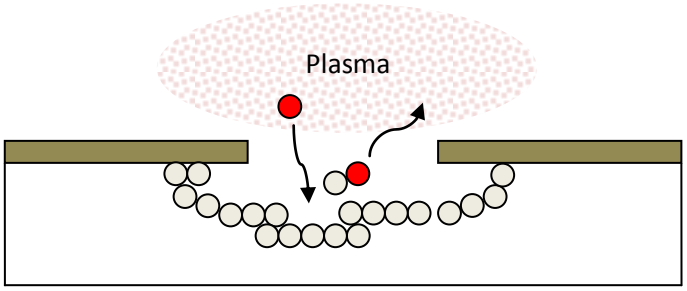

Figure 4-1: Schematic representation of purely chemical plasma etching. Resultant etch is isotropic.

Sputtering:

In contrast to chemical etching, sputtering is a purely physical process where the positive ions are accelerated across the sheath and collide with the atoms on the surface of the sample transferring momentum. If the energy given up in the collision exceeds the bond energy, then the atoms at the surface can be ejected and removed by the vacuum system. The chamber pressure must be sufficiently low so that the mean free path is long enough that atoms can escape the surface before they collide with a nearby molecule and redeposit on the surface. The physical nature of this etching mechanism results in poor selectivity between the semiconductor and the

mask. The etch rates achieved through sputtering are generally low and the collisions can cause significant sub-surface damage, altering the properties of the semiconductor.

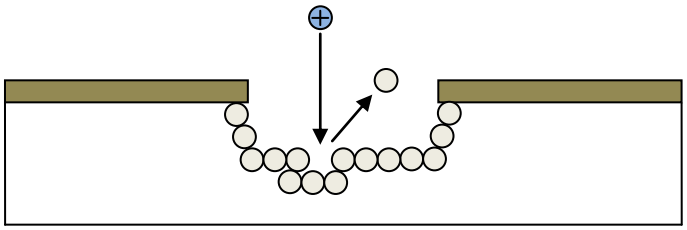

Figure 4-2 Schematic representation of sputtering (purely physical process). Results in a directional, anisotropic etch.

Kinetic Ion-assisted chemical etching:

This combines the effects of sputtering and chemical etching to produce vertical profiles and a substantial improvement in removal rate. The highly directional ions incident on the surface enhance the chemical etch rate by 'freeing up' the atoms of the semiconductor and also facilitate the removal of the etch product, which would otherwise passivate the surface. Since the ions are accelerated perpendicular to the sample surface, the horizontal etch rate is not kinetically assisted. The result, is an etch process that proceeds more rapidly in the vertical direction, producing the anisotropy necessary for creating the sub-micron wide high aspect-ratio features of DBR gratings. However, due to the large parameter space associated with this type of etching it can be difficult to establish the appropriate conditions. Determining the etch recipe which gives satisfactory results will often be done empirically.

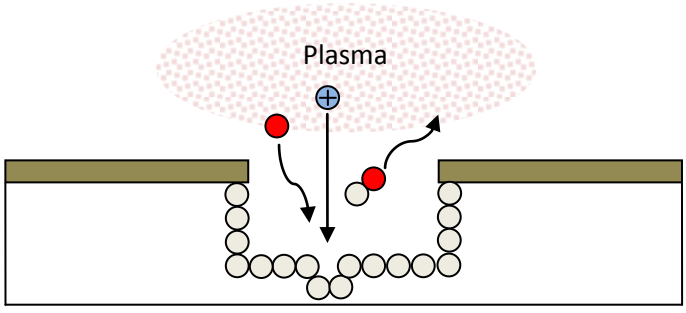

Figure 4-3: Schematic representation of ion assisted chemical etching. Resultant etch is anisotropic with vertical sidewalls.

4.2.2. Etch masks

A mask which is used to protect the sample from the plasma and define the etched features must fulfil certain criteria. Firstly, it should be sufficiently resistant to the etching process being used, so it etches at a slower rate than the material which it is masking. The ratio of etch rates between the mask and the sample is termed the *selectivity* and can be used to calculate the minimum mask thickness. The edges of the mask should be as vertical as possible and be free from imperfections as these will transfer into the material as etching proceeds. Similarly, if material is sputtered from the mask it can redeposit elsewhere on the surface producing unwanted features in the finished etch and this effect is known as *micro-masking*. The mask should not chemically react with constituents of the plasma or the etch products in a way which contaminates the surface of the sample, or the reactor chamber itself. Finally, it is important that the method used to remove the mask does not affect the patterned structures.

4.2.3. Etch profiles, faceting and aspect-ratio-dependent-etching

There may be several factors that could affect the resulting etch profiles, it could manifest in the mask quality, the material uniformity of the sample or in the mechanisms of the etch process itself. The SEM micrographs in Figure 4-4 (A) and (B) show some of the undesirable characteristics which can result from an incorrect choice of etch parameters. In the first image (A), the undercutting profile results from the lateral etch rate proceeding too quickly and suggests that the chemical etch mechanism is too high. Conversely, image (B) gives an example of an etch process which is very much dominated by the physical sputtering mechanism. In this etch the density of reactive species in the plasma was low due to an insufficient supply of the chemically active gases. The surface appears rough and a *trenching* effect is observed at the base of the sidewalls of the ridge (indicated in the figure).

The SEM image in Figure 4-4 (C) shows signs of an effect known as *faceting*, where the edge transition of the profile appears rough and uneven. This can be caused by a number of issues, but here it results from a poorly defined mask which has begun to etch through at the edges in the latter stages of the etching. Finally, the etched

features in Figure 4-4 (D) suffer from an effect known as *aspect-ratio-dependent-etching* (ARDE), sometimes referred to as RIE-lag [Gottsho et al. 1992; Chin et al. 1986]. It refers to the reduction in etch rate that occurs when the width of the feature reduces and is worsened as the etch proceeds to a greater depth. This effect limits the ability to create closely spaced high aspect-ratio features, such as those of a DBR grating, and ways to reduce it in the context of this material system formed a crucial part of this study.

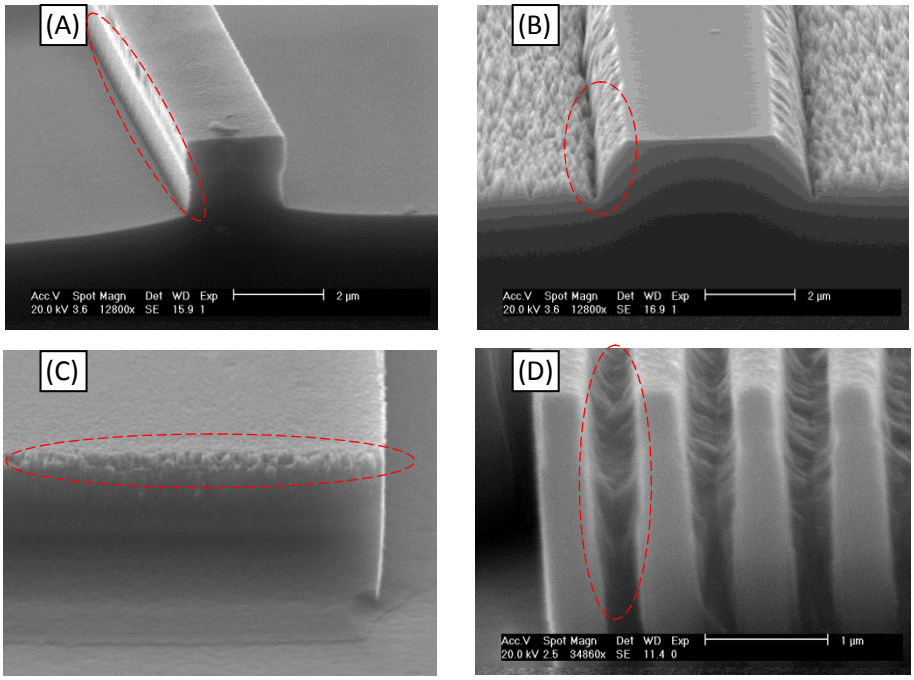

Figure 4-4: SEM micrographs showing (A) Undercutting, (B) effect of sputtering (showing effect of trenching), (C) faceting, (D) aspect-ratio-dependent etching (ARDE). Regions of interest are indicated by red dashed line.

4.3. Inductively Coupled Plasma Etching

An inductively coupled plasma (ICP) source offers greater control over the etch mechanisms because, unlike an RIE source, both the energy and flux of the bombarding ions can be controlled independently. The key advantage is that the flux can be made sufficiently high, without increasing the energy of the ions to a point that causes damage to the sample. A schematic illustration of an ICP chamber is shown in Figure 4-11. In an RIE reactor there is capacitive coupling between the electrode and the plasma, but in an ICP configuration the RF power is inductively coupled across a

dielectric wall. This approach allows plasmas to be generated with a high ion density but with low sheath potential between the chamber walls.

To maintain control over the ion energy, the stage on which the sample sits doubles as an electrode (essentially the RIE part of the reactor) and is capacitively coupled to the plasma. It is therefore more appropriate to refer to the reactor as an ICP-RIE source.

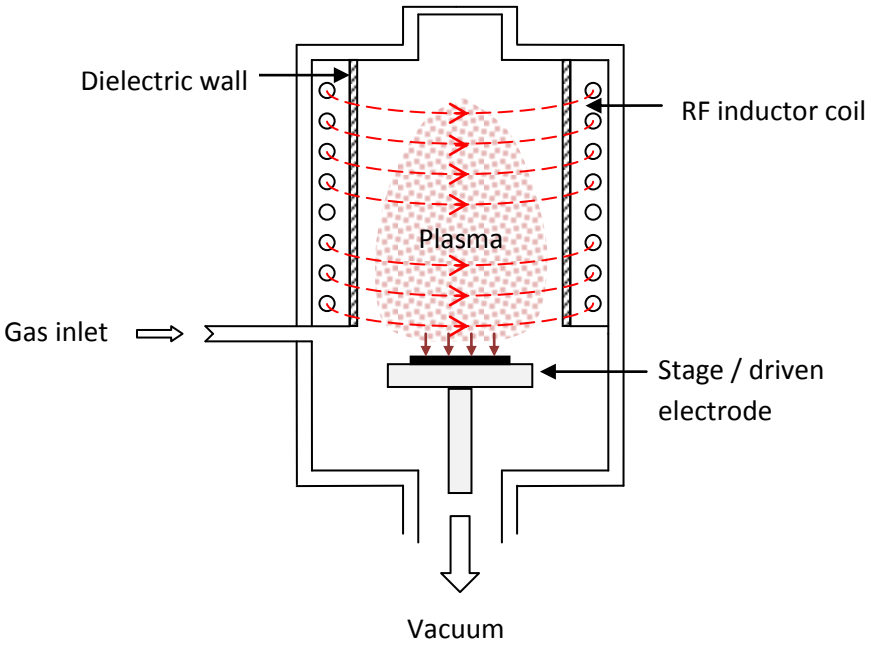

Figure 4-5: Schematic illustration of ICP source chamber layout. Sample located on top of the driven electrode.

4.3.1. Process parameters

Six key parameters can be adjusted to vary the characteristics of the plasma, and as such the mechanisms governing the overall etching conditions can become very complex. In this study four of these parameters were varied: temperature, RIE power, ICP power and gas chemistry. The other two parameters are gas flow and chamber pressure and these were not explored as a sufficient etch chemistry was achieved without making adjustments. The initial values that were found to be adequate were established by a previous study conducted by [Edwards, G.T., 2007], where the effect of varying these parameters was explained.

RIE power:

Increasing the RF power driving the sample electrode increases the DC bias and hence the sheath potential. Consequently, this raises the average energy of the ions arriving at the surface of the sample, and also increases the ion density, due to the higher number of ionisation interactions occurring in the plasma.

ICP power:

The applied RF signal in the inductor coil surrounding the chamber walls couples to the plasma electromagnetically causing the charged particles to undergo cyclotron motion. Increasing the ICP power thus induces more collisions within the plasma producing a higher density of ions, electrons and radicals. This inductive coupling mechanism allows the ion flux to increase with minimal increase in the ion energy.

Temperature:

The temperature can significantly affect the etching process by influencing the rate of chemical reactions and the removal of the etch products. In a plasma reactor, it is the temperature of the sample stage which is set by the user and the values quoted in this chapter refers to this temperature and not that of the plasma. However, in the proximity of the sample surface these temperatures are effectively the same.

Gas Chemistry:

Chemical etching can only take place if the process gases can react with the atoms of the sample to form a volatile etch product. The type of gas chemistry required depends on the constituent atoms that make up the sample. Therefore, when etching compound materials it may require introducing several gases into the chamber. In order to influence the directionality of the etching it is necessary to also add gases which are inert. The ions formed from these gases are used to facilitate the ion-assisted chemical etching process described in section 4.2.1.

4.3.2. Etching procedure

Many parameters affect the outcome of an etch process and this makes it difficult to form an exact analysis from which etch recipes can be derived. Instead, a more empirical approach is used and the optimised conditions which are established in this way may not necessarily transfer as a successful process in another reactor. Chamber history is also an important factor to consider when performing or evaluating an etch process. Reactors are often used to etch various material types including metals, resists and dielectrics which usually require introducing different gases into the chamber. To ensure consistent etches and eradicate spurious results, it is therefore good practice to remove contaminants by 'conditioning' the chamber prior to etching the sample. A typical condition would include first running an oxygen-rich plasma for at least 10 minutes, followed by a recipe using only an inert gas such as Ar. Finally a plasma containing the etch chemistry which would be used to etch the sample would be struck and run for a short period. When conditioning the plasma it is important to have the carrier wafer in the chamber to prevent etching the stage (RF electrode).

The reactor used to etch the structures in this study was an Oxford Instruments Plasmalab 100 system with an ICP380 chamber design. The sample is placed on a three inch Silicon wafer and transferred into the main chamber via a load-lock. The wafer is held in position by clamps and a flow of helium to its undersides ensures that the temperature of the wafer (sample) is kept close to the temperature-controlled stage (range of -100 to 400°C). The process parameters are set by the user and etching commences when the plasma strikes. The chamber has a small viewing port in the top to accommodate for a camera/laser-interferometer used to view the sample and monitor the etch rate/depth. The laser light, with a wavelength of 677 nm, partially reflects at the interfaces of the epitaxial layers due to a step change in refractive index. As the etching proceeds the thickness of the top layer reduces, causing the detected light intensity to oscillate sinusoidally between constructive and destructive interference. An example of an interferogram obtained from etching an InP/AlGaInP structure is shown in Figure 4-6. From the trace it is possible to infer the layers of the structure which are being etched and this gives the user the confidence to terminate

etching at the correct time. The depth *(d)* that is etched in one period *(T)* of oscillation can be calculated from the refractive index *(n)* and the wavelength *(λ)* of the laser:

$$d = \frac{\lambda}{2n}$$

Equation 4-1

Hence the etch rate *(R)* is given by:

$$R = \frac{\lambda}{2nT}$$

Equation 4-2

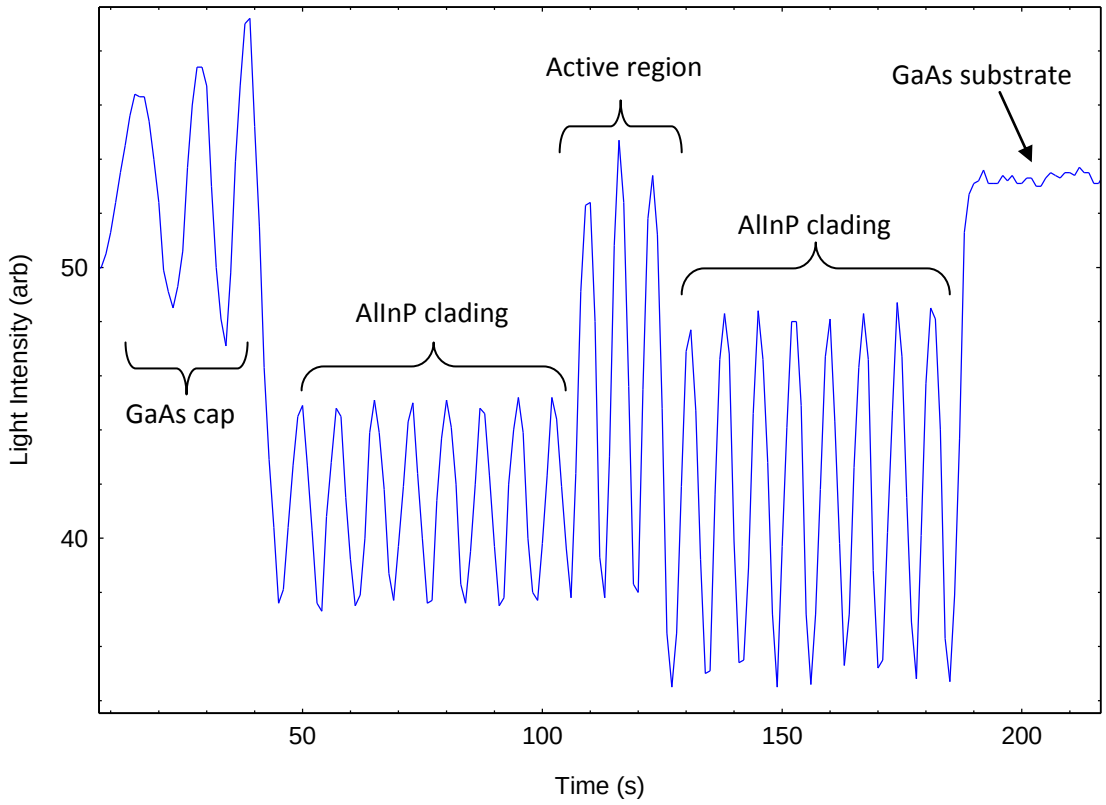

Figure 4-6: Laser interferogram obtained from etching InP/AlGaInP epitaxial structure.

4.3.3. Etching InP/AlGaInP

It was mentioned in the introduction that the work in this chapter builds on the developments previously made to etch InP/AlGaInP for sub-micron features [Edwards et al. 2006, 2007, 2008]. Etching was performed in a chlorine environment as this has proven effective for other III-V compounds due to the high etch rates and anisotropic etching that can be achieved [Yuan et al. 1997; Raffaele et al. 2001; Avary et al. 2001].

It was recognised that desorption of the etch product, namely $InCl_3$, was the etch rate limiting process. To assist in the removal of this non-volatile compound, the etching was performed at an elevated temperature of 180°C. The anisotropy required for etching RWGs with vertical sidewalls was established using the conditions summarised in Table 4.1.

Table 4.1: Summarises the etch parameters used in a previously optimised etch process for InP/AlGaInP [Edwards et al. 2008]

Etch Parameter	Value
ICP power	1000 W
RIE power	100 W
Sample Temperature	180°C
Ar flow	33.0 sccm (82.5 %)
BCl_3 flow	4.4 sccm
Cl_2 flow	2.6 sccm
Chamber Pressure	10 mTorr

Although this single stage process was adequate for etching RWGs, it was not suitable for etching sub-micron features such as those used in DBRs due to severe ARDE. After etching various combinations of compounds and alloys, the origin of this problem was found to be the GaAs cap, which proved reluctant to etch when in the confines of a grating structure. To resolve the issue the process was performed in two stages: the GaAs cap was etched at 25°C and the remaining structure etched at 180°C [Edwards et al. 2008]. Dichotomisation of the etch process is not ideal from a fabrication point of view as the sample must be unloaded from the chamber while the table temperature is raised to a stable 180°C - a process which can take around 30 minutes.

4.4. Etch development

The anticipated goal of this thesis is the creation of a dual-wavelength laser. To achieve this requires an etch process which yields the high aspect-ratio features necessary to form the particular device architecture, such as DBR gratings.

The etch study described in this section attempts to guide the reader through the developments made in this PhD, which led to a reliable single stage etch process suitable for RWGs and DBR gratings. With reference to Figure 4-7, are the characteristics of a ridge structure obtained using the previous etch conditions [Edwards et al. 2008]. Although the sidewalls appear rough, the main issue with the etch profile is the deviation from verticality in the lower portion of the ridge. Even though this occurs below the active region, any signs which indicate a loss of anisotropy in a ridge structure will become very apparent when etching the closely spaced features of a grating.

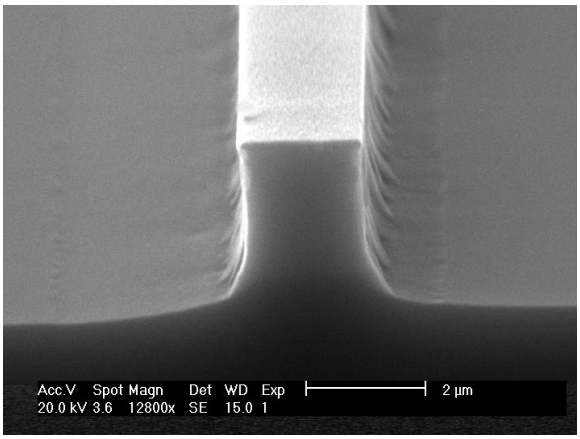

Figure 4-7: SEM micrograph of ridge cleaved to show the cross-section profile. Etch conditions were the same as those listed in Table 4.1.

In addition to a non-ideal etch profile, there was also variability between different etches run under the same input parameters. The cause of this was uncertain, but it appeared that the etch process was being operated in a sensitive region of the parameter space.

i) Changing gas chemistry:

It was hypothesized that sensitivity to the etch conditions could be reduced by simplifying the etch chemistry, by the withdrawal of BCl_3. Moreover, its removal would reduce the error in gas flow as the amount of Cl_2 introduced to the chamber could now be increased. To begin with the Ar content was left at 82.5 % and total volume flow rate of BCl_3 (4.4 sccm) was replaced by adding the same amount of Cl_2 (from 2.6 sccm to 7 sccm). Although this seemed to improve the reliability of the etching, it inevitably

increased the chemical etch rate. An SEM micrograph of the resulting etch process, shown in Figure 4-8 (A), is symptomatic of a structure which has been chemically over-etched. To reduce the chemical etch mechanism the Ar content was increased to 90 %, but as evident from Figure 4-8 (B), the ridge still has concave sidewalls.

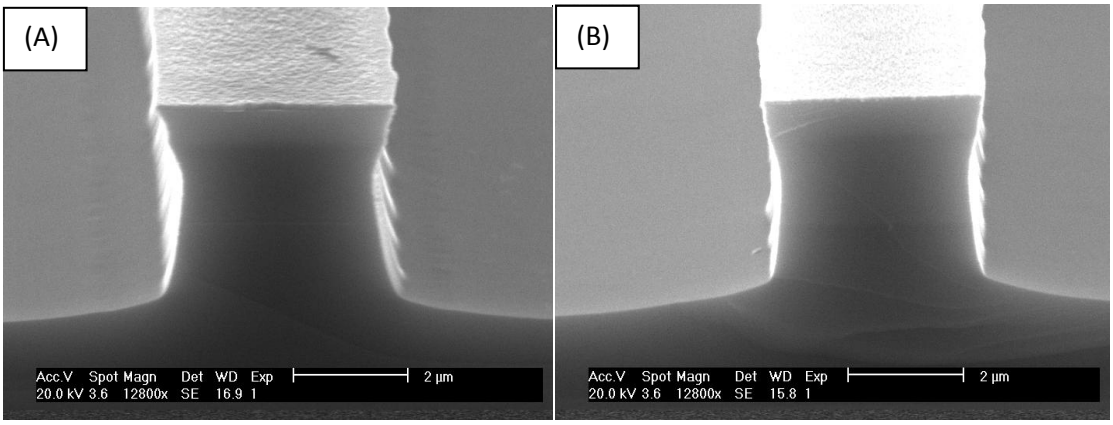

Figure 4-8: SEM micrograph of a ridge cleaved to show the cross-section profile for (A) 82.5 % Ar, 17.5% Cl_2 and (b) 90 % Ar, 10% Cl_2

ii) Changing Powers:

Increasing the RIE power increases the sheath potential, raising the energy of the ions impacting on the surface, and consequently increases the kinetically-assisted chemical etching mechanism. The RIE power was increased from 100 W to 200 W and to compensate for the associated rise in ion flux, the ICP power was reduced to 500 W. The resultant etch is shown in Figure 4-9 and a list of the etch parameters are shown in Table 4.2. There is a significant improvement in the verticality of the sidewalls, which extends down to the bottom of the ridge. Increasing the ion energy has increased the vertical etch rate relative to the horizontal rate enough to maintain anisotropy to a depth of at least 5-µm.

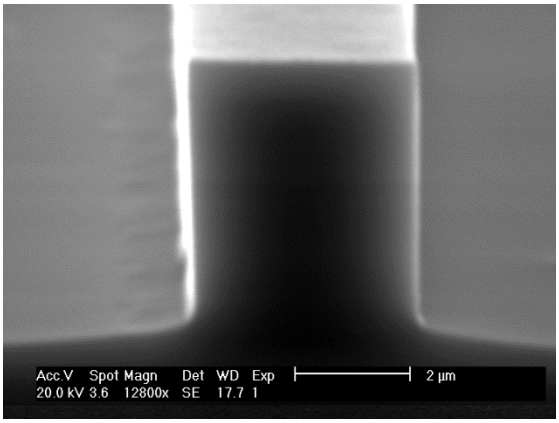

Figure 4-9: SEM micrograph of ridge cleaved to show the cross-section profile resulting from RIE/ICP powers of 200 W/ 500 W and Ar/Cl2 ratio of 9:1.

Table 4.2: Etch parameters used for anisotropic etching of deep-etched RWGs

Etch Parameter	Value
ICP power	500 W
RIE power	200 W
Sample Temperature	180°C
Ar flow	36.0 sccm (90 %)
Cl_2 flow	4.0 sccm
Chamber pressure	10 mTorr

4.4.1. Etching submicron high aspect-ratio gratings

Desorption and removal of the etch product $InCl_3$ is the rate limiting factor in this material system and the confines of a grating structure exacerbates this problem. Increasing the ion energy certainly improved the anisotropy in ridge structures and it was anticipated that the change in the RIE/ICP power and the withdrawal of BCl_3 would also improve the etching of closely spaced, high aspect-ratio features.

Submicron features in GaAs:

In order for a single stage process to be realised, the conditions need to suit anisotropic etching of both GaAs and AlGaInP. In terms of etch product removal, we are limited to using high temperatures for In-containing compounds. The image in Figure 4-10 shows a ridge etched under the same condition as that in Figure 4-9 except

for the temperature, which was reduced to 25°C. It illustrates just how significant the temperature is for the resulting etch profile. The etch rate at this temperature is less than half that at 180°C.

As mentioned in Section 4.3.3, closely spaced submicron features cannot be etched in GaAs with the existing AlGaInP recipe, due to the high temperature. The SEM micrograph in Figure 4-11 shows how the high anisotropy and low ARDE can be achieved for GaAs at high temperature, by adjusting the RIE and ICP powers from 100 W/1000 W to 200 W/500 W respectively. Interestingly, this combination of powers was not suitable for etching at 25°C - the temperature previously found to give satisfactory results.

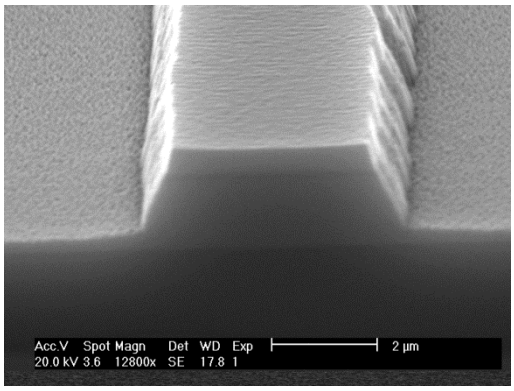

Figure 4-10: SEM micrograph showing the profile of an InP/AlGaInP ridge etched at 25°C. All other conditions were the same as those given in Table 4.2

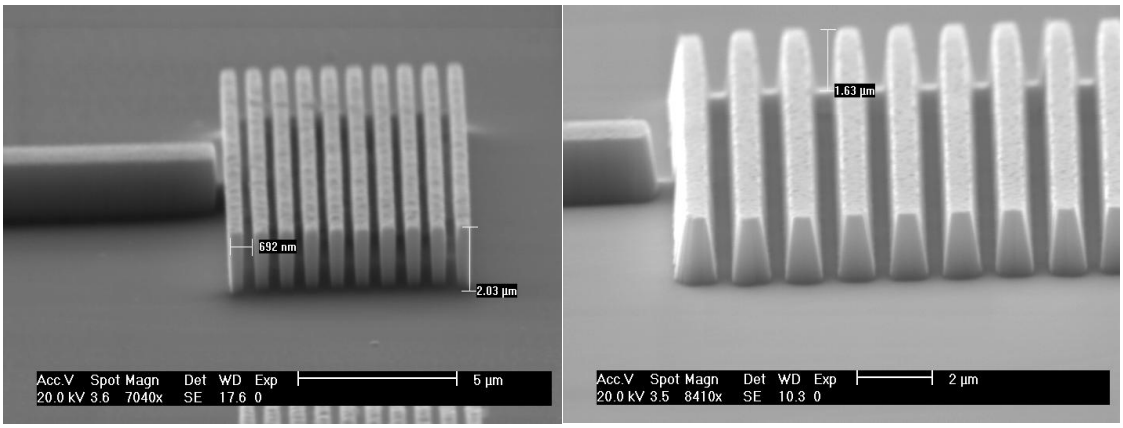

Figure 4-11: SEM micrograph of gratings structures etched into GaAs at (A) 180°C (B) 25°C.

Submicron features in InP/AlGaInP:

Using the conditions listed in Table 4.2, submicron features with varying line-widths were etched into an InP/AlGaInP QD sample. The dimensions of the patterned features (from 100 to 800 nm) were chosen to encompass the range of sizes that may be incorporated into a Bragg grating. The line-widths and the etch depths were assessed using the SEM and these measurements could be used to find the aspect-ratio and judge how vertical the side-wall profiles were. The etched features in Figure 4-12 show good verticality (close to 90 ° with respect to the un-patterned surface) with limited undercutting, but they also suffer from the effects of ARDE. Arrival of reactive species and removal of the etch product (normally the rate limiting factor), is 'choked' by the confines of the grating and the effect worsens as the depth increases.

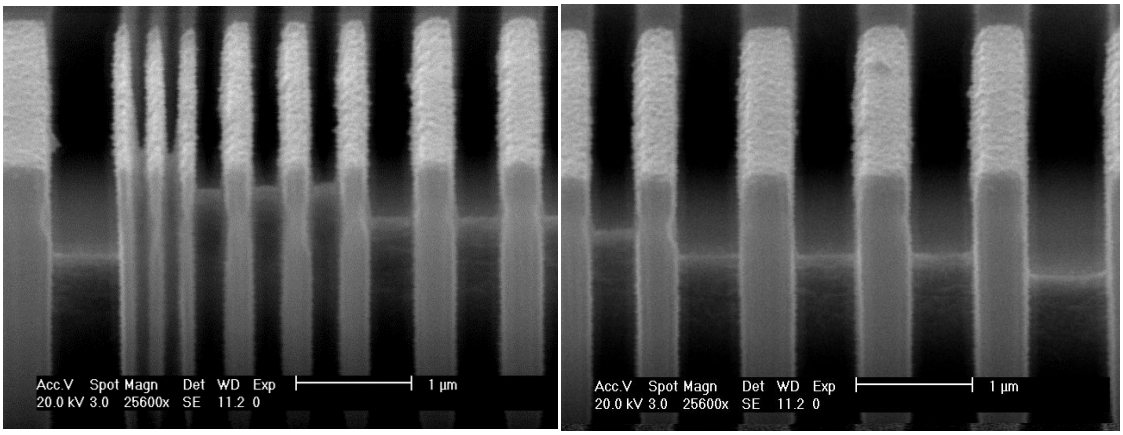

Figure 4-12: SEM micrographs illustrating the effect of ARDE for a range of line-widths. Etch conditions were the same as those listed in Table 4.2

Effect of temperature:

A sample temperature of 180°C is sufficient to increase the removal rate of $InCl_3$ enough to achieve deep-etched ridges with vertical sidewalls, so increasing the temperature beyond this had not yet been explored. Assuming the limiting factor associated with high aspect-ratio features was removal rate, raising the temperature further may increase the volatility of the etch product and reduce the unwillingness of the sample to etch within the confines of the grating. The plot in Figure 4-13 reveals how the etch rate of an un-patterned sample increases until 220°C and at some temperature between this and 240°C the etch rate begins to fall. This result suggests

increasing the volatility of the etch product yields an increase in etch rate until the evaporative effects begin to suppress adsorption of the reactive species.

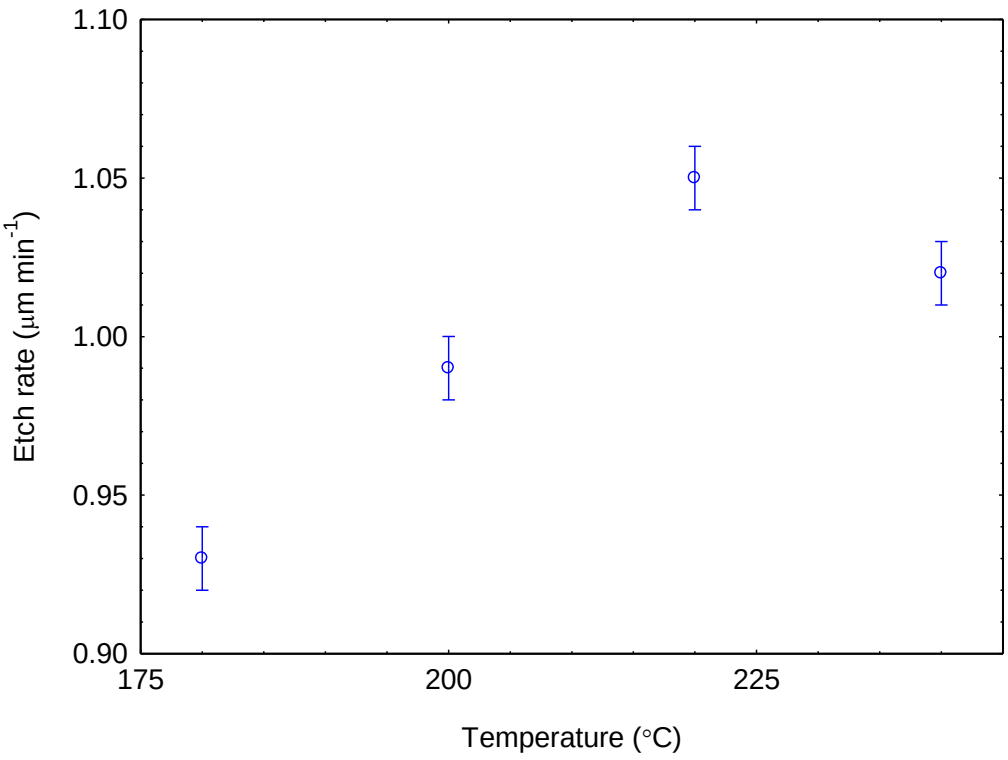

Figure 4-13: Etch rate of un-patterned InP/AlGaInP sample. All other etch conditions as listed in Table 4.2: Etch parameters used for anisotropic etching of deep-etched RWGs. Error bars indicate the error in determining the rates from the associated interferogram.

Based on this result, samples were patterned with grating structures and etched at 220°C. This was found to reduce the ARDE for InP/AlGaInP (Figure 4-14 (A)) and incidentally proved excellent for deep-etching submicron features in GaAs (Figure 4-14 (B)).

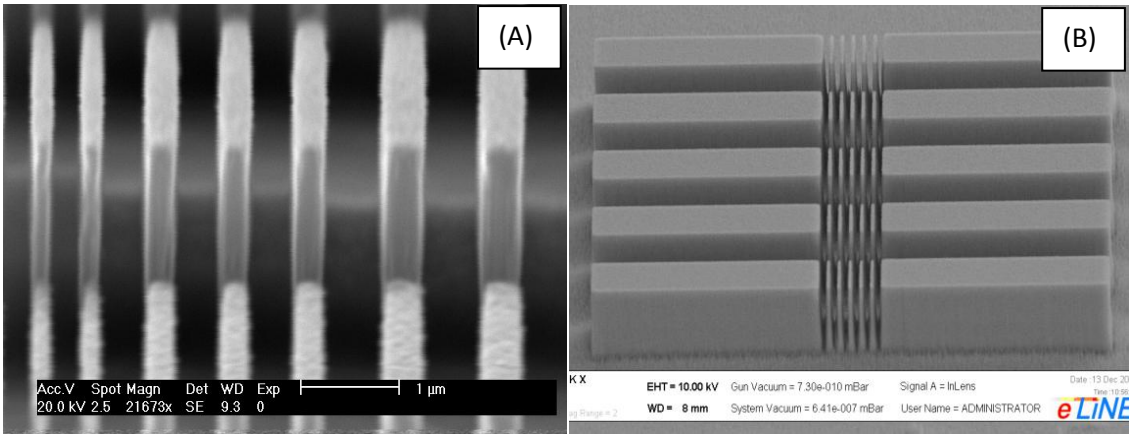

Figure 4-14: SEM micrograph for etching done at 220°C for (A) InP/AlGaInP laser structure and (B) GaAs.

Limitations of this etch process:

The modified etch recipe for InP/AlGaInP is sufficient for producing deep-etched gratings with portion dimensions equivalent to those required for 3rd order DBRs. The upper limit in aspect ratio (ridge height to width) was found to be approximately 25:1, but etching beyond this results in a loss in anisotropy. The reason for this is the limited ability to control, or rather reduce the lateral etch rate. The deeper the features are etched the longer the upper regions are exposed to the reactive species, resulting in structures which become progressively undercut.

Another factor consider which is difficult to quantify, is that RIE lag will be higher in the centre of the etched portion of the grating. For features of a certain line-width, this effect will be worsened as the lateral width (dimension normal to the periodicity) of the grating increases. To measure this effect requires the grating to be cleaved precisely through the etched gaps, which is difficult to achieve and makes any thorough investigation too sample intensive. In the calculations used to determine the reflectivity stop-bands the extent of the gratings was assumed semi-infinite in two dimensions so the mode only experienced a variation in refractive index in the direction of propagation. This was seen as viable approach as the gratings were deep-etch, extending into the substrate. However, if this were not the case along the centre of the grating, the effective index in this region would be slightly higher than that used in calculations. If significant, this would cause the reflectivity to be reduced and would cause the peak of the stop-band to shift to a longer wavelength.

4.4.2. Mask choice and Selectivity

Various mask materials have been employed in dry etching, with silicon-dioxide (SiO_2) being a common choice; but here the preferred mask material was nickel (Ni). The main reason for this was the higher selectivity it offered. Not only was the vertical etch rate lower, but importantly so was the lateral etch rate (governed mainly by the chemical etching process). The etch rate of Ni (≈0.01 µm[min^{-1}]) is relatively insensitive to variations in the etch parameters and as such the highest selectivity is achieved when the conditions give rise to the highest etch rate of the semiconductor. For the conditions found to be most suitable for etching photonic structures, the etch rate for InP/AlGaInP was 1.09 µm[min^{-1}] giving a selectivity with respect to Ni of at least 100:1. Improvements in the selectivity means a thinner mask can be used and the advantages of this are two-fold. Firstly, a thinner mask improves the ease and quality of the lift-off process and secondly it helps reduce the aspect ratio, enhancing the removal of the etch product from the confines of grating structures.

A Ni layer was thermally evaporated onto the exposed sample at a rate of 1 Åmin^{-1} to a typical thickness of 40 - 60 nm. The pattern was defined using a lift-off process as described in Chapter 2. Post etch, the Ni was removed using a solution of 1 part nitric acid to 19 parts de-ionised water.

Although raising the table temperature to 220°C produced the best result, in terms of etch rate and ARDE, it appeared to render the Ni impervious to the Nitric acid normally used to remove it. After researching the literature is was found that above 200°C Ni begins to inter-diffuse with GaAs to form a mono-crystalline structure [Ogawa et al. 1980; Dogan et al. 2008] and hence why it could not be removed from the surface. In view of this, several other mask materials were explored including titanium (Ti) and chromium (Cr), but these were also found to be unsuitable. In the case of Ti, the selectivity was very poor and Cr proved to give the same issues as Ni. Another attempt to remedy the problem was to deposit a thin layer of SiO_2 on the sample prior to evaporating the Ni, but to no avail; the mask could not be removed without damaging the etched structures. As a compromise, the table temperature was reduced to 200°C, which still gave satisfactory results in terms of ARDE.

4.4.3. Surface roughness

Reducing surface roughness is important for two reasons, firstly it will lower the non-radiative recombination process associated with surface states and secondly it will reduce scattering of the optical mode. Furthermore, for integrated photonic devices, or when the epitaxy is grown on a substrate that cannot easily be cleaved, the facets of the laser may need to be etched. Roughness in this case will cause a reduction in the reflectivity of the facet and this will affect the threshold gain condition and perhaps the beam quality. An investigation into this effect using the etch recipe derived in this work showed that the roughness, with a RMS value of 13.2 nm, gave an etched facet efficiency of 48 % compared with a cleaved facet [Thomas, 2012]. Within experimental error, this result concurred with the value calculated using a phase broadening model [Francis et al. 1996]. The reason for the roughness was ascribed to the mechanisms of the etch process but also the quality of lithography, where imperfections can lead to vertical striations in the etched-facet. Here measures were taken to improve the definition of the lithography and hence the mask profile. Firstly, samples in this study were patterned using a smaller electron beam step-size and the outer regions were exposed with a higher dose to improve definition as described in Chapter 3. Secondly, Ni was used as the mask material (defined using a lift-off process), and in terms of edge profile and etch resistance is superior to the etched-defined SiO_2 mask used in the study described above. It is therefore reasonable to suggest that the roughness due to lithographical processes would result in a facet efficiency of no less than 48 %.

In relation to etch chemistry, it has previously been established that the post-etch RMS surface roughness between ridge structures varies with Ar concentration with a similar dependence as the maximum etch rate [Edwards et al. 2007]. For Ar concentrations above that which maximises the etch rate (> 80 %) there was a sudden fall in the RMS roughness and this is the regime in which this etch recipe resides.

4.4.4. Etching RWG lasers with grating structures

All of the laser structures based on a RWG geometry where deep-etched through to the substrate (≈2.5 µm), using the etch recipe derived in this chapter. For convenience, the details of the suitable etching parameters determined during this PhD are

summarised here in Table 4.3 and an example of the type of devices which have been etched using this recipe are shown in Figure 4-4.

Table 4.3: Etch parameters used for anisotropic etching of deep-etched RWGs

Etch Parameter	Value
ICP power	500 W
RIE power	200 W
Sample Temperature	200°C
Ar flow	36.0 sccm (90 %)
Cl_2 flow	4.0 sccm
Chamber pressure	10 mTorr
Mask	Ni
Mask thickness	40 - 60 nm

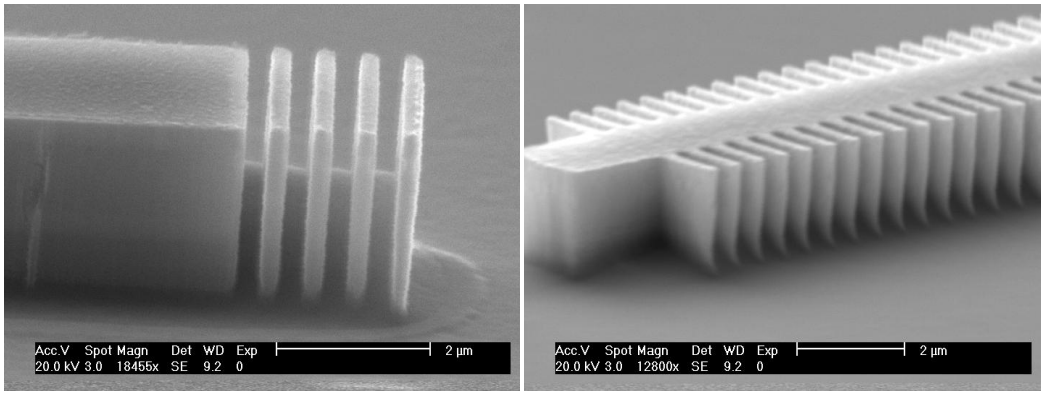

Figure 4-15: SEM micrograph of laser devices etched using the conditions listed in Table 4.3. Device (A) is a RWG with an end DBR grating and device (B) a lateral grating DFB RWG laser.

4.5. Summary

The development of a single stage etch process has been described which is suitable for etching anisotropic high aspect-ratio photonic structures in an InP/AlGaInP material system. By appropriable choice of RIE and ICP powers and the withdrawal of BCl_3 (used in the previous process) RWGs with vertical sidewalls could be etched to a depth of ≈ 5 µm. These process parameters were successfully used to etch closely spaced high aspect-ratio grating structures in GaAs, which had not previously been possible at high

temperatures. This allows for an increase in device throughput, as both the GaAs cap and the In-containing layers can be etched through in a single stage. The maximum etch rate (≈1.09 μm(min^{-1})) was achieved at a temperature of 220°C and a reduction in ARDE was also observed at this temperature, which was ascribed to the enhanced removal rate of the etch product, $InCl_3$. However, above 200°C the Ni mask could not be removed from the etched features and this was due to the Ni inter-diffusing with the GaAs cap. The selectivity of the semiconductor material with respect to the Ni mask was measured to be at least 100:1. Due to the large difference in etch rates, only a thin mask is required and this has several benefits. Firstly it reduces the thickness of PMMA required for a *lift-off* process, which means features can be patterned with a higher resolution, and secondly a thinner mask reduces the total aspect ratio ensuring ARDE is kept to a minimum.

The plasma etch recipe derived in this study has been used to etch all the RWG and DBR laser devices fabricated in this PhD and has proven to be a reliable process giving high device yield. As far as the author is aware, few etch recipes have been developed which are capable of etching high quality mesas in this material system. Therefore, without the development of this etch process, it would not be possible to form the deep-etched gratings which are integral to the operation of the devices produced in this work.

Chapter 5. Characterisation of Material System: Properties of InP Quantum Dots

5.1. Introduction

This Chapter describes the work which was carried out to establish a InP/AlGaInP QD structure suitable for creating a dual-wavelength laser. In the of context these devices, it is necessary to ascertain the range of wavelengths which can be accessed and importantly, understand how wavelength stability and threshold currents are affected by factors such as temperature and injection level. In this chapter, it is revealed how these properties are related to the way in which carriers populate the inhomogeneous distribution of electronic states. Characterising these effects was a prerequisite to designing the devices described in Chapter 6, and proved useful in understanding their performance.

In order to optimise or tailor the desired characteristics of an epitaxial laser structure in terms of the modal gain (or threshold current density), efficiency and the operating wavelength, it is essential that the effect of changes in the structure design and the growth conditions can be quantified and understood. Although the principle interest was to establish a suitable material for a dual-wavelength laser, the work carried out in this PhD helped to build on the recent advances which have been made in this material system, [Zundel et al. 1998; Walter et al. 2004; Smowton et al. 2005].

The first section of the chapter provides a description of the epitaxial layer structure in terms of the composition and dimensions, specifying the variations between each structure investigated. In the following sections, results are presented on the effect of growth temperature (T_{gr}) for structures that are otherwise nominally the same, using optical gain and loss measurements. These results are supplemented by threshold current density measurements made on corresponding edge-emitting laser devices with varying cavity lengths. The next section explains how tensile strain can be used to improve the temperature dependence of threshold current as well as further extend

the accessible range of lasing wavelengths. The following section describes the key mechanisms responsible for the super-linear rise in threshold current observed as operating temperature increases. The latter part of the chapter then deals with the temperature dependence of the gain-peak wavelength and reveals an interesting property unique to QD laser structures, the advantages of are useful for dual-wavelength sources and could potentially have benefits for lasers in a range of applications.

5.2. Epitaxial Structure

The InP QD laser structures were grown at the National Centre for III-V Technologies in Sheffield by low pressure metalorganic vapour phase epitaxy (MOVPE) in a horizontal flow reactor. The recipe used for the growth conditions was based on those previously used to produce InP QD lasers with low threshold currents [Krysa et al. 2007]. The constituents of the epitaxial structure were deposited on *n*-GaAs (100) substrates oriented 10° off toward <111>. Self-assembled dots were formed by depositing 6.5 Å of InP, at a rate of 2.5 monolayers per-second, on $(Al_{0.3}Ga_{0.7})_{0.51}In_{0.49}P$ and then covered with 8 nm $Ga_{0.51}In_{0.49}P$ QWs. Structures contained 5 layers of dots in wells (D-WELL)s where each D-WELL layer was separated by 8 or 16 nm wide $(Al_{0.3}Ga_{0.7})_{0.51}In_{0.49}P$ barrier layers. Forming the rest of the waveguide are 1000 nm wide $Al_{0.51}In_{0.49}P$ cladding layers. A schematic of the material structure is shown in Figure 5-1

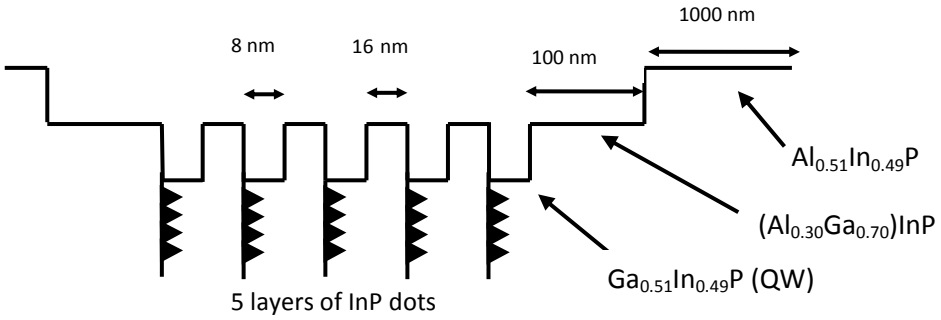

Figure 5-1 Diagram representing band-gap of material structure with growth direction in the horizontal plane. The triangular shapes represent the QD's within the GaInP quantum wells.

Wafers of this structure were grown at 710, 730 and 750°C. In addition, a wafer with tensile strain introduced into the QW was grown at a temperature of 730°C. Samples were processed into 50 μm wide oxide-isolated stripe lasers and non-lasing segmented contact devices (as described in chapter 3), all with cleaved non-coated facets.

5.3. Effect of growth temperature

Growth of InP/AlGaInP has previously been done using temperatures between 580 and 650 °C. The lower limit of this range was thought to, among other benefits, promote a higher density of smaller dots. However, this relatively low temperature is not ideal for the growth of GaInP/AlGaInP QWs on which the dots are formed. Suitable temperatures are in the region of 700 °C and can even yield a higher quality of InP without significantly affecting dot formation [Krysa et al. 2007]. This high-temperature growth approach has been used to demonstrate InP/AlGaInP QD lasers with low threshold current densities compared to those grown at the conventionally lower temperatures [Smowton et al. 2005].

This section quantifies the effect of systematically varying the growth temperature from 710 – 750 °C. Results are presented on the modal loss (revealing the relative dot density/energy distribution), net modal gain, internal optical loss and the resulting threshold current density of lasers with different cavity lengths.

5.3.1. Laser Measurements: Threshold Current Density

The three laser structures, grown at 710, 730 and 750 °C (all with 16 nm thick barriers) were cleaved into various lengths, with multiple devices of each length being mounted for experimental testing. Checks were made to ensure each device has the expected IV characteristic, and the optical near field profiles (FWHM) were measured to enable calculation of the current density.

The threshold current density (J_{th}) plotted as a function of operating temperature for 1, 2 and 3 mm long lasers is shown in Figure 5-2, with

Table 5.1 summarising the J_{th} values for each laser device at 300 K. For all cavity lengths, there is a super-linear increase in J_{th} with temperature and over the measured range; J_{th} decreases as the growth temperature (T_{gr}) is reduced. For the highest value

of T_{gr} (750°C), the difference between the 1 and 2 mm laser is less at higher temperatures than the other two samples. For example, at 350 K there is a 215 % increase in J_{th}, whereas the sample grown at 730° shows an increase of 352 %.

A standard method of quantifying the temperature dependence of the threshold current is to obtain the so-called *characteristic temperature (T_0)* [Coldren, L.A. & Corzine, S.W., 1995]. This value is extracted from a log plot of the threshold current versus temperature characteristic; however, in these QD structures the temperature dependence of the threshold current is not exponential over the measured range. As a result, T_0 can only be obtained over limited temperature ranges, and depending on the chosen range, the values can vary substantially. Therefore, a single meaningful value of T_0 cannot be determined for these lasers.

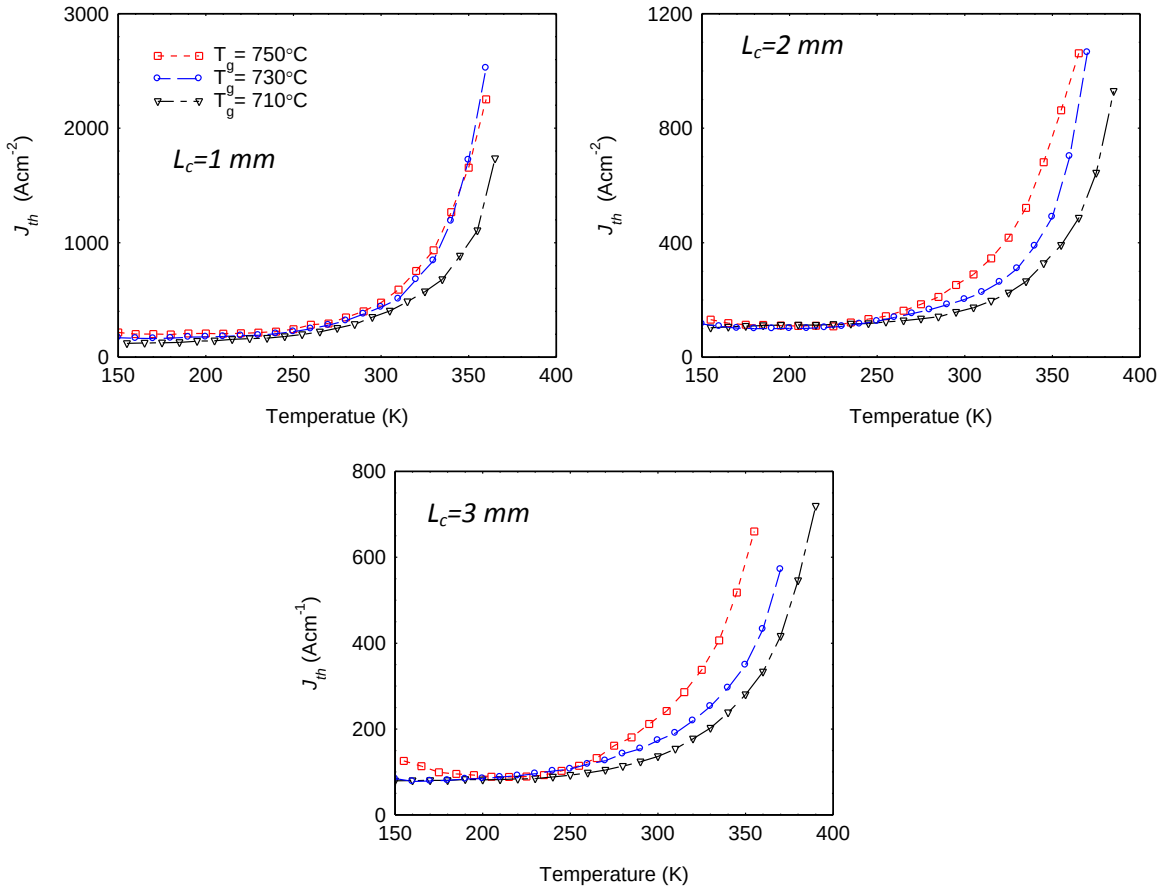

Figure 5-2 Threshold current density (J_{th}) vs. temperature for samples grown at 710°C (triangles), 730°C (circles) and 750°C (squares). Laser cavity length (L_c) is indicated on each plot.

Table 5.1 Gives a summary of laser threshold current densities at an operating temperature of 300 K.

	Threshold Current Density, J_{th} / Acm^{-2}		
Growth Temperature	1mm	2mm	3mm
750°C	480	270	210
730°C	440	200	170
710°C	375	165	135

5.3.2. Optical Loss and Gain Measurements

To understand how the growth temperature affects the optical properties of the active structure it was necessary to measure the optical loss of each material using the segmented contact absorption measurement. The spectra obtained, shown in Figure 5-3, reflect the optical gain that could be achieved if all energy states were fully inverted.

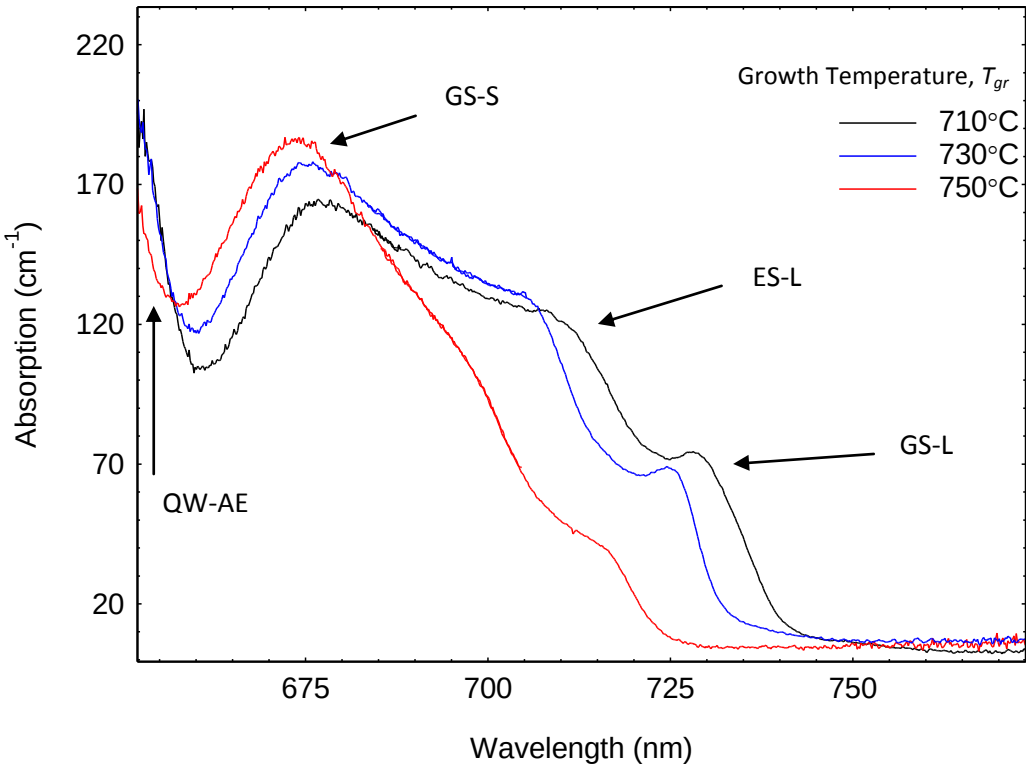

Figure 5-3: Optical loss spectra (sum of modal absorption plus internal optical loss) for InP/AlGaInP QD structures grown at temperatures of 710, 730 and 750°C. GS-L and ES-L indicate the ground and exited states of the large dot subset respectively and GS-S indicates the ground state of the small dot subset.

The presence of the GaInP quantum well (QW) is evident by its absorption edge (AE) labelled in the left of the figure, with the remaining features resulting from energy states formed by a bimodal distribution of dot sizes. The existence of which are confirmed by AFM images (Figure 5-4) taken after a single equivalent dot layer was deposited. Although AFM imaging can be useful in identifying whether a multimodal distribution of dot sizes exist, it should be noted that the exact dimensions of the dots determined in this way may not be representative of those dots formed in a complete growth. The samples selected for imaging are uncapped and the effect of cooling at this stage is believed to promote accumulation of surface species modifying the dot dimensions [Krysa et al. 2007].

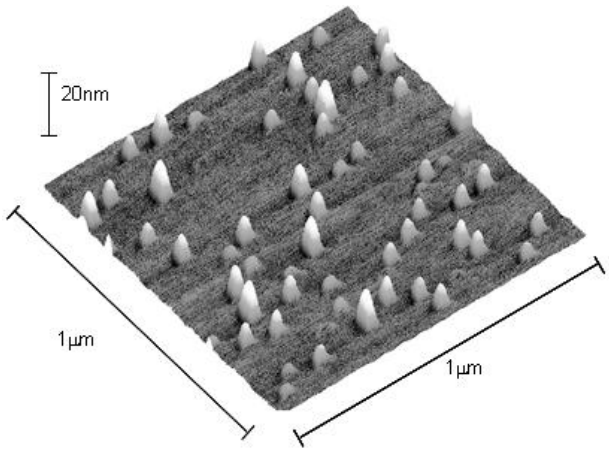

Figure 5-4: AFM image of strained single layer of uncapped InP QDs with showing a bimodal size distribution.

The two features at the lower energies, labelled GS-L and ES-L, correspond to the inhomogeneously broadened ground and excited states of the large dot subset [Al-Ghamdi et al. 2011]. The feature labelled GS-S represents what is believed to be the ground state of the small dot subset. As the growth temperature is varied, there is an obvious shift in energy of the inhomogeneously broadened ground and excited states of the large dot subset. The QW absorption edge is relatively unaffected by the growth temperature, whilst the shift of the dot states to higher energy states is consistent with the effect that increased growth temperature has on the size of dots formed. The reduced magnitude in absorption from the large dot states is most significant between 730 and 750^{o}C, where a reduction in the density of large dots may be due to an increased loss of material from the surface of the wafer at high T_{gr}. There does

however, appear to be a relative increase in absorption at energies associated with the small dot subset as temperature increases. As mentioned previously, the absorption spectrum below the band edge tends towards the value of the internal optical loss. These values were found to be 2.5, 5 and 4.5 cm^{-1} for samples grown at 710, 730 and 750^{o}C respectively. There appears to be no discernible trend between the internal loss and the growth temperature.

The net modal gain for each sample was measured at 300 K and the peak values of the spectra are plotted against current density in Figure 5-5. Each curve is fitted using an empirical relation [Ustinov et el. 2003];

$$G = G_0 \left[1 - exp\left(-\gamma \frac{J - J_0}{J_0}\right)\right],$$

Equation 5-1

where G_0 is the gain parameter (asymptotic value of gain at infinite current), J_0 is the transparency current and γ is referred to as a ideality factor. The sample grown at 750 °C has the lowest gain parameter, and its transparency current is also less, which is expected due to the lower density of large dot states. Within experimental error (± 2 cm^{-1}), the 710 and 730 °C samples have the same modal gain, G (not shown here) for a given current density and so the difference in laser performance can be attributed to the difference in α_i.

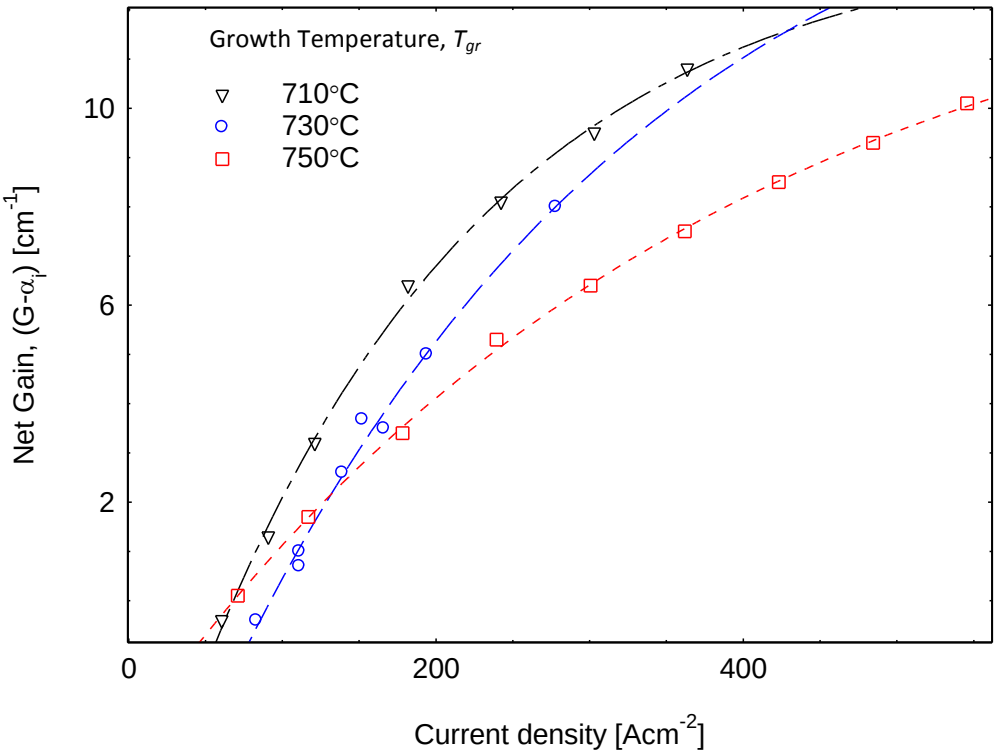

Figure 5-5: Net-gain vs. drive current density obtained from multi-section measurements, comparing effect of growth temperature.

5.4. Effect of Tensile Strain

As part of a recent study, a variation to the epitaxial structure given in Section 5.2 was applied to a wafer grown at 730°C, where the composition of the upper confining layer (UCL) was altered to induce either compressive or tensile strain, with respect to the GaAs lattice [Elliott et al. 2012]. The degree of strain was controlled by the fraction of Gallium (x) in the Ga_x $InP_{(1-x)}$ QW. Although strain can have deleterious effects on the quality of the wafer, for example introducing defects and non-radiative recombination centres it was reported that changing the composition of Ga from 0.51 (unstrained) to 0.54 reduced the temperature dependence of the threshold current. Based on the findings further measurements were carried out during this project to establish how this sample could potentially benefit a dual-wavelength device.

Later in Section 5.6, it becomes apparent that short (high mirror loss) cavities will be required to access laser emission at short wavelengths. Inherently, this leads to threshold currents that increase rapidly with operating temperature and as described in Section 5.5, this is largely due to the thermal spread of carriers among the

inhomogeneous dot states. Although strain cannot directly influence the thermal spread of carriers, it can be used to lower the threshold current due the effect it has on the band structure. Figure 5-6 illustrates the band structure of an unstrained and strained III-V semiconductor. For the unstrained case there is an asymmetry between the hole and electron effectives mass, where the heavy-hole band mass gives rise to a quasi-Fermi level which is above the top of the valence band. As such, the lowest energy levels have few hole states which can be filled by transitions from the conduction band. This means that the quasi-Fermi level separation required to reach threshold is higher than in a situation where the effective band masses are the same, as here the conduction and valence band would 'fill up' symmetrically with an applied bias. It was suggested [Yablonovitch et al. 1986] that introducing strain as a means to lower the valence band effective mass would reduce the asymmetry between the conduction and valence bands, hence lowering the lasing threshold current density. This reason for this becomes apparent by considering how the positions of the quasi-Fermi levels affect the transparency carrier density. For a given quasi-Fermi level separation the electron density is always lower in the strained sample and therefore transparency is reached at a lower injection current. In addition, the increase in gain with carrier injection (differential gain) is greater when the Fermi-levels sit closer to the band edge. This can be understood by considering that the differential gain is determined by the response of the band-edge carrier density to changes in the quasi-Fermi level. The Fermi function has a steepest gradient at the Fermi-level and therefore positioning it close to the band edge as possible will give the highest differential gain. The combined effect of reducing the transparency current and increasing the differential gain means that the threshold current required to reach a fixed gain is reduced. Although compressively strained material have not been used in this work, it is worth pointing out that compressive strain also reduces the valence band effective mass and can therefore be used to a similar effect.

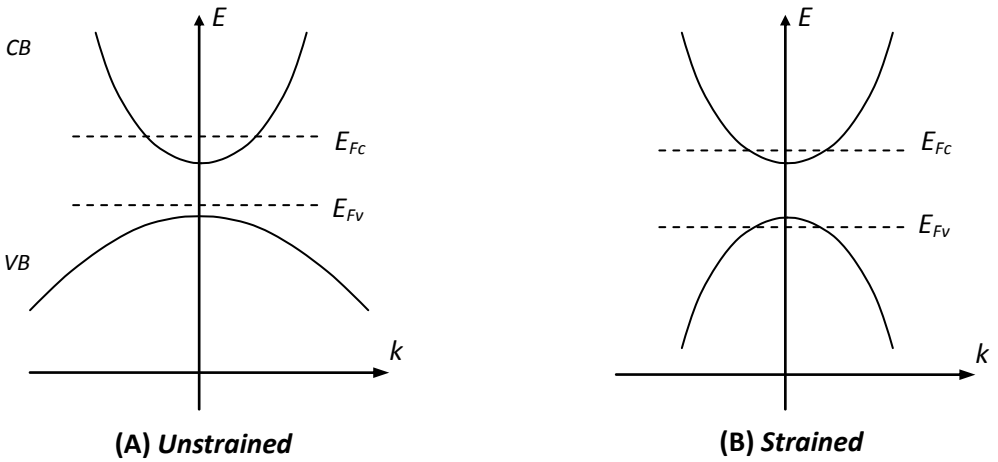

Figure 5-6: Band diagrams showing the positions of the quasi-Fermi level positions (E_{Fc}, E_{Fv}) for (A) unstrained and (B) strained material.

The structure grown with 54 % gallium in the QW gave promising results in terms of the threshold current dependence on operating temperature. Figure 5-7 shows data from measurements made on 1, 2 and 3 mm long lasers with 54 % gallium in the QW together with an unstrained sample with the same T_{gr}. The incorporation of strain has significantly reduced the threshold current density at elevated temperatures and this is most apparent when comparing the 1 mm long samples, with a 74 % reduction at 350 K. For the 3 mm samples, the difference is much less at 25 %. The internal optical loss of the two samples were found to be very similar at 5 and 4.5 cm^{-1}, so any variation in threshold current would presumably be due the effects of strain. Furthermore, differences in threshold current due to changes in band curvature would be most prominent at high injection (shorter cavities) as observed here.

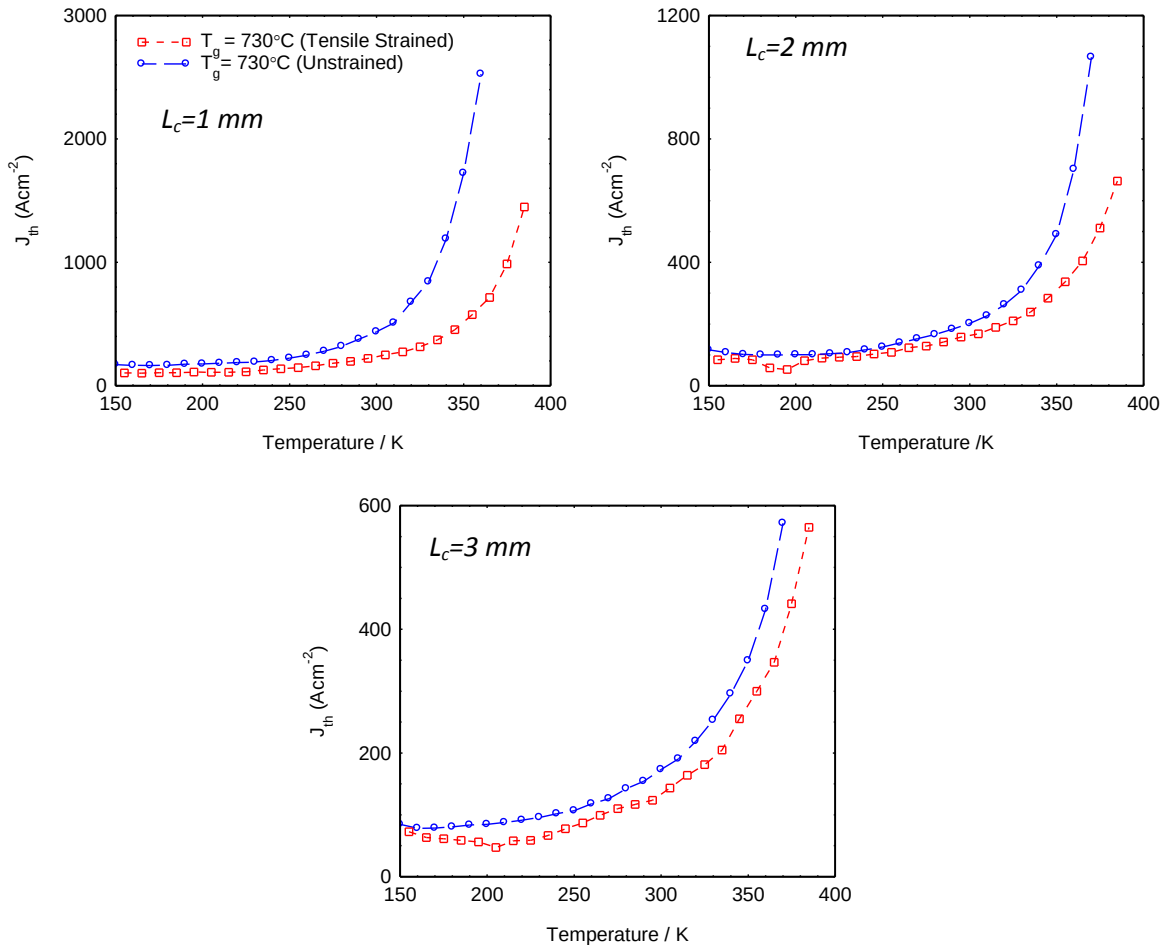

Figure 5-7: Threshold current density (J_{th}) vs. temperature for unstrained (blue circles) and tensile strained (red squares) samples grown at 730°C. Laser cavity length (L_c) is indicated on each plot.

It is evident from Figure 5-8, where a comparison is made from the modal absorption spectra of an unstrained sample grown at the same temperature, that the energy of the dot states has been shifted to higher energies.

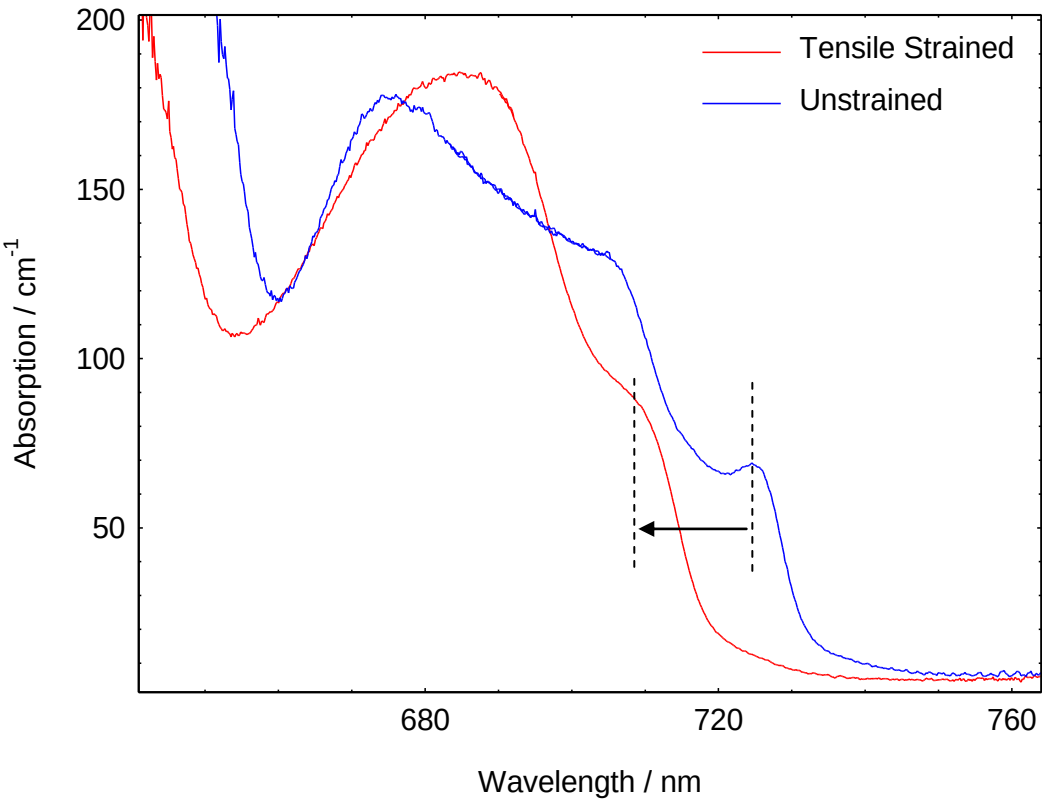

Figure 5-8: Comparing modal absorption spectra for strained (tensile) and unstrained UCL. Tensile strain has the effect of shifting the dot states to higher energies. The arrow indicates how the absorption feature due to the ground state of the large dot subset (depicted by the dashed lines) has been shifted.

The shift in energy of the dot states observed when tensile strain is introduced into the UCL causes a blue-shift in the gain-peak (G_{pk}) wavelength and so this process can be used, together with the growth temperature, to further extend the limit of lasing wavelength. The plot in Figure 5-9 shows the spectral position of the G_{pk} as a function of injected current density for QD active regions grown at 710, 750°C and a tensile strained structure grown at 730°C. It illustrates the extendable range of wavelengths that can be achieved by varying the growth temperature or introducing strain into the active structure. From the plot, it is apparent that the range of wavelengths that can be achieved from each structure depends on the current density. The gain-peak shifts with increasing injection due to state filling of the inhomogeneously broadened dot states and therefore it is the gain requirement, or equivalently the cavity loss, which determines the absolute wavelength. By appropriate choice of cavity length, the range that can be accessed from the materials shown here is approximately 705 – 745 nm.

The short wavelength corresponds to a 1000 µm long laser fabricated from the tensile strained structure and the long wavelength from a 4000 µm laser, which is unstrained and grown at 710°C.

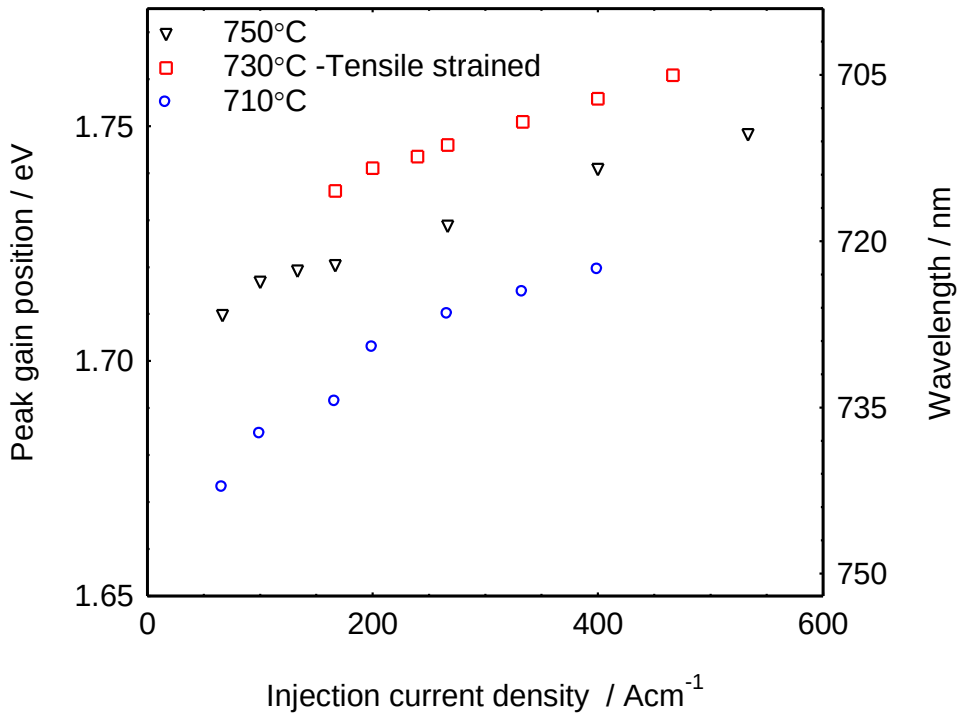

Figure 5-9: Plot of gain peak position vs. injection current illustrating the effect of varying the growth temperature from 710 °C (circles) to 750 °C (triangles) and incorporating strain into the upper confining layers (UCL)s of a sample grown at 730 °C (squares)

5.5. Temperature Dependence of Threshold Current

Measurements have been presented on the temperature dependence of threshold current density for lasers with various cavity lengths as a means to compare the performance of each laser material. This section attempts to explain the origin of the temperature dependence in InP QD lasers. In an idealised QD array the optical gain and hence the threshold current density is independent of temperature due to the delta-like density of states function. In a real QD system, there is a departure from this temperature-insensitive operation. The major culprit for the super-linear dependence observed at elevated temperatures is the thermal spread of carriers amongst the inhomogeneously broadened dot states. The presence of a wetting layer or QW, with a high density of states, can also lead to an increase in the threshold current as they become increasingly populated by thermal activation of carriers from the QD states.

From a design perspective, it is therefore attractive to fabricate a laser structure whereby the Fermi-level is be kept low with respect to higher lying states associated with the wetting layer or matrix. For instance, this could be achieved by incorporating deeper QDs that only require a small level of injection to achieve lasing threshold. As observed in the tensile strained samples, the level of injection can also be lowered by reducing the asymmetry between conduction-valence band curvatures.

Due to the inhomogeneous broadening associated with the two dot subsets there is a wide distribution of energy states. Operating a laser at an elevated temperature will cause an increase in the thermal spread of carriers among these energy states and consequently will contribute to an increase in the threshold current. The effect can be seen in the gain spectra plotted in Figure 5-10, where the change in transparency point (quasi Fermi-level separation) required to maintain a fixed peak-gain over a range of 100 K has increased by 32meV (11 nm shift).

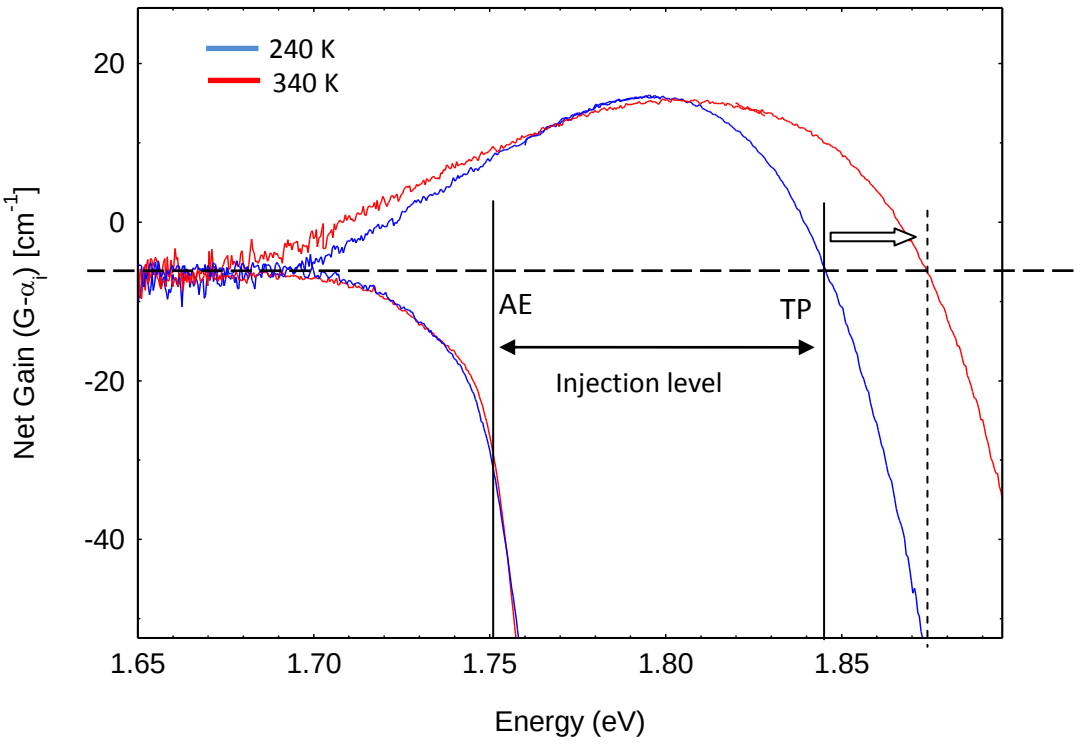

Figure 5-10: Modal gain spectra measured at 240 K (blue) and 340 K (red) together with absorption (shown here as negative gain). The spectra have been shifted to factor out the change in the band-gap with temperature. The arrow indicates the shift in the transparency point (TP) associated with the increase in injection required to maintain a fixed peak gain.

The increase in transparency with temperature is concomitant with a broadening of the gain spectrum, and for a fixed level of injection, this lowers the gain magnitude. The increase in injection required to compensate for this also affects the gain-peak wavelength and this effect is discussed in detail in Section 5.6.

At a fixed temperature, transparency was found to increase almost linearly with gain and this is demonstrated in Figure 5-11, where the injection level |Transparency point (TP) – Absorption edge AE| (defined in Section 3.3.1), is plotted against net peak-gain at 240 and 340 K. The plot also indicates the cavity lengths that correspond to a specific gain requirement. The increase in injection level with temperature increases as the length of the cavity is reduced, for example between 240 and 340 K the difference is 20 meV for a 1 mm laser, but only 4.5 meV for a 4 mm long laser.

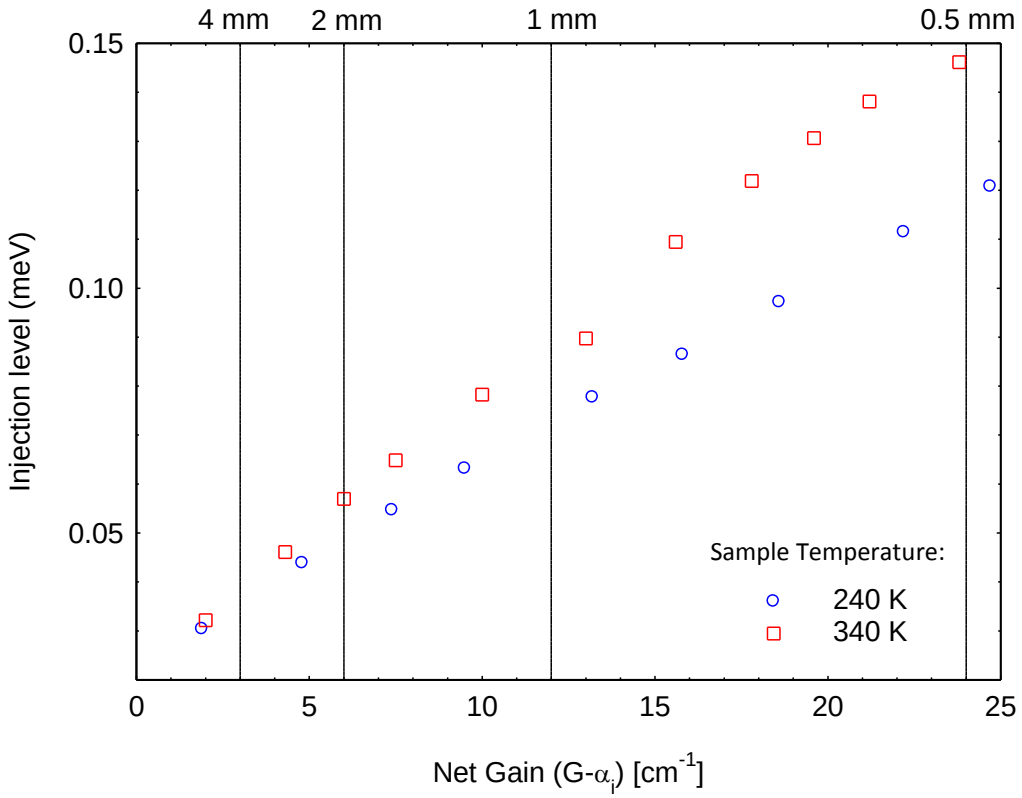

Figure 5-11: Illustrates the variation in injection level required to achieve the required net-gain at 240 K (blue circles) and 340 K (red squares). Vertical lines and labels indicate the laser cavity lengths

Increasing the cavity length reduces the required level of injection and so the quasi-Fermi levels sit lower down the ladder of energy states. Consequently, as the temperature increases the thermal spread of carriers to higher energy states is less and this lowers the temperature dependence of threshold current.

The thermal spread of carriers is not the sole cause of the super-linear rise in threshold current - it is accompanied by other 'parasitic' processes. The influence of these individual processes can be difficult to quantify accurately but are likely to include spontaneous emission, Shockley-Read-Hall (SRH) and Auger recombination (possible to a lesser extent in larger band-gap materials). The unamplified spontaneous emission spectra can be used to ascertain which energy states in the structure are populated with carriers and reveal where parasitic processes are manifested. The plot in Figure 5-12, shows the unamplified spontaneous emission measured from a top-window of a laser device for two levels of injection.

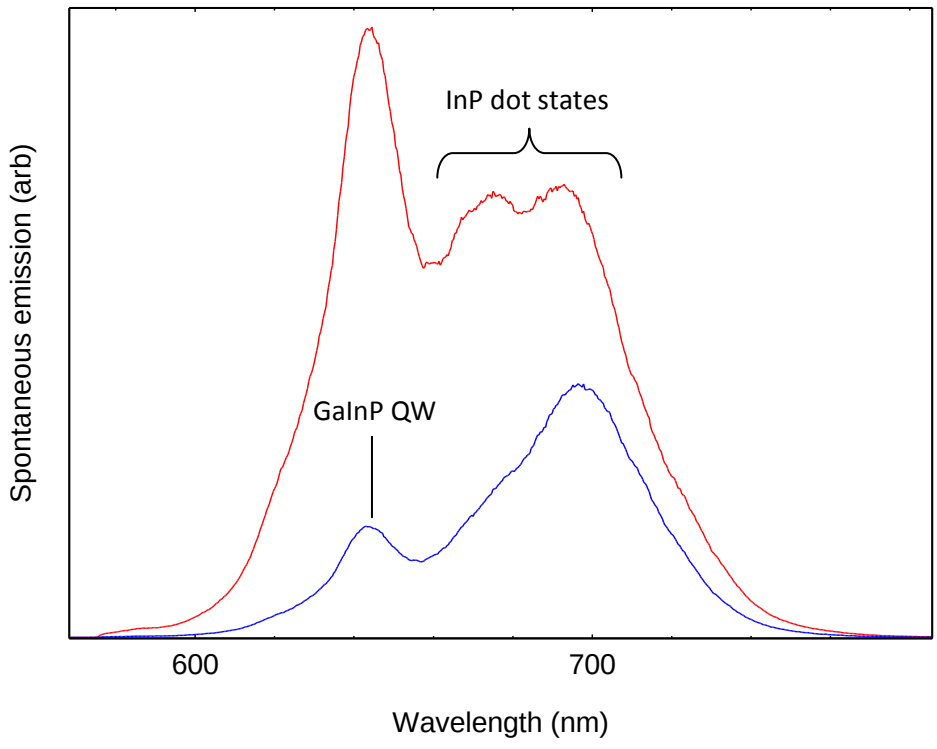

Figure 5-12: Room temperature unamplified spontaneous emission spectra for two levels of injection. Labels indicate contributions from the GaInP QW and dot states.

The presence of the GaInP QW is indicated at the short wavelength side of the spectrum, with the remaining contribution resulting from transitions of the

inhomogeneously broadened states of the small and large dot subset. At low injection, the emission is dominated by recombination within the dot states, particularly from the large dot subset. At high injection, emission from the small dot states is comparable with that of the large dots, and perhaps rather striking is the contribution from the QW, which constitutes a significant portion of the total recombination. At elevated temperatures, this effect is exacerbated by the increased number of carriers that are thermally activated into the QW [Smowton et al. 2011]. However, the study revealed that the increase in spontaneous recombination current associated with both the dots and the QW was small compared to the total change in current density measured over the same temperature range.

Despite the intangible nature of these processes, it is possible, from the segmented contact measurements, to estimate what fraction of the threshold current increase is due to thermal spread of carriers. At 240 and 340 K the threshold current density of a 2 mm laser (formed from the tensile strained structure) is 100 and 280 Acm^{-2} respectively. To produce the same inversion at 340 K as that at 240 K requires a current increase of 88 Acm^{-2}. The difference, therefore between this (188 Acm^{-2}) and the threshold current density at 340 K is that associated with the extra current required to compensate for the thermal spread of carriers. It equates to 51 % of the total increase in current density.

The laser structures discussed so far have all shown a monotonic increase in threshold current with temperature. It has been observed in other material systems, for example in InAs QD lasers, that the threshold current can rise and then fall again with increasing temperature [Smowton et al. 2007]. The origin of this behaviour has been attributed to the thermalization of carriers among the spatially separated dot states – an effect which is likely to occur in all inhomogeneously broadened QD systems. The temperature range at which thermalization takes place and the effect it has on the laser characteristics (e.g. threshold current) depends on the nature of the dots; namely their size and whether multimodal distributions exist.

The threshold current characteristics of two nominally identical InP QD structures, except for the growth temperature, were compared between 180 and 350 K. The

samples, grown at 710 and 750°C, had a similar epitaxial structure to previous samples discussed but contained 8 nm barrier regions instead of 16 nm. The temperature dependence of threshold current measured for 2 mm long oxide isolated stripe lasers fabricated from both these structures is shown in Figure 5-13.

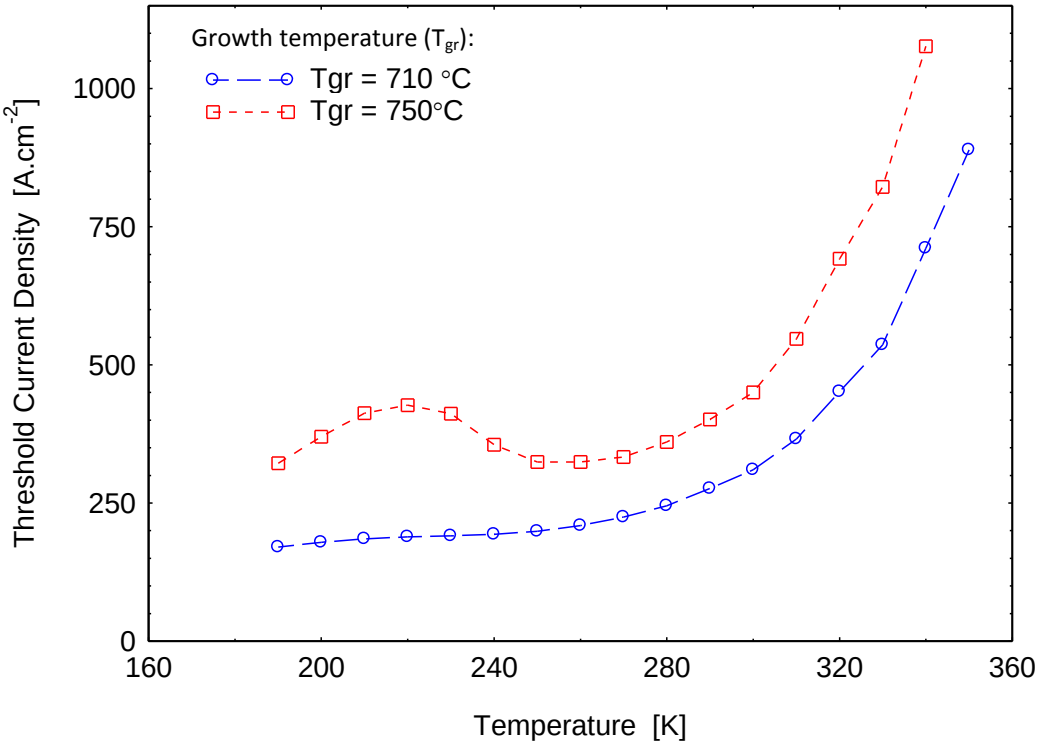

Figure 5-13: Threshold current density vs. operating temperature for 2 mm long lasers grown at a temperature (T_{gr}) of 710 and 750 °C.

The threshold current density of the 8 nm barrier materials is higher than the 16 nm samples grown at equivalent temperatures. For example, in the samples grown at 710°C J_{th} at 300 K is 45 Acm^{-2} higher than measured for the 16 nm barrier sample. An even larger difference of 180 Acm^{-2} is observed between the two samples grown at 750 °C. Although the narrower 8 nm barrier means that a larger number of dot layers can be deposited for the same active layer thickness, it is likely that this width is insufficient to prevent one dot layer from influencing the formation of the next, causing deleterious effects on the performance of the lasers. The internal optical loss appears not to be significantly affected by varying the width of the barrier. It is presumed that the higher threshold currents observed in the 8 nm samples are due to

a change in the density of dot states which contribute to the optical gain of the laser and possibly an increase in the number of defect states present.

The 8 nm barrier sample grown at 750 °C has a notably different temperature dependence to the other sample grown at 710 °C. The threshold current initially increases with temperature until a local maximum is reached at 220 K, and then falls to a minimum at 260 K. At temperatures above this, the threshold current increases super-linearly.

Inspection of the absorption curves for the 8 nm barrier samples, shown in Figure 5-14, reveals that, as well as having the dot states shifted to higher energy, the 750 °C sample has a greater degree of absorption from the higher energy states than the 710 °C sample. The same was also true for the samples containing the 16 nm barrier regions (described in Section 5.3.2). This suggests that the relative fraction of dots in the small dot subset is increased for the samples grown at a higher temperature.

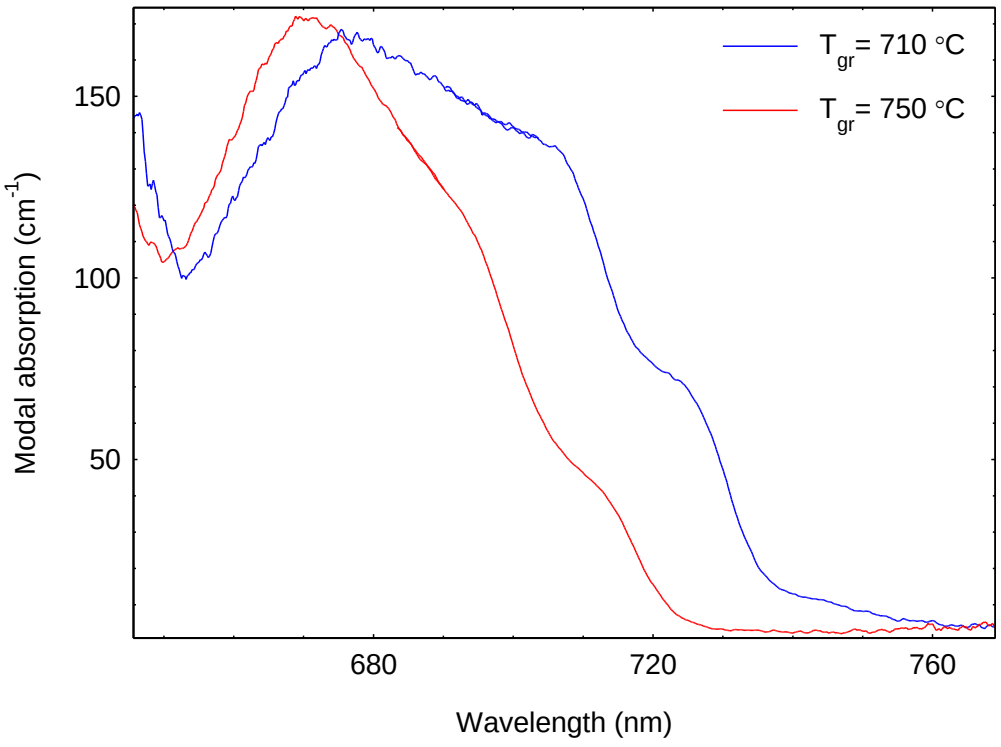

Figure 5-14: Modal loss spectra for 8 nm barrier InP QD samples, grown at a temperature (T_{gr}) of 710 °C (blue) and 750 °C (red).

In an attempt to investigate the possible mechanisms responsible for the non-linear temperature dependence, the injection level for both the 8 nm barrier samples was

measured over the temperature range of interest. As mentioned previously (Chapter 3), for a given set of states contributing to the optical gain, the injection level quantifies how hard the device is being driven. For both samples, the optical gain and absorption spectra in Figure 5-15 was used to obtain the injection level (Figure 5-15) for a constant peak gain of 6 cm^{-1} (2 mm long laser).

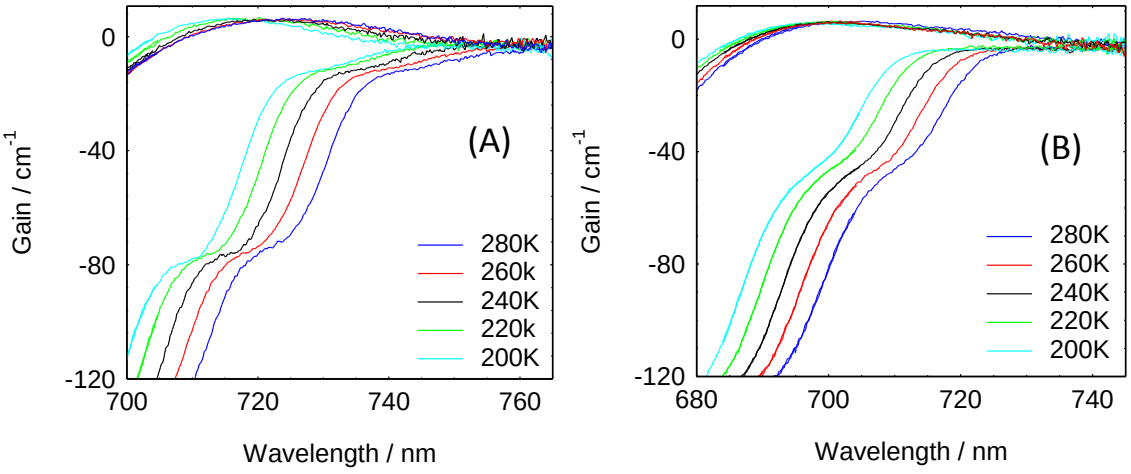

Figure 5-15: Modal gain spectra and absorption (shown here as negative gain) for 8-nm barrier samples grown at 710 (A) and 750 °C (B). Data was used to obtain the injection level required to maintain a fixed net-gain of 6 cm^{-1}.

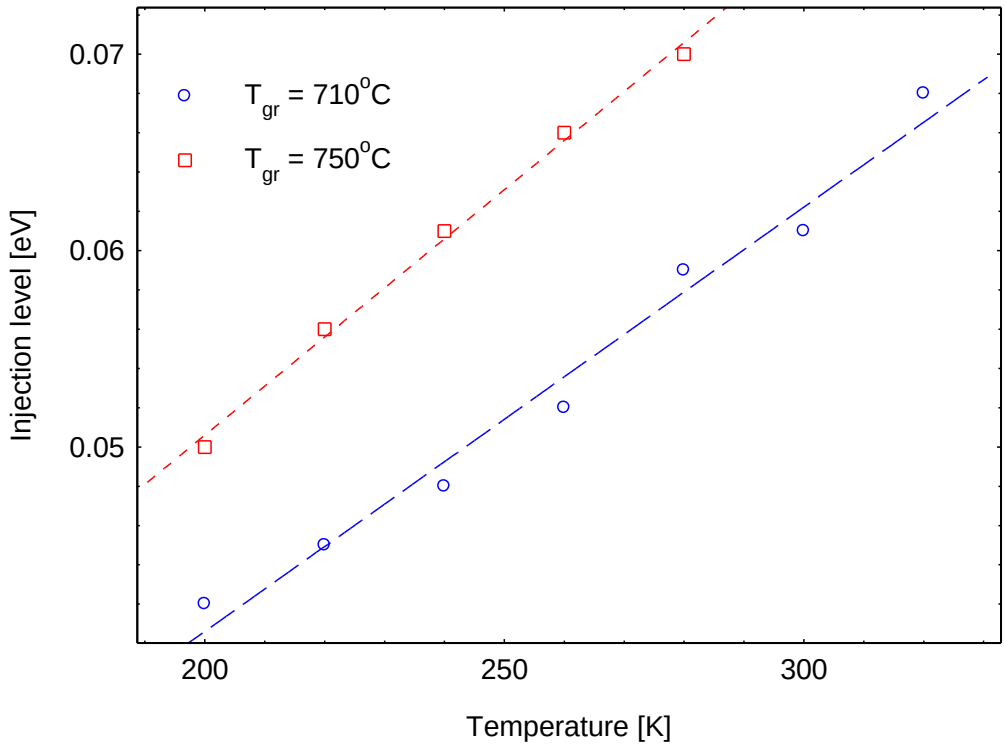

Figure 5-16: Injection level required to reach threshold in a 2 mm long laser (net gain of 6 cm^{-1}) for both 8 nm barrier samples, grown at temperatures of 710 (blue circles) and 750°C (red squares)

Rather surprisingly, the injection level increases monotonically with temperature for both the samples even though the current density required to achieve this gain is distinctly different, following the behaviour of the threshold current density of the laser (Figure 5-17). This behaviour is contrary to that observed in p-doped InAs QDs and suggests the mechanism here may be different, or not related with the energy states associated with the gain spectra.

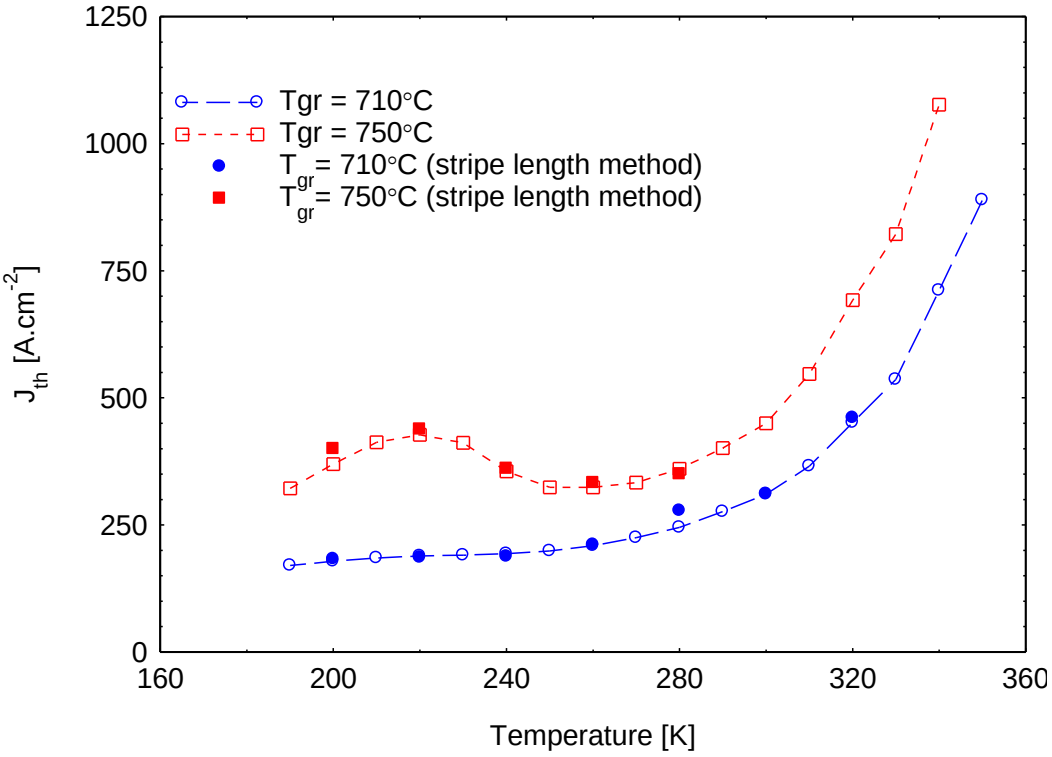

Figure 5-17: Comparing the current required to reach the level of injection given in Figure 5-16 using the stripe-length method, with the threshold current measured for the laser devices.

The internal optical loss for both samples was measured to be the same (within experimental error) over all temperatures and is therefore not the cause for variation in the threshold currents. A likely cause of the higher threshold current in the sample grown at 750 °C is a result of the lower density of dots within the large subset. As with the sample grown at 710 °C, the initial rise in the threshold current of this sample is a result of the thermal spread of carriers among the large dot subset and, as discussed previously, an increase in non-radiative recombination processes. However, as the temperature increases further (220 - 260 K) the electrons that have been captured into the small dots obtain sufficient thermal energy to redistribute among the spatially separated large dot states. The effect of this being that the threshold current necessary to reach the required level of gain begins to fall. The increase in temperature has “tapped” into the reservoir of electrons that were captured into the small dot states – states that are not contributing to optical transitions usable for laser action.

Measurements of the spontaneous emission as a function of temperature, courtesy of Muhammad Al-Ghamdi (Cardiff university), were used here to find further evidence for this non-thermal to thermal transition. For clarity, the spontaneous emission spectra were normalised and the shift in band-gap with temperature was factored out by measuring the shift of the absorption edge. These spectra are plotted in Figure 5-18 and Figure 5-19 for the samples grown at 710 and 750 °C respectively.

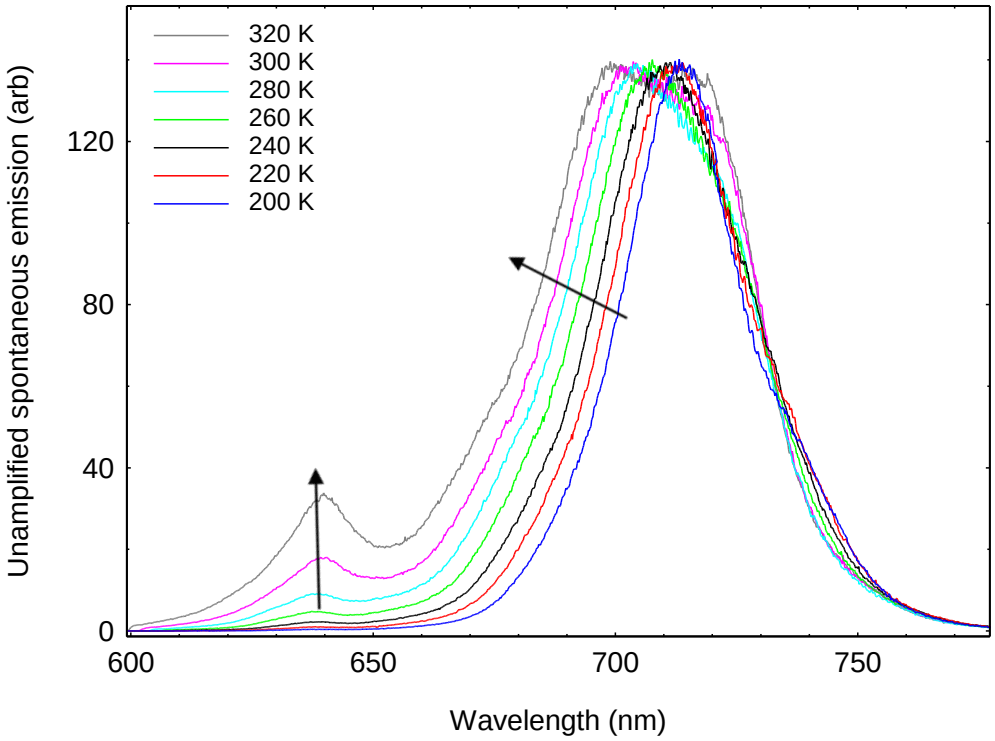

Figure 5-18: Unamplified spontaneous emission spectra for sample grown at 710°C; arrows show the increasing amplitude of QW emission with increasing temperature and broadening due to thermal spread of carriers amongst dot states. Data courtesy of Muhammad Al-Ghamdi (Cardiff University)

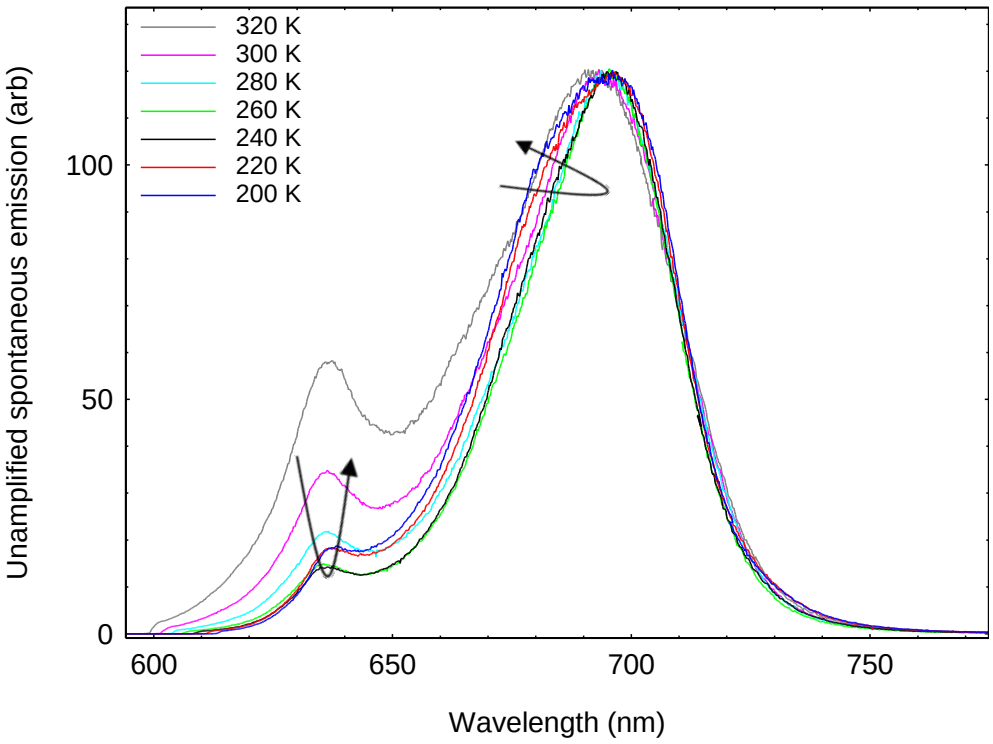

Figure 5-19: Unamplified spontaneous emission spectra for sample grown at 750°C; arrows showing change in amplitude of QW emission with increasing temperature and broadening of due to thermal spread of carriers from dot states. Data courtesy of Muhammad Al-Ghamdi (Cardiff University)

The profile of the spontaneous emission spectra corresponds to the distribution of charge carriers among the available energy states. The first (larger) peak is due to the inhomogeneously broadened QD states and the second peak is due to emission from the GaInP QWs. The distribution due to the QD states increases linearly with temperature in the sample grown at 710^{o}C, with increased population of higher energy states and thermal activation into the QWs. The emission spectrum of the 750 °C sample evolves with temperature in a way which is characterised by the directed line shown in Figure 5-19. The breadth of the profile in this region of energy follows the behaviour of the threshold current density of the laser, with a minima occurring at 260 K. The plot also reveals that this effect is coincident with the variation in amplitude of the QW; however, this is only a consequence of the reduction in threshold drive current. It is therefore likely, that a thermally activated redistribution of carriers from the small dot subset is responsible for the reduction in short wavelength emission observed in the spontaneous emission spectra and hence the decrease in threshold current between 220 and 260K.

The spectral region of the spontaneous emission over which optical gain is achieved does not appear to show any observable effect of a thermal to non-thermal transition and hence why the injection level varied monotonically in both samples and did not follow the threshold current dependence.

It appears to be the nature of the dot size distribution, due to the effect of growth temperature, which dictates whether, or at what temperature, we observe the effects of the thermal to non-thermal distribution of charge carriers between the two dot ensembles.

5.6. Temperature Dependence of the Gain Peak Wavelength

It is likely that the temperature of a laser device will vary under operation, either by internal self-heating, or by external mechanisms such as the temperature of the surrounding environment. The temperature of the laser will of course depend on the intended application and since a given laser structure may be used in a number of different applications, it is useful to quantify the temperature dependent behaviour, namely the threshold current (described in Section 5.5) and the operating wavelength. The mechanisms that govern these two characteristics are both related to the way carriers are distributed amongst the available states with changes in temperature and injection level.

Stability of the gain-peak wavelength is important parameter to consider in this project, as it will directly influence the operation of a dual-wavelength source. The work presented in this section characterises how the gain-peak wavelength is affect by changes in temperature and injection level (via the effects of state filling) for the tensile strained sample described in Section 5.4. In edge-emitting lasers, the wavelength is governed by how the gain-peak (G_{pk}) position varies with temperature and for lasers where the feedback is spectrally dependent, such as in VCSELs or DFBs, any variation of the G_{pk} with respect to the Bragg frequency will cause a variation in the threshold current. In an idealized QD array, where the states are represented by delta functions, the G_{pk} is expected to vary with the band-gap temperature coefficient, irrespective of the level of gain. Previous work has shown that for a fixed level of gain,

the temperature dependence of the G_{pk} wavelength in InGaAs QD laser structures does not always follow that of the band-gap [Thomson et al. 2001].

The energy distribution of the dot states is inhomogeneously broadened due to the statistical fluctuation in dot size. Consequently, the wavelength at a given temperature is strongly dependent of state-filling, in that an increased level of injection will cause a blue-shift of the G_{pk}. The effect of this is apparent in Figure 5-20, where the optical gain spectra at 300 K are shown for various levels of injection. Since the peak net-gain relates to a certain cavity length (edge-emitting lasers), the effect of state-filling is that lasers of different cavity lengths will emit at different wavelengths. This effect can be used to generate dual-λ emission and a method to achieve this is described in Chapter 6. Incidentally, in QW lasers, the shift in G_{pk} wavelength with injection is much less and therefore they are not as suitable for accessing widely separated wavelengths using this approach.

To characterise the temperature dependence of the G_{pk} wavelength for InP QD lasers, at different G_{pk} magnitudes, the optical gain was measured at various levels of injection for a range temperatures.

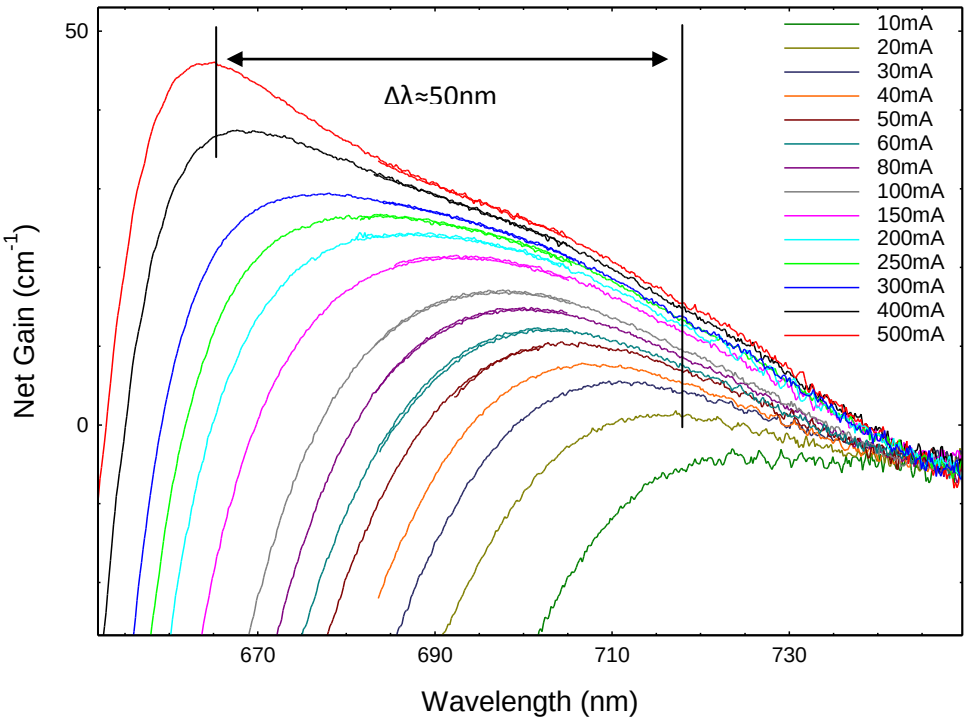

Figure 5-20: Measured Net modal gain spectra, for increasing current injection at 300K using the stripe-length method.

The G_{pk} magnitude versus spectral position is shown in Figure 5-21, for a temperature range of 240 – 340 K.

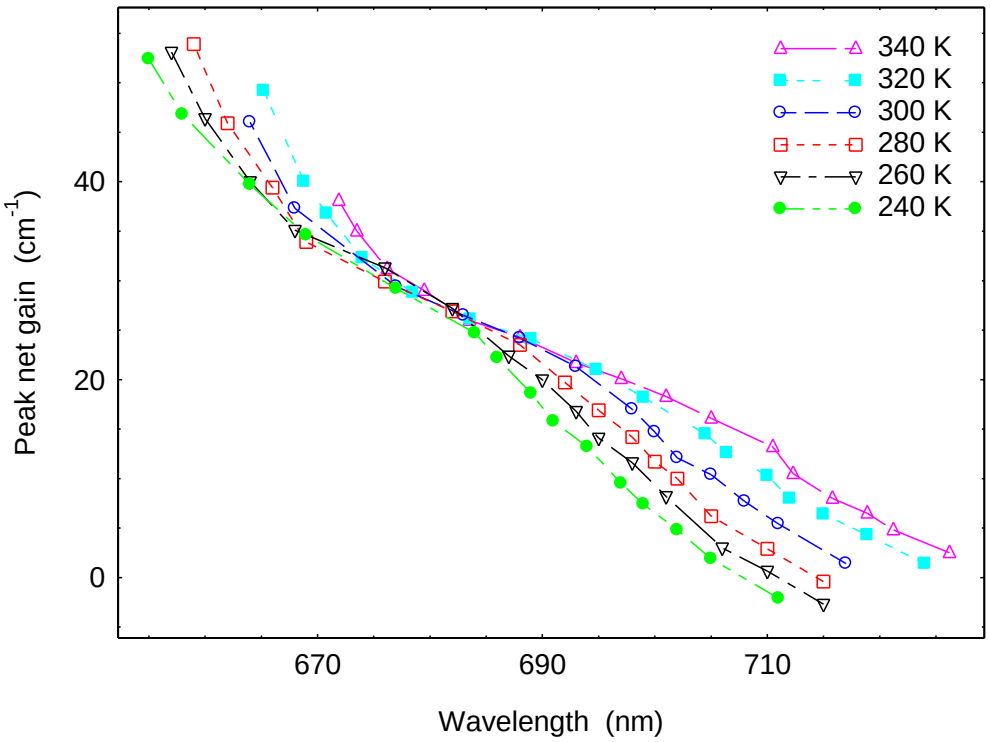

Figure 5-21: Plot shows relationship between the peak net-gain and its spectral position.

It is immediately obvious from the data plot that the variation of the G_{pk} wavelength with temperature depends on the magnitude of the gain (level of injection). Perhaps more striking, is that for gain values in the region of 25 – 30 cm^{-1} there is little change in the G_{pk} wavelength with temperature. To illustrate this more clearly, the plot in Figure 5-22 shows the change in wavelength with temperature as a function of the peak net-gain *(G-α_i).*

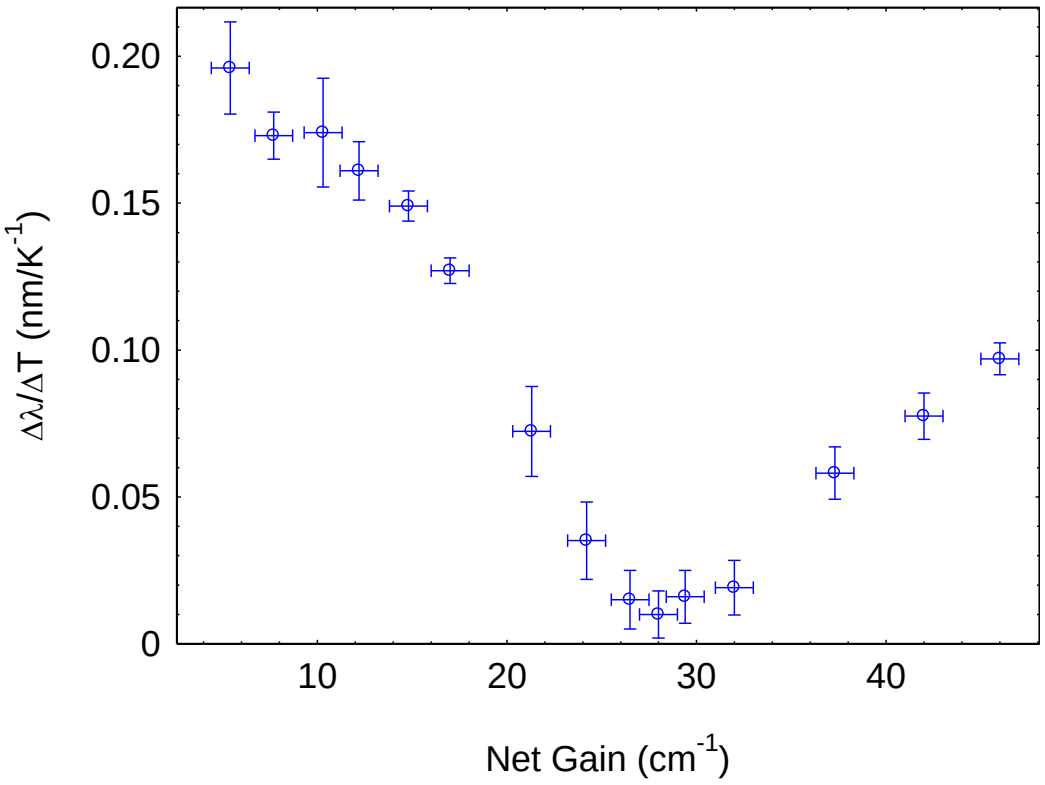

Figure 5-22: Data obtained from the gain measurements, showing the change in peak wavelength with temperature as a function of Gpk magnitude.

For a fixed gain at low injection the wavelength dependence of the G_{pk} follows that of the band gap (≈ 0.17 nm/K), as described by the Varshsni equation, but at higher levels of injection the wavelength becomes relatively independent of operating temperature, until the gain increases beyond 30 cm^{-1}. A similar effect has been observed in GaInAs/(Al)GaAs laser structures [Klopf, F. et al. 2002], where the most temperature insensitive behaviour was observed in a laser with a single layer of dots and weak optical confinement (relative to the comparator structures). They reported on a rise in α_i with increasing temperature and inferred that an increase in gain was required in order to equate with the loss of the cavity as temperature increased. This effect was not observed in this study; within experimental error, α_i remained constant over the temperature range investigated.

The temperature dependence of the G_{pk} wavelength is attributed to both the evolving distribution of carriers among the energy states and the rigid shift due to the band-gap temperature coefficient. As the level of carrier injection increases, the temperature dependence of these two effects begin to compensate each other and this onset is

characterised by a broadening of the gain spectra (discussed below), an effect which coincides with the reducing temperature sensitivity of the G_{pk} wavelength.

In order to maintain a fixed net gain as the temperature increases, there must be an increase in the level of injection. The effect of this is illustrated in Figure 5-23. The blue and red solid lines are the measured gain spectra for a fixed level of injection at 240 and 300 K respectively. The dashed red line is the measured spectrum at 300 K which results from the necessary increase in injection required to maintain a fixed gain. The resulting blue-shift observed due to state-filling, is equal to the red-shift in the band-gap with temperature (which has been quantified by the change in half height position of the absorption edge), and hence there is no change in the peak wavelength.

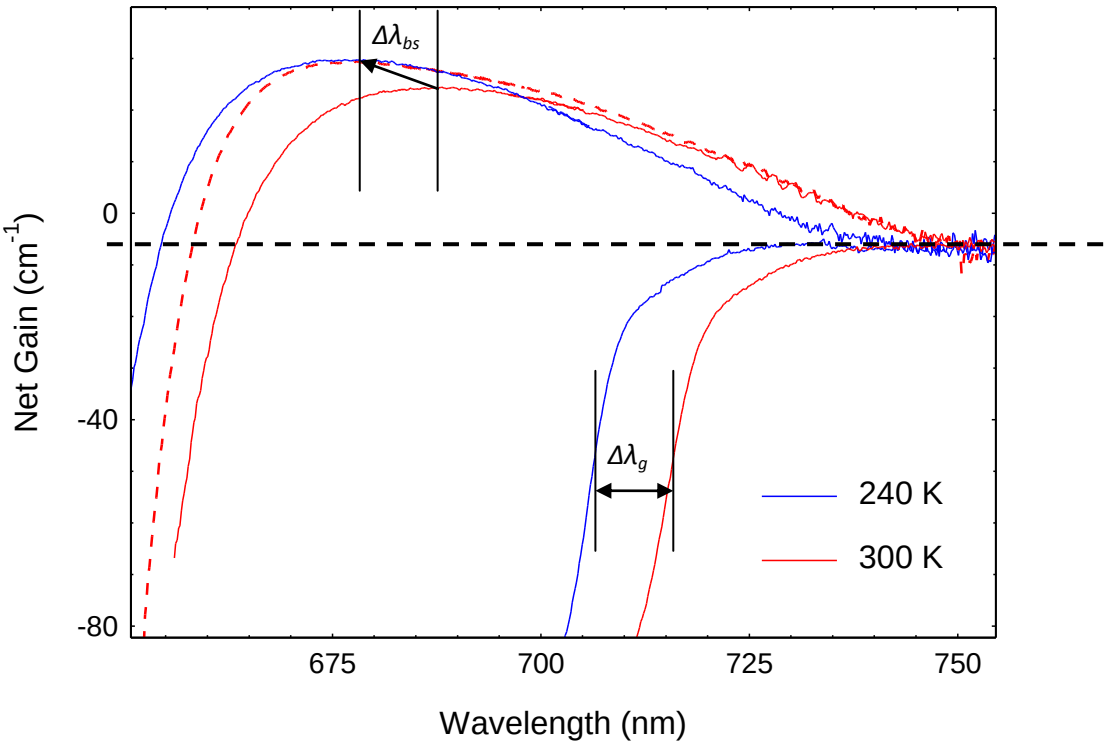

Figure 5-23: Illustrates the net modal gain and absorption spectra for a fixed level of injection (red and blue solid lines) and how the spectrum evolves (dashed line) when the injection level is increased to maintain a fixed Gpk. The red-shift due to the temperature coefficient of the band-gap (Δλg) is compensated by the blue-shift ($\Delta\lambda_{bs}$) of the peak due to state filling.

The gain-current relations for a temperature range of 240 – 340 K are shown in Figure 5-24. For low carrier injections, the gain is dominated by ground state transitions of the large dot subset, but as the injection is increased further, there is a distinct change in the gain-current dependence. This is brought about by a significant contribution

from transitions belonging to a quantised distribution with a higher density of states, which is likely to be from the ES and or the GS, of the large and small dot subset respectively. These two regions are both fitted with the empirical relation given by Equation 5-1.

The relation provides a good fit at both the linear regime at low injection and the saturation region of the gain curves. The ideality factor (Υ value), which quantifies the variation of the gain-current relation from an ideal QD ensemble, should be closer to unity if the contribution from higher lying states is small. This correlates with the experimental data, in that the Υ value is lower in the regime where the gain is dominated by transitions from higher energy states, which are in closer proximity with the QW states.

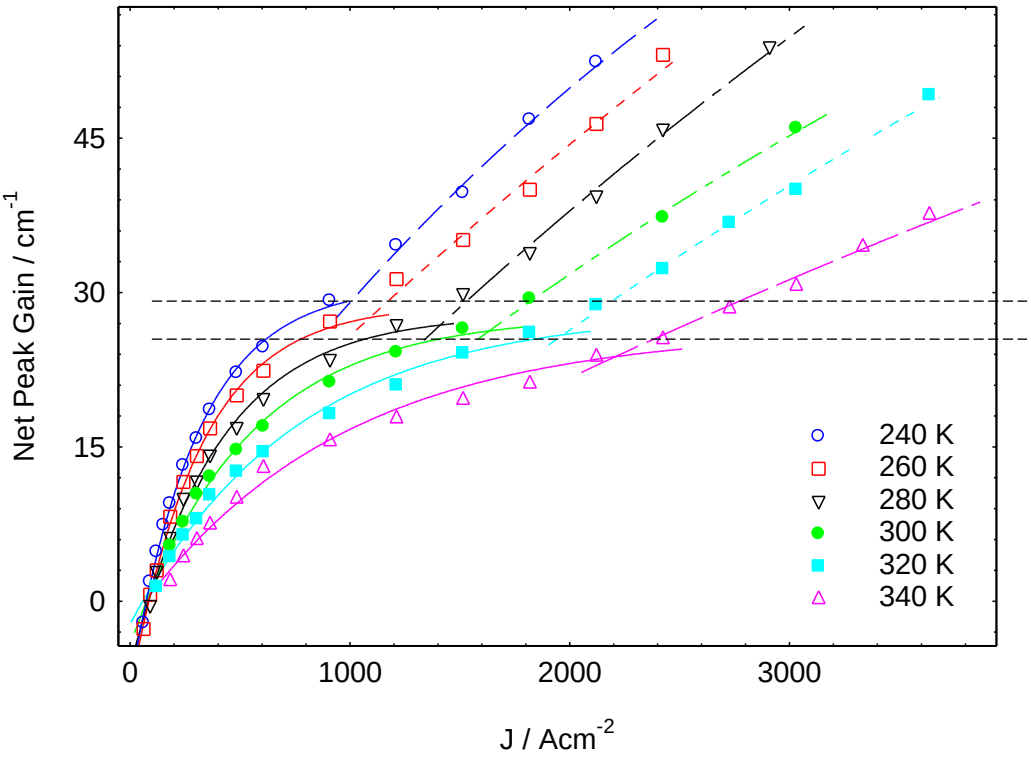

Figure 5-24: Gain-current relations for InP QD samples measured at various temperatures. There are two distinct regions for each data plot which have been fitted separately using Equation 5-1. The region bound by the dashed line indicates the range of gain where Δλ/ΔT falls to a minimum.

A higher gain requirement means that the level of inversion must be increased by injecting more carriers. However, the gain will begin to saturate prematurely compared with an idealised QD array, because carriers begin to populate higher lying

states which do not necessarily contribute to the peak gain. In this ensemble of dots, there is a wide distribution of electronic states and therefore as the level of injection increases, the gain spectrum begins to broaden as the G_{pk} magnitude saturates

To explain this effect in terms of how the dot states are populated, it is necessary to consider the overlapping distribution of energies associated with the QD ensemble. For simplicity, suppose that the bi-modial distribution of energy states comprises of two overlapping Gaussian (G1 and G2) associated with the two distinct regions of the gain-current curves. The situation is illustrated by a schema (Figure 5-25), where the summation of the two Gaussians results in the purple dashed line.

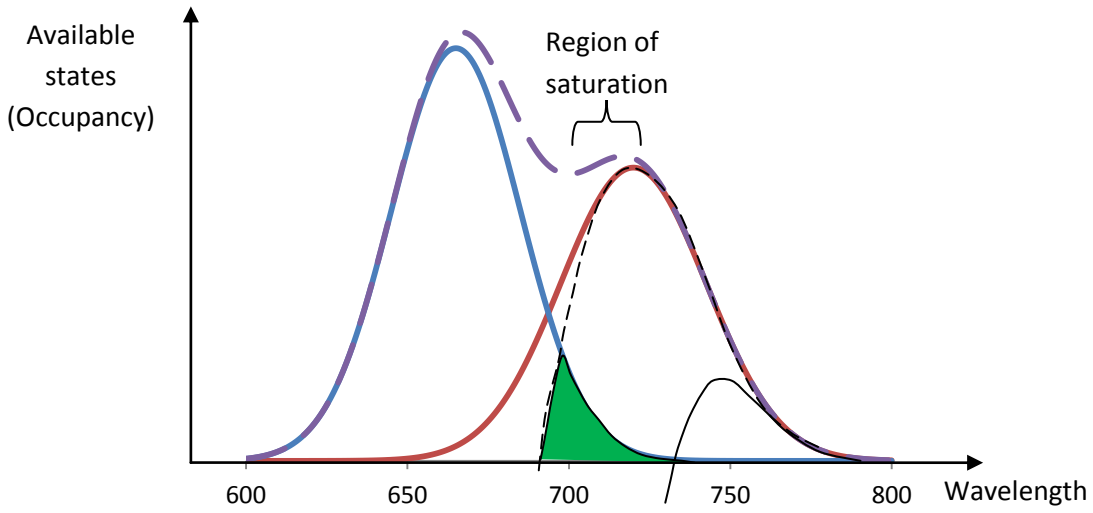

Figure 5-25: Diagram to show state filling of an energy distribution comprising of two Gaussians arising from the inhomogeneous distribution of dot states.

The black solid line under the long wavelength tail exemplifies how the states of the system begin to populate as carriers are injected. When the level of injection increases beyond the peak of G1 (black solid curve), the optical gain begins to saturate. As this occurs carriers begin to occupy the states of the G2, and this is represented by the green shaded region located within its tail. The injected carriers now have a larger reservoir of electronic states to fill, however below a certain level of occupancy, the optical transitions associated with the higher energy states do not contribute to the peak of the gain and instead have the effect of broadening the gain spectrum.

The effect of this is illustrated in Figure 5-26, where the relative breadth of the gain spectrum is represented by the difference between transparency and the G_{pk} position (λ_{pk} – TP). The spectrum broadens with progressive pumping, until the G_{pk} magnitude becomes dominated by transitions of the higher lying states. As pumping proceeds further the spectral width begins to reduce and the point at which this "roll-off" occurs corresponds to the region of gain where the empirically fitted gain-current functions in Figure 5-24 cross over.

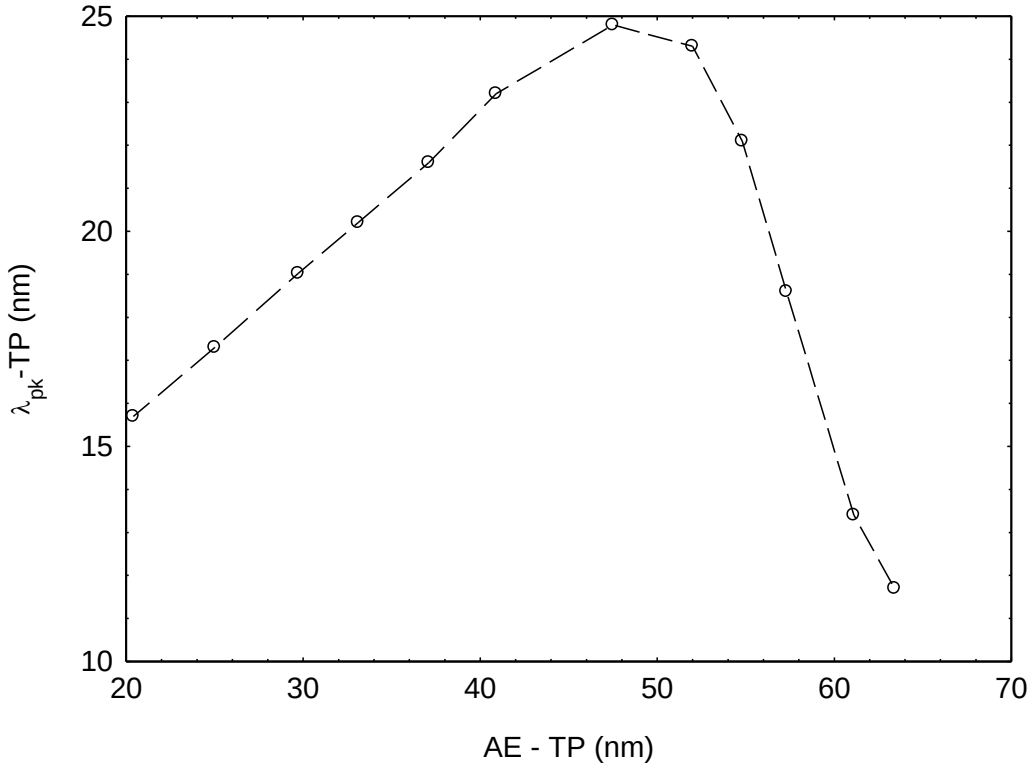

Figure 5-26: Illustrates the broadening of the gain spectra as the level of injection increases. Data extracted from 300 K gain spectra, where the breadth is characterised by the difference between TP and the G_{pk} wavelength (λ_{pk} – TP).

During the transition between these two distributions of states, the rate of change of the G_{pk} wavelength with increasing gain reaches its maximum, or put another way, the magnitude of the gain due to ground state transitions begins to saturate, but the wavelength of the peak continues to blue-shift with state filling. This effect is evident from the family of curves plotted in Figure 5-21, where there is a point of inflection corresponding to the ground-state saturation seen in the gain-current curves. This mechanism results in a large enough blue-shift to balance the temperature dependence of the band-gap. At still higher pumping, the largest gain is no longer

obtained from the ground state and the larger number of excited states allows a more rapid increase in gain magnitude. In addition, the population of a high density of states decreases the change in quasi-Fermi level with increasing carrier injection and results in a relatively smaller change in the peak wavelength. This reduces the compensation of the bandgap-controlled wavelength shift and therefore results in larger value of $\Delta\lambda/\Delta T$.

5.6.1. Laser Measurements

Establishing the temperature dependence of the G_{pk} wavelength has revealed an interesting behaviour, which results from the inhomogeneity of the QD ensemble and the wide distribution of dot states. Through understanding the regime that gives rise to a relatively temperature-insensitive G_{pk} wavelength it is, in principle, possible to design edge-emitting lasers that also have a temperature-insensitive operating wavelength. As described in Chapter 2 (Section 2.4), the net modal gain (G-α_i) is proportional to the inverse cavity length. Therefore, by appropriate choice of length, a laser that has a relatively temperature-insensitive wavelength can be fabricated.

The peak wavelength of edge emitting lasers from 280 – 380 K are shown in Figure 5-27 and the corresponding emission spectra for these devices at 300 and 380 K are shown in Figure 5-28. For a cavity length of 3 mm (G-α_i = 4 cm^{-1}) the temperature dependence is nominally the same as the band-gap at 0.17 nm/K, but this has been lowered to 0.03 nm/K using a 0.4 mm cavity (G-α_i = 30 cm^{-1}). This shorter cavity length is more ideally suited for incorporating into compact devices, or for accessing short wavelengths, due to the high level of state filling.

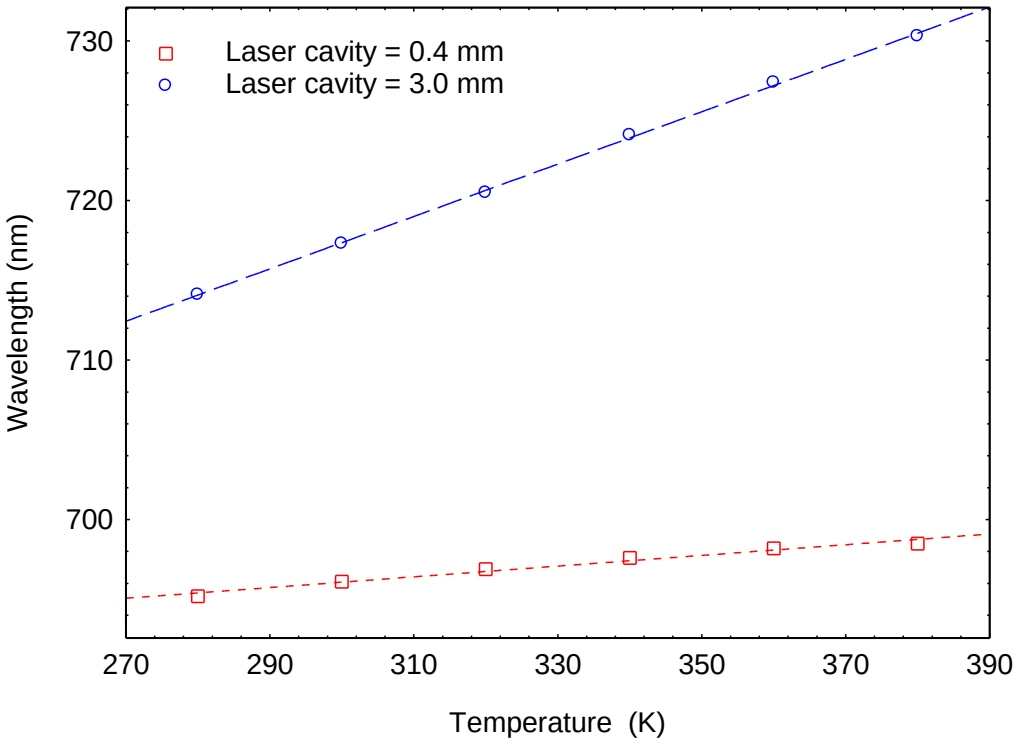

Figure 5-27: Emission wavelength of edge-emitting lasers from 280 to 380 K. Shown here is a laser with a 3 mm long cavity (circles) with $\Delta\lambda/\Delta T \approx 0.17$ nm/K and a 0.4 mm long cavity with $\Delta\lambda/\Delta T \approx 0.03$ nm/K

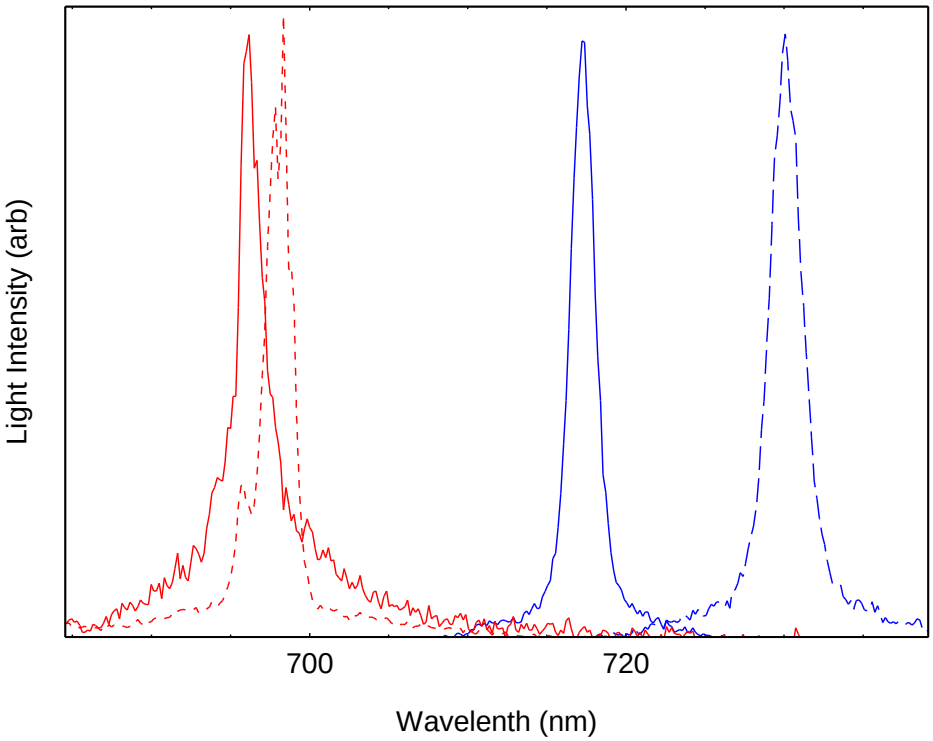

Figure 5-28 Emission Spectra at 300 K (solid lines) and 380 K (dashed lines), for 3 mm (blue) and 0.4 mm (red) length lasers.

The only compromise to be made here is that the shorter the device, the higher the current density that is required to reach threshold. Neglecting the issues concerning heat extraction for the moment, a high current density is not necessarily detrimental, since it is the total current which determines the power consumption. The relationship of total drive current to device size (cavity length) is given by:

$$I_d = wJ_{tot}L_c = wJ_{tot}\left[\frac{1}{G_{th} - \alpha_i} ln\left(\frac{1}{R}\right)\right]$$

Equation 5-2

where w is the lateral current spreading and J_{tot} is the total current density. Hence, by extracting information from the gain-current characteristic a plot of cavity length versus threshold current can be constructed. This is shown in Figure 5-29 for data obtained in a temperature range of 240 – 340 K. The threshold current initially falls as the length of the cavity is reduced, but then begins to rise rapidly with further reduction. Ideally, the minimum in drive current would correlate with the length of laser which achieves the least temperature dependent wavelength. However, for this epitaxial design this is not the case: the minimum threshold current corresponds to a cavity which is between 800 and 1200 µm giving at best 0.13 nm/K dependence. Therefore, the penalty to pay for a temperature-insensitive wavelength is a relatively high threshold current.

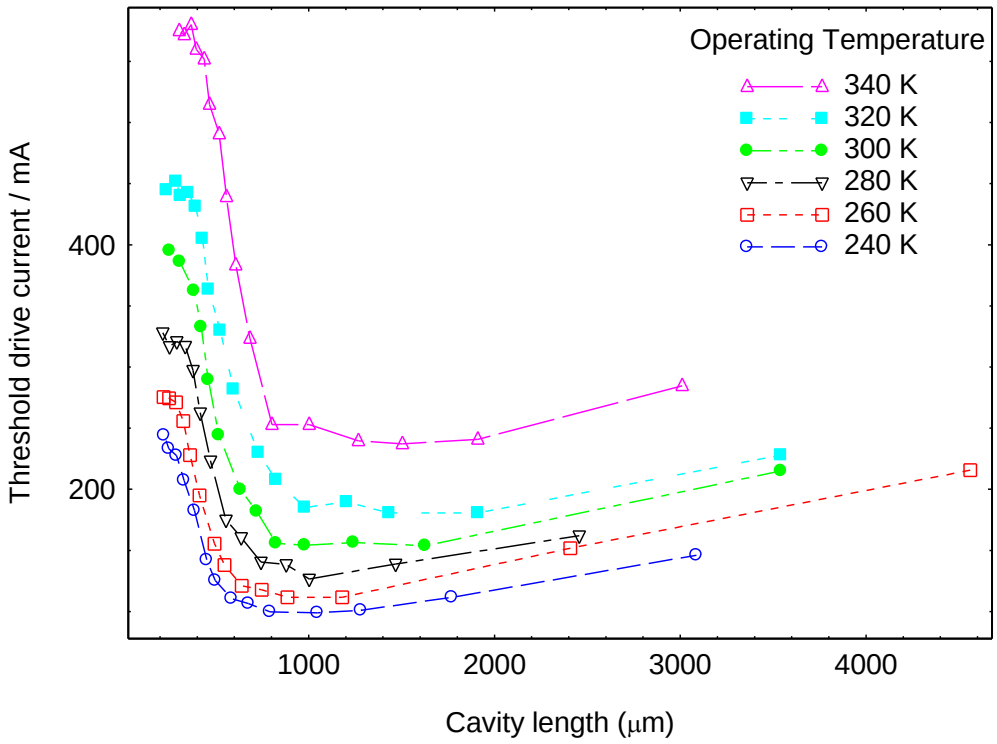

Figure 5-29: Data extracted from gain-current relations obtained from multi-section experiment showing how the threshold drive current relates to laser cavity length.

While the results reported here are specific to a type of InP QD laser structure, similar results are expected for all types of QD materials, albeit at a different level of pumping, because the origin of the effect is manifested in the way carriers fill the inhomogenously broadened QD states. It is anticipated that altering the number of layers in the gain medium or the dot density in each subset will influence the value of gain at which $\Delta\lambda/\Delta T$ falls to a minimum. However, since saturation of the ground state gain is necessary to create a large enough blue-shift with increasing gain magnitude, it is not possible to optimise the active structure so that wavelength-insensitivity corresponds to a minimum in the drive current.

5.7. Summary

In this chapter, the optical properties of various InP/AlGaInP QD laser structures have been investigated with the motivation to establish a suitable structure for a dual-wavelength device. The stability and range of wavelengths that can be accessed, as well as the threshold current dependences, are all important factors to consider when

designing a dual wavelength device. Understanding the mechanisms that govern these effects was the main goal of this chapter.

The effect growth temperature (T_{gr}) has on the performance of laser devices in terms of threshold current has been investigated. The samples tested in this project were grown at 710, 730 and 750° C. The threshold current over the temperature range investigated was found to reduce with decreasing $T_{gr.}$ Measurements of optical absorption revealed that the dot states shift to high energy with increasing T_{gr}, with a reduction in dot density associated with the large dot subset. Modal gain measurements revealed that the increase in gain with current was lowest for the sample grown at 750 °C. The modal gain at each value of current was very similar in the other two samples (710, 730 °C) and any variation in threshold current was ascribed to the difference in α_i.

Measurements of threshold current density revealed that reducing the barrier width from 8 to 16 nm had deleterious effects on the laser performance. This was attributed to the influence that dot layers can have on the formation of dots in the subsequent layer when barrier widths are too thin. In all laser devices, the threshold current increased monotonically with temperature, over the measured range, except in the 8 nm barrier sample grown at 750 °C. The rise and fall in threshold current between 200 and 260 K was attributed to a change in the thermal distribution of carriers between the small and large dot subset. This section also dealt with the mechanisms responsible for the super-linear increase in threshold current commonly associated with real QD ensembles. The current required to compensate for the thermal spread of carriers amongst the available dot states was identified as the main culprit and this effect is exacerbated by any increase in the inhomogeneous broadening. Although a temperature insensitive threshold current is unlikely to be achieved, the incorporation of strain into the upper confining layers (in an attempt to reduce the asymmetry between the conduction and valence bands) gave promising results, especially for the shortest (1mm) devices tested. This sample was therefore seen most attractive for use in dual-wavelength devices that require short cavities. In addition, it was revealed how strain together with growth temperature can further extend the accessible range of lasing wavelengths.

Finally, the chapter described the effect state filling has on the G_{pk} wavelength and how it is affected by changes in operating temperature for the strained sample grown at 730 °C. This proved to be an important characteristic to investigate, as it not only provides information on how state-filling can be using to vary the emission wavelength, it also reveals how the stability of a dual-wavelength device may be affected by temperature changes. At low injection, the temperature dependence followed that of the band-gap (≈ 0.17 nm/K) but at higher levels of injection, the wavelength became relatively insensitive to temperature. A 0.4 mm long laser was demonstrated with a temperature dependence as low as 0.03 nm/K. However, the compromise to be made here is the relatively high threshold current. The mechanism responsible for gain dependent wavelength sensitivity to temperature is a property of inhomogenously broadened dots and therefore a regime of insensitivity is expected to occur in other dot structures. The analysis presented here is a useful tool in determining the level of pumping at which this effect occurs. Wavelength stability is important for a number of laser applications and where the ability to control temperature is limited, the implications of a material offering a temperature insensitive operating wavelength becomes very important.

As stated in the introduction to this chapter, the principle interest in measuring the optical properties of this series of epitaxial wafers was to establish a structure most suitable for a dual-wavelength laser. However, the understanding of the material system and the effect structure changes have on basic laser performance, such as threshold current densities and wavelength stability, can be used to further-improve such device performance.

Chapter 6. Monolithic dual-wavelength InP QD lasers

6.1. Introduction.

The developments made in preceding chapters culminate in the design, fabrication and characterisation of the devices investigated in this chapter. The main goal of this work is to establish a dual-wavelength (dual-λ) monolithic laser device that could potentially be used in a range of applications: from a compact terahertz source, to biomedical applications such as optical coherence tomography (OCT) and excitation of fluorescent dyes. The first section of the chapter discusses how the operating wavelength can be governed by incorporating grating structures such as Distributed Bragg Reflectors (DBR)s. The following section tackles the principle of achieving dual-λ operation, by virtue of the material properties, using coupled cavity ridge lasers. Finally, the two strands of the chapter are brought together to describe a novel design for a monolithic dual-λ laser: a coupled cavity RWG which incorporates gratings to provide preferential feedback at the desired wavelengths.

6.2. Varying the emission wavelength using DBRs

As described in the previous chapter, the Stranski-Krastanov growth of this material results in an inhomogeneous distribution of dot sizes giving rise to a wide distribution of electronic states. This provides a relatively broad gain spectrum, extending the tuneable range of the emission for lasers which incorporate DBRs. To emphasize the extent of the broad-spectrum characteristic of QDs a comparison was made with a QW sample. This is illustrated in Figure 6-1, where the gain spectra for a red emitting AlGaInP QW and an InP/AlGaInP dot sample [Smowton et al. 2011] are plotted together for a range of injection currents. Apart from the broader gain spectra, the QD sample exhibits a higher peak-gain for a given current and has a lower internal loss of 2 cm^{-1} compared with 9 cm^{-1} for the QW sample.

The ability to source multiple wavelengths from the same active material and vary the emission wavelength are important characteristics, especially the latter as it allows

each laser wavelength to be matched to the given application; for instance the absorption peak of a fluorescent dye or photosensitizer. This particularly benefits, for example, the cyanine squarate dyes which exhibit a narrow absorption bandwidth [Hamilton et al. 1997], [Oswald et al. 2000].

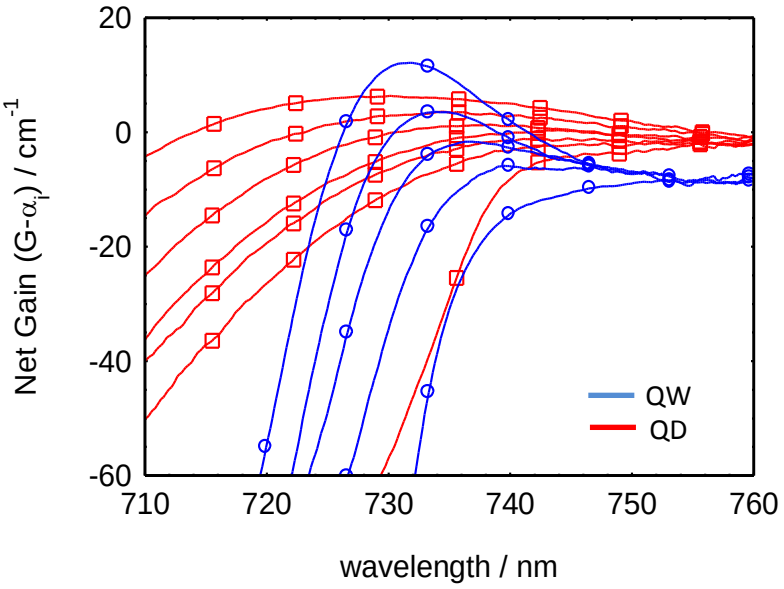

Figure 6-1: Gain and loss spectra (shown here as negative gain) for a current range of 6-30 mA for a QD material (squares) and a current range of 50-125 mA for the comparator QW sample (circles) of the same dimensions. The wavelength of the QW data has been shifted by 75 nm for comparison.

6.2.1. Design and Fabrication

Calculations were based on one dimensional 3rd and 5th order quarter wave stacks with the assumption that the layers are homogeneous and isotropic with semi-infinite extent in the other dimensions. Using the gain spectra, the dimensions of gratings used to form the DBR structures were calculated. To ensure an appropriate overlap with the gain spectrum, but with a mismatch between the maximum reflectivity and the gain peak, a Transfer Matrix Model (TMM), described in Chapter 2, was used to estimate the resulting reflectivity spectrum. The principle is illustrated in Figure 6-2, where the maximum feedback is purposely shifted from the gain-peak to promote laser emission at shorter wavelengths. RWGs were fabricated with a DBR at one end and a cleaved facet at the other, from which the light output was measured.

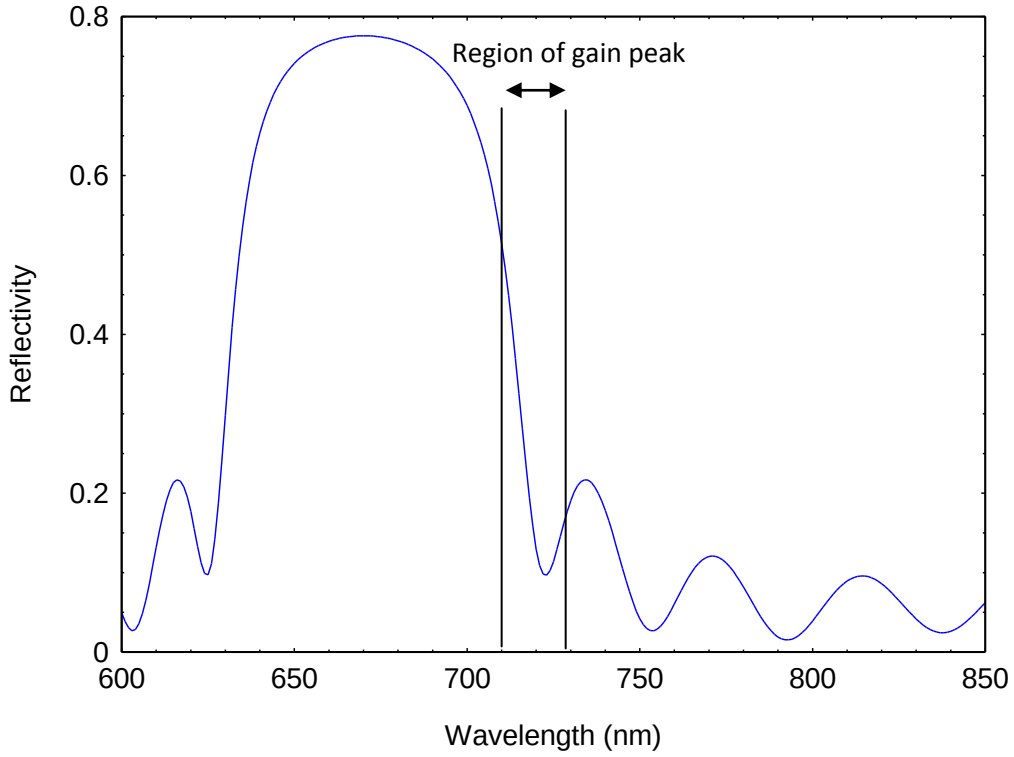

Figure 6-2: Reflectivity spectra based on a 5th order grating structure, showing the region occupied by the peak gain for typical injection currents.

6.2.2. Device Measurements

The lasing wavelengths of a 1.5 mm long ridge with and without a DBR were measured as a function of operating temperature from 220 to 320 K, as shown in Figure 6-3. The emission of the DBR laser (squares) has been shifted to shorter wavelengths (blue-shifted) relative to the ridge laser (circles), as a consequence of positioning the reflectivity stop-band of the grating away from the peak-gain. Over this temperature range, the ridge laser has a shift in emission wavelength of 0.15 nm/K, showing agreement with the Varshni equation (fitted dashed line). The DBR laser shows an improvement to this, with a shift in emission wavelength of 0.07 nm/K. The operating wavelength of the ridge laser follows the temperature dependence of the gain-peak, which is governed predominately by the temperature coefficient of the band-gap. In the case of the DBR laser, the wavelength is also governed by the reflectivity spectrum. Any shift in the reflectivity spectrum is dictated by the temperature dependence of the refractive indices associated with the layers that form the grating. This is generally

known to be less than the change in the energy band-gap with temperature and hence why a deviation from the Varshni equation is observed for the DBR laser.

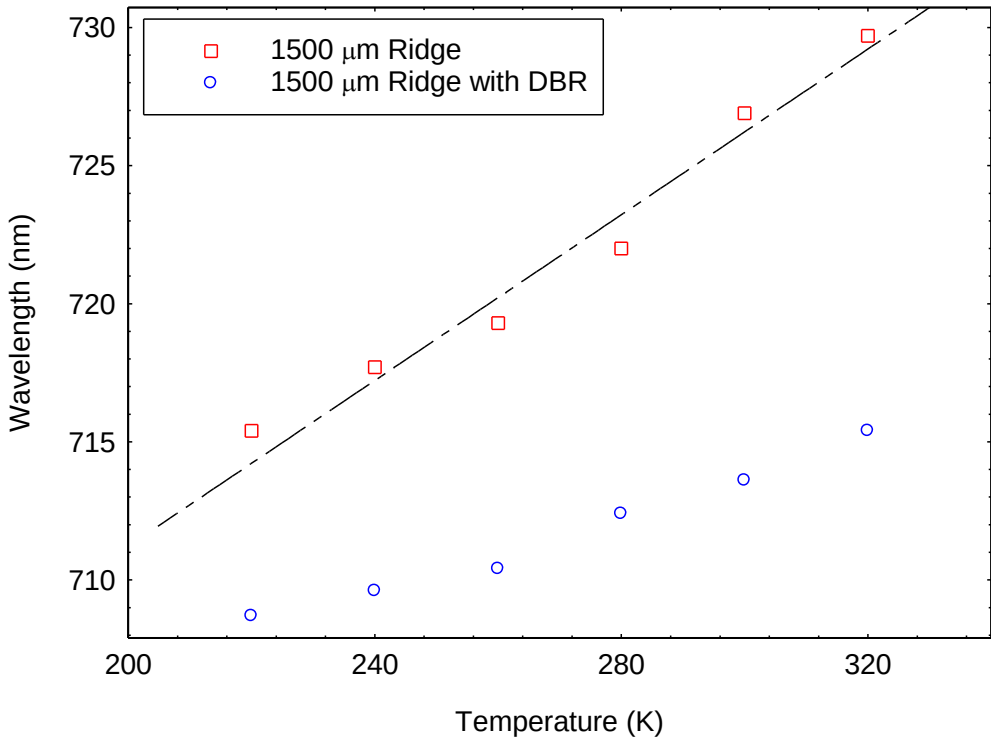

Figure 6-3: Temperature dependence of lasing wavelength for 1.5 mm long ridge (squares) and 1.5 mm long DBR (circles) laser. Dashed line fitted to ridge laser data is the temperature dependence of the band gap calculated with the Varshni equation.

The threshold current density of both lasers are the same at 300 K (within experimental error), therefore assuming the non-radiative contributions are equal, the position of the gain-peak will be the same. The optical gain spectra and the emission wavelength of both laser devices when operating at 300 K are shown in Figure 6-4. The results confirm that the emission wavelength of the ridge laser coincides with the gain-peak position and illustrates how the operating wavelength of the DBR laser has been shifted to a shorter wavelength, closer to the maximum reflectivity of the grating. It is also worth pointing out that there is evidence of multi-modal behaviour in the laser spectra shown in Figure 6-4, especially for the laser without a DBR. This is essentially due to the RWG supporting several lateral modes and this characteristic is explained in more detail in Section 6.4.4.

Above 300 K the threshold current density of the DBR laser begins to increase relative to the ridge laser and this is ascribed to the increasing separation of the gain spectrum

relative to the Bragg frequency with temperature. By estimating the level of gain at which the DBR laser reaches threshold, an approximate value for the reflectivity of the Bragg mirror can be calculated. Using the equation for the round trip gain condition the reflectivity, R_g was found to be ≈ 0.6 at the emission wavelength.

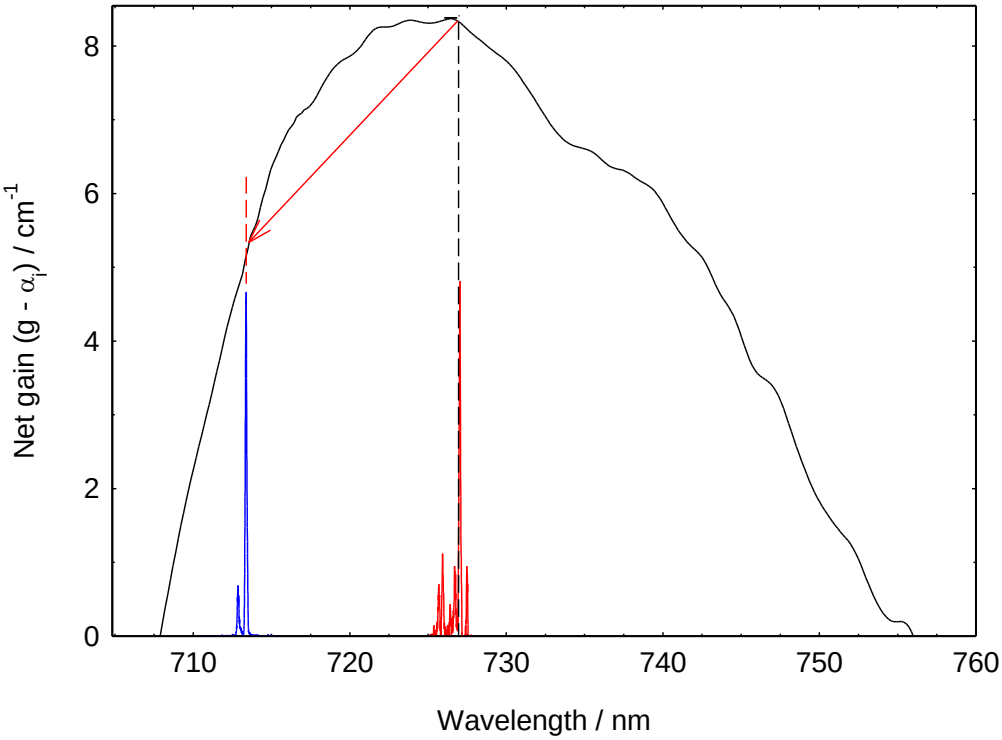

Figure 6-4: 300 K optical gain spectra at an injection current density relating to the threshold currents of a 1.5 mm long DBR and ridge laser. Also plotted here is the lasing wavelength spectrum of the corresponding devices (intensity is arbitrary) with the DBR laser emitting at a shorter wavelength. The arrow indicates the shift from the peak gain position. Multi-modal behaviour due to lateral modes is apparent in the laser spectrum.

6.3. Dual-λ Ridge Lasers

6.3.1. Principle of operation

It became apparent in chapter 5 that the gain-peak wavelength in this material system is strongly dependent on state filling. It is this material property which lends itself as a source for accessing multiple wavelengths. The effect of increasing the injection level and populating higher lying states can easily be seen in the ASE obtained from a segmented contact device, as shown in Figure 6-5, where a comparison is made between low and high injection. Due to a wide distribution of energy states between the two dot subsets, the amplitude of the ASE peak is observed to increase and shift to

shorter wavelengths as higher lying states are progressively populated, giving rise to a broad continuous gain spectrum. The advantage of this behaviour is that by changing the loss (by varying the cavity length) and hence the threshold current density (injection level), a relatively continuous variation in wavelengths can be sourced. This approach essentially yields the same result that is achieved by incorporating a DBR at the end of the cavity, the only difference being that the loss here is controlled by the cavity length and not the nature of reflectivity. The idea of coupling ridge lasers with different length cavities to produce two wavelengths is discussed in the following section.

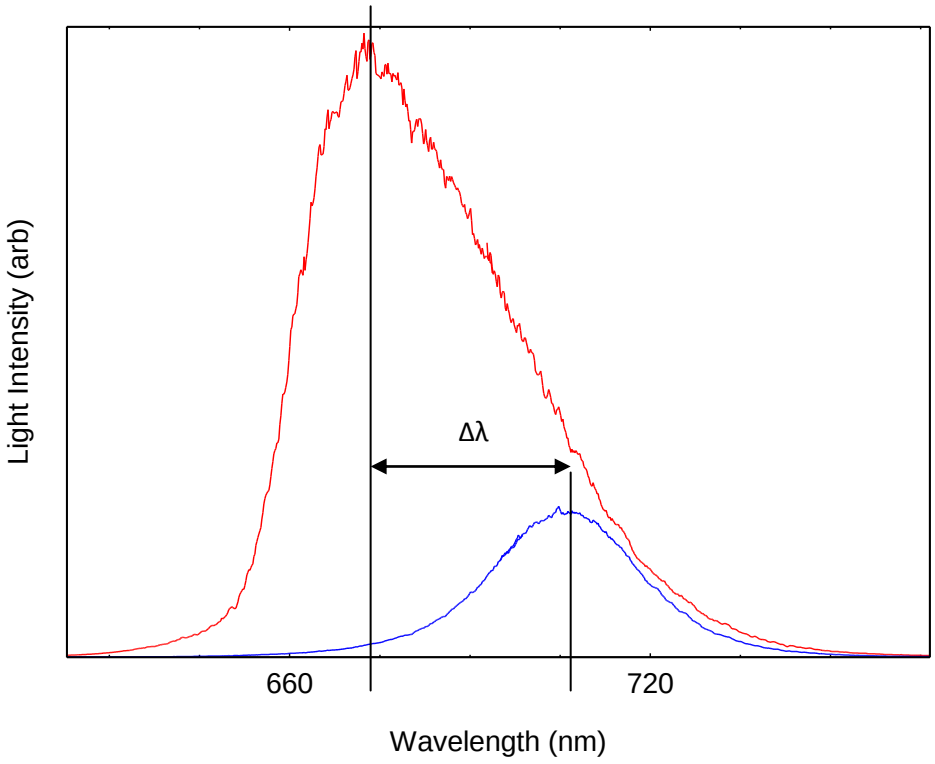

Figure 6-5: ASE spectra obtained from segmented contact device for low and high injection. Arrow indicates the shift in peak due to state filling.

6.3.2. Coupled cavity design

Coupled cavity designs have been studied and employed in a number of laser devices for various applications, including single longitudinal mode operation and high-speed frequency modulation [Tsang et al. 1983; Burrus et al. 1983; Jianglin et al. 1987]. The coupled-cavity laser fabricated in this work is formed from a RWG which has cleaved facets at either end and is divided into two sections by an etched gap. The length of these sections was made unequal so that the loss in each would be different and thus

allow for emission of two wavelengths. Separate metal contact pads were formed on each section of the RWG so that each wavelength could be operated simultaneously or independently. A schema of the device is shown below in Figure 6-6. The light output was measured from the cleaved facet of the front section, since this is the only facet which emits both wavelengths of light. The advantage of using this design is that the emission of the two wavelengths comes from a common aperture, making it simpler to collect the light using external optics or fibres.

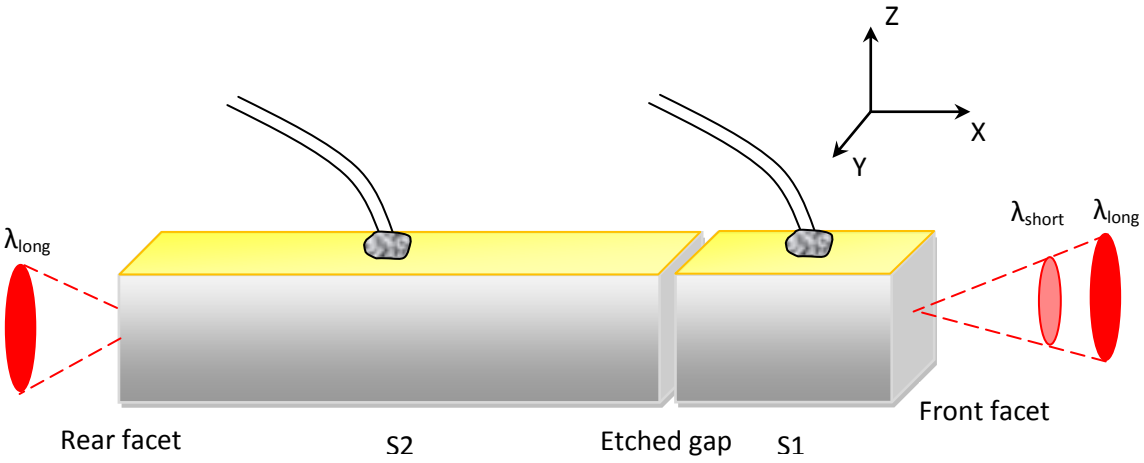

Figure 6-6: Schematic of a two-section coupled-cavity laser. The longer rear section (S2) provides the long wavelength and the short front section (S1) the short wavelength. The light output at both wavelengths is measured from the front facet.

To produce dual-λ operation using a coupled-cavity ridge laser, the two sections of the device must be pumped asymmetrically. To facilitate this, the sections need to be electrically isolated so no leakage current can flow from one section to the next. This was achieved by simply etching the gap between the two sections deep enough to prevent lateral current flow within the metallurgical junction. As a consequence of ARDE, discussed in Chapter 4, the etch rate within the gap is slightly less than the regions surrounding the ridge. Due to limitations of the laser interferometer, it is not possible to monitor the depth of the gap whilst etching. For this reason, it is necessary to account for the difference in etch rates. Here it was found that the etch rates were not that dissimilar, and etching down to the substrate outside of the confines of the gap would yield a sufficient gap depth.

Other techniques used for electrical isolation between sections of a device employ the use of proton implantation [Naderi et al. 2010], which can provide over 10 MΩ of

resistance between adjacent sections. However, the advantage of simply etching down to the substrate is that it requires no extra process steps and reduces the cost of fabrication. The only issue here is the loss experienced by the optical mode in transmitting across an etched gap. For simplicity, the RWG and the gap were etched in the same step and the gap was then filled with BCB during the planarization process.

The length of the sections (determined by the cleave locations) was chosen, with aid of the gain spectra, to obtain the required loss needed for a desired operating wavelength. When calculating the mirror-loss of the cavity in this device, it is important to account for both the reflectivity of the cleaved facet (from which the light output is measured) and the reflectivity at the gap. The contrast in refractive index between the semiconductor and BCB is less than between air and semiconductor, so transmission across each interface is increased. Consequently, this increases the mirror-loss of each cavity, which is detrimental to the front (short) section (S1) as a large portion of the light generated in this section is lost to the rear (longer) section (S2) via passive absorption. Conversely, increasing transmission across the gap is beneficial for S2 as the light generated in this section needs to propagate through both the gap and S1 to produce a useful light output from front facet. The reflectivity in both cases was calculated using Fresnel's equation for normal incidence.

Despite only having two contacts of injection the device can be operated in a number of different ways. Firstly, S1 can be operated to provide emission at the short wavelength and secondly it can be pumped with S2 to provide emission at the long wavelength. A third method of operating the device is achieved by floating the front the section, such that it acts as a passive absorber. In this situation the threshold current of the device is increased but the slope efficiency of the light-current (*L-I)* curve above threshold is higher. Operating a device in this regime can potentially be used to achieve self-pulsation of the optical mode; this topic is discussed later in Section 6.4.3 and 6.4.4. The final and perhaps most interesting method of operation is that which achieves dual-λ emission. Due to the relatively complex recombination dynamics of the different dot states, establishing a stable output at each wavelength requires accurately balancing the level of carriers injected into each section. Since a portion of the light from S1 passes into S2 it will optically pump that section.

Consequently varying the output of the short wavelength will give rise to a variation in output at the long wavelength. The opposite is true when the injection level into the second section is increased. Due to carrier competition of the two modes, increasing the light output at the long wavelength will stimulate further recombination into that mode. This consequently reduces the number of carriers available for recombination at the short wavelength; essentially the two modes are 'competing' for the injected carriers.

6.3.3. Coupled cavity: device measurements

A coupled-cavity laser was cleaved to obtain an S1 and S2 length of 500 µm and 2000 µm respectively. If these operated as individual devices then the net gain $(G - \alpha_i)$ imposed by these cavity lengths would be 30 and 7.5 cm^{-1} (taking into account the BCB/semiconductor interface). However, when operating as a coupled cavity the threshold condition depends on the operation of both cavities, as discussed later in this section. It was estimated from gain measurements that the chosen section lengths should yield emission wavelengths of approximately 720 nm (taking into account the length of S1 + S2) and 680 nm for S1. The device was placed in a cryostat and the electrical contacts of each section were connected into two synchronised pulse generators. The experimental setup used for measuring the light output was the same as that used for segmented contact measurements. The convenience of this setup, over one which utilises a wavelength scanning optical spectrum analyser OSA, is that the whole spectrum (or importantly both wavelengths) can be viewed simultaneously, allowing any changes due to variations in the current to be monitored in real time.

The two spectra shown in Figure 6-7 were obtained from asymmetrically pumping the sections of the device. The spectrum shown in red, where there is only emission at the short wavelength is for an S1 current of 78 mA and an S2 current of 32 mA. Fixing the current in S1, but increasing the current in S2 to 36mA (shown in blue) is enough to produce emission at both wavelengths simultaneously. The measured wavelengths here are 676.5 and 721 nm respectively, giving a separation of 44.5 nm. However, since the temperature dependence of the short and long wavelengths is not the same (0.04 nm/K and 0.16 nm/K respectively) the absolute separation depends on operating

temperature. The origin of this can be explained by the temperature dependence of the gain peak wavelength as discussed previously in Chapter 5. The difference in temperature dependence is a useful feature of the device as it allows the separation to be tuned by simply varying the operating temperature of the device, by using, for example, a thermoelectric cooler.

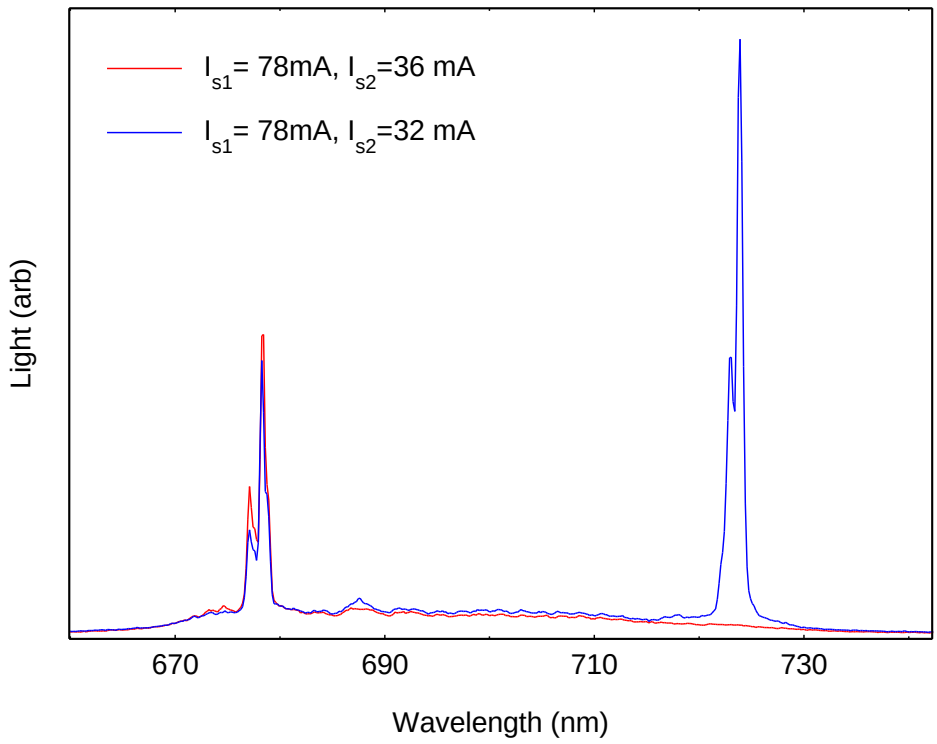

Figure 6-7: Coupled-cavity ridge laser demonstrating emission at 675.5 nm only (red) and simultaneously with emission at 721 nm (blue) by asymmetric pumping of the two sections.

A performance-limiting factor that arises when operating this device at both wavelengths simultaneously, is the competition for the available carriers distributed amongst the ensemble of states. The RWG was intended to be sufficiently narrow to limit the number of transverse modes and confine the two longitudinal modes to the same spatial region (as observed from the near-field of S1). In doing so of course, the two propagating modes within S1 interact with the same spatial distribution of carriers and the dynamics of capture and recombination within the different dot states becomes important.

Suppose that S1 is driven to transparency so that there is no net gain or absorption experienced by photons entering from S2. Threshold at the long wavelength is

achieved when the gain matches the loss experienced by the optical mode and the resulting emission wavelength reflects the degree of state filling required to reach this condition. In order to achieve laser emission at the short wavelength, the current in S1 must be increased to reach the required level of gain imposed by that section. However, increasing the number of carriers in this section will also increase the rate of stimulated emission at the long wavelength, suppressing the ability to populate higher lying states and reach the required quasi Fermi – level separation. A situation needs to occur where the level of gain in the S1 does not 'pin' at a value associated with the long wavelength. This cannot easily be achieved when threshold at the long wavelength has already been reached, as the light at this wavelength will tend to dominate with any extra injection of carriers. Instead, the threshold condition must first be met in S1. Increasing the current in S2 will begin to suppress the short wavelength emission due to carrier competition, but this can be accounted for by increasing the current in S1. Eventually a condition is reached where the number of injected carriers is sufficient to maintain both lasing modes simultaneously and by modulating the current, the power at each wavelength can be equalised.

The degree of suppression at the short wavelength can be significant, with even a small variation in the drive current of S2. For example,

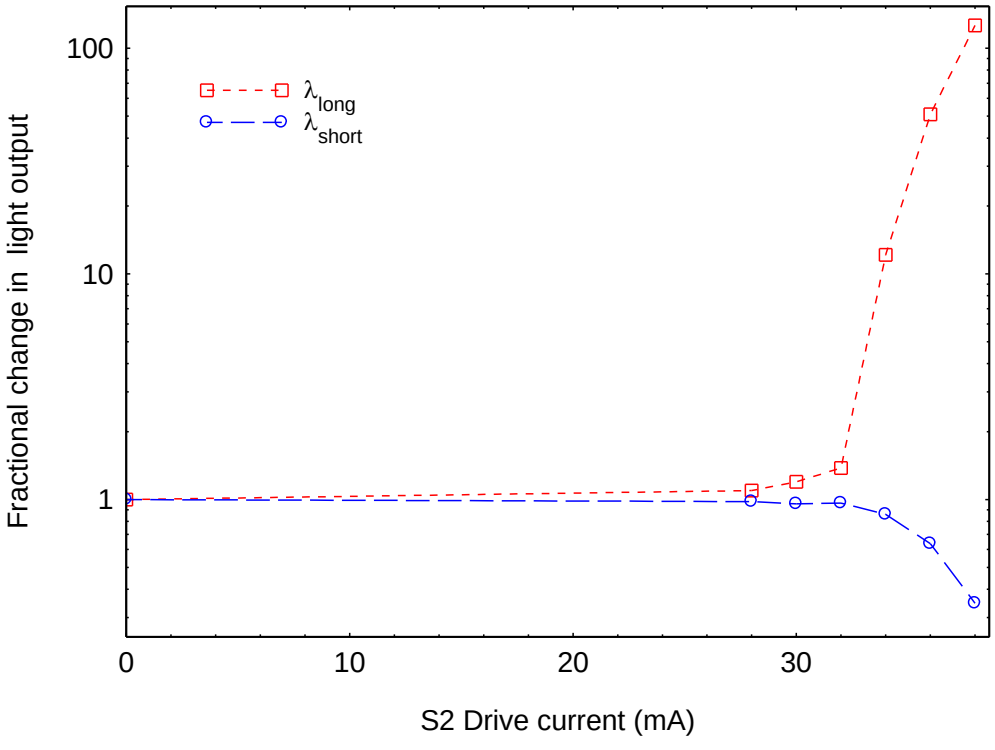

Figure

6-8 shows the fraction change in light output at each wavelength as measured from the facet of S1 versus the drive current to S2. At a drive current of 28 mA the light from the short wavelength falls by 2 %, but as the current is increased to 38 mA, this fall increases to 65 %.

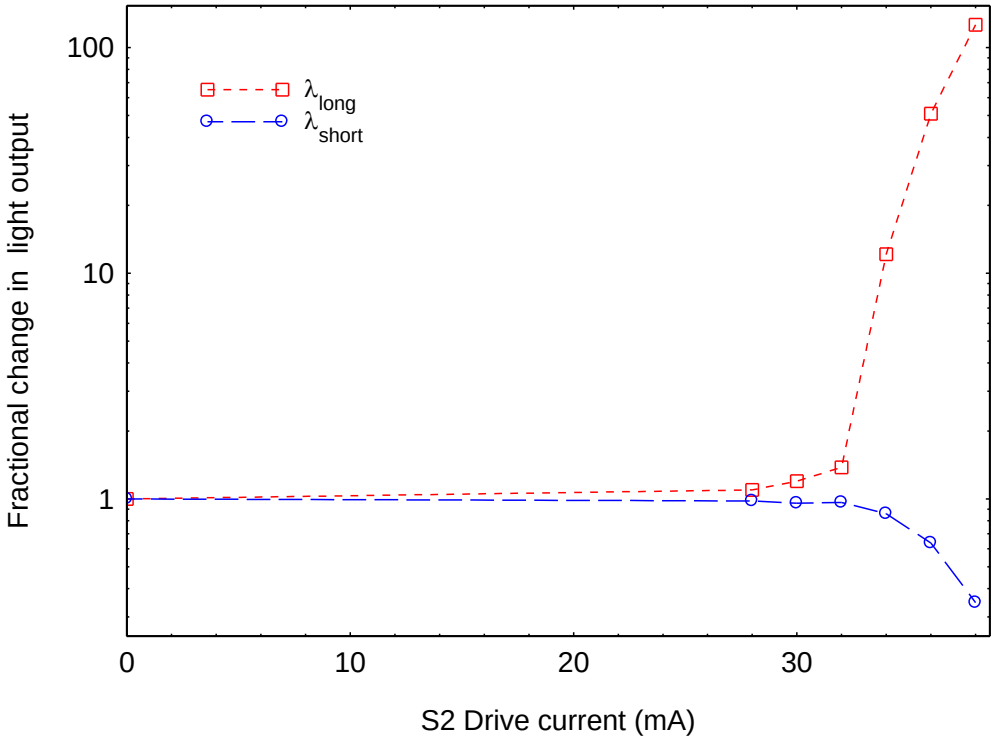

Figure 6-8: Illustrates the fractional change in the light emitted for λ_{short} (blue circles) and λ_{long} (red squares) with drive current to S2.

Asymmetrically pumping two unequal length sections of a coupled-cavity laser is an effective way of accessing the variation in wavelengths that are offered by the gain medium. By simply varying the loss, through choice of cavity length, we can access a modest variation in gain peak wavelength (via the effects of state filling). This has facilitated a separation of laser emission wavelengths of up to 44.5 nm. There are however limitations to this design and operation above room temperature results in very high threshold current densities and unstable behaviour. The following section discusses a method for improving device performance and achieving a greater separation of wavelengths, while operating at elevated temperatures.

6.4. Dual-λ Coupled-Cavity DBR Lasers

So far, the use of DBR gratings and the effect of state-filling on the gain-peak wavelength have been separately considered as techniques for varying the emission wavelength. This section pulls together the advantages realised from both these principles to describe a novel dual-λ laser.

6.4.1. Preferential feedback using DBR gratings

To date, there have been several reports in the literature of approaches used to achieve dual-λ emission from a semiconductor laser, and there are various advantages realised through each design. A ridge laser with a laterally coupled DFB has been used to generate dual-λ emission, where the gratings along each sidewall are designed to select two different wavelengths [Pozzi et al. 2006]. The authors report on stable dual-mode emission around 1347 nm with a wavelength separation of 0.15 nm. The two wavelengths were observed to emit in different spatial locations, which was identified by traversing a fibre across the facet of the laser. Another approach makes use of a RWG with a gain section and two surface-etched grating sections [Roh, et al. 1989]. Results are presented which show mode-pair separations of 4.1, 8.4 and 16.9 nm. Coupling between the optical modes and the grating structures was enhanced by growing an asymmetric cladding, with the upper cladding layer being thinner than the lower one. A more recent method, based on an InAs/InGaAs QD material system, uses a two-section laterally loss-coupled (LLC) DFB laser, which generates emission from the ground and excited state [Naderi et al. 2010]. The chrome grating, which is formed perpendicular to the ridge sidewalls, is coupled to the excited state only and emits at around 1193 nm, with the ground state emitting around 1235 nm. The two sections are electrically isolated by proton implantation, as described earlier, so that the sections can be pumped asymmetrically.

The dual-λ DBR device presented here is based around the coupled-cavity geometry, except the gap separating the two sections is replaced with a Bragg grating. To be effective, the grating needs to be highly reflecting at the short wavelength and offer a low level of reflection at the long wavelength. Ideally, the long wavelength does not ‘see’ the middle grating and propagates as a longitudinal mode defined by the entire

length of the device. The short wavelength on the other hand, meets a highly reflective interface and the asymmetry of the feedback now yields a larger portion of the light being emitted from the front facet, rather than being lost to S2 via passive absorption. To further improve the performance of the device, but not essential, is to have a grating placed at the rear end of S2 increasing feedback at the long wavelength. This grating was also designed to have a low level of reflection at the short wavelength, however if the level of inversion is low in S2 the Bernard and Duraffourg condition for light emission at the short wavelength is not satisfied; consequently reducing feedback at this wavelength is not necessarily required. A schema of the device is shown in Figure 6-9.

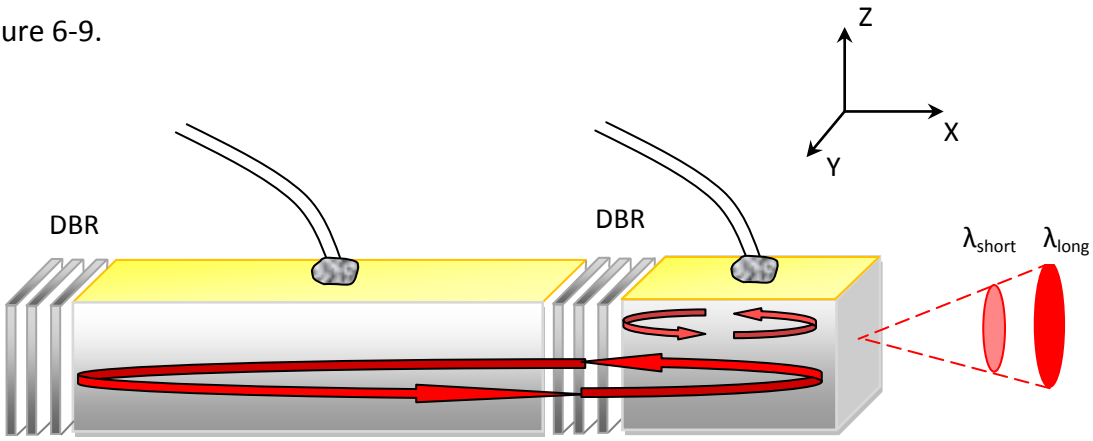

Figure 6-9: Schematic illustration of coupled-cavity laser with incorporated DBR gratings. Grating positioned between the two sections is designed to have low reflectance at the long wavelength and be highly reflective at the short wavelength, vice-versa for the rear grating.

As with the coupled-cavity device, electrical isolation of the two sections is achieved by etching the gaps in the grating portions down to the substrate. An additional advantage of etching to this depth is that there is no transverse (Z) variation in refractive through the optical waveguide. In surface grating lasers the variation in refractive index can have the effect of pushing the optical mode down towards the substrate as it propagates. Although this may have no appreciable effects on the power output of the laser, it is unlikely to yield emission of two wavelengths within the same spatial position, since the guiding effect may be wavelength dependent. This will of course have negative implications concerning the collection of both wavelengths through the same optics or fibre.

Etching closely spaced, high aspect ratio features in this material system is not a trivial matter and the developments made in order to achieve this were described in Chapter 4. The patterning of the grating portions also has a certain element of complexity due to the *proximity effect* (here the exposure of sub-micron features is affected by patterning of the ridge waveguide) and a method to account for this effect was described in Chapter 3.

The gratings were based on third order Bragg stacks and as with the DBRs described earlier in section 6.2, the peak of the centre grating stop-band is positioned such that the reflectivity, or feedback is higher at shorter wavelengths. In doing so, the loss of the cavity and the emission wavelength is now influenced by both its length and the nature of the reflectivity spectra attributed to the centre grating.

Measurements of gain spectra presented in the previous chapter show that under high injection the peak of the gain curve can blue-shift up to 50 nm. To achieve the largest wavelength separation, a grating structure was designed where the reflectively would only rise above that of a cleaved facet at the short wavelength limit of the material, accessed by high injection. The original motivation for pushing the limits of the wavelength separation within this material was the possibility of generating emission at 650 and 780 nm, the read-write wavelengths of DVDs and CDs. The current technology makes use of two separate sources to achieve emission at these two wavelengths. From the absorption and spontaneous emission spectra, it is apparent that emission at 650 nm would have to come from carrier recombination within the QW states (this would require altering the loss of the cavity substantially to suppress laser emission from the dot states). Although 780 nm is beyond the limit of long wavelength emission offered by the samples measured in this thesis, InP/AlGaInP materials demonstrating optical gain at this wavelength have previously been measured [Smowton et al 2005]. An example of a centre grating reflectivity spectra used to achieve a large wavelength separation is shown in Figure 6-10. The reflectivity is low at the longer wavelength with the intention of suppressing laser emission from the large dot states.

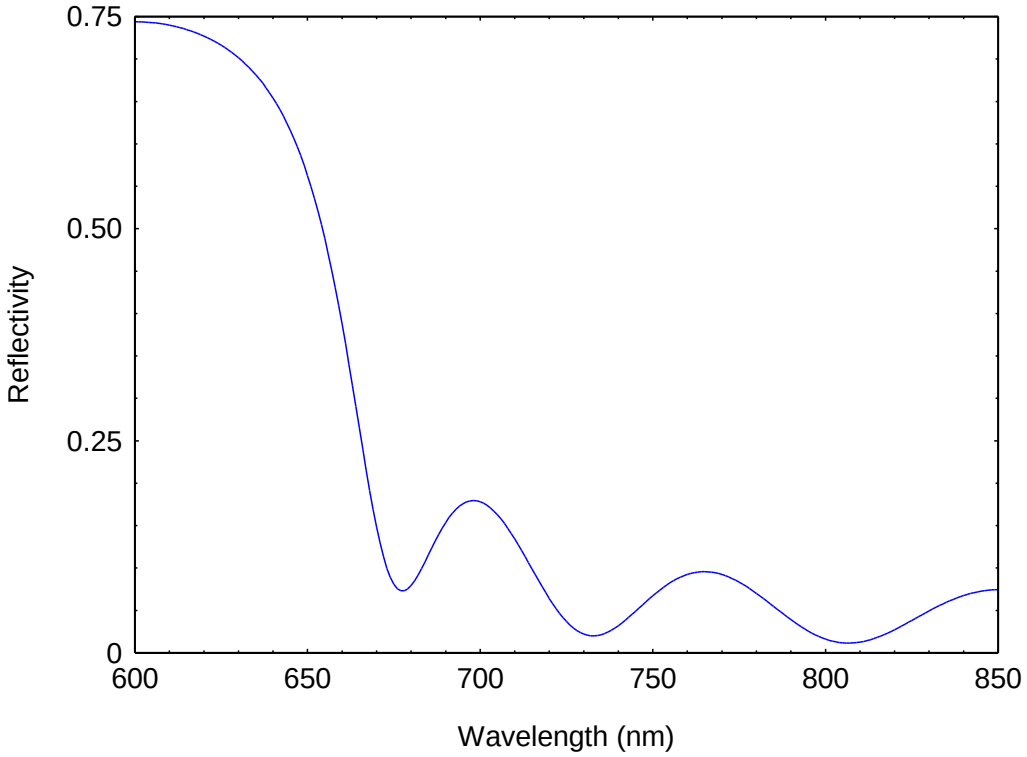

Figure 6-10: Calculated reflectivity spectra for centre grating to achieve emission at short wavelengths.

With reference to the round-trip gain equation described in Chapter 2, the overall mirror loss *($\alpha_m(\lambda)$)* of the short section is dependent on its length *(L_c)* and the reflectivity of both the cleaved facet (*R_f)* and the DBR grating *($R_G(\lambda)$)*:

$$\alpha_m(\lambda) = \frac{1}{2L_c} ln\left(\frac{1}{R_f R_G(\lambda)}\right)$$

Equation 6-1

This equates to the net-gain requirement which must be achieved in order for laser action to take place. The mirror loss, now spectrally dependent, is shown in Figure 6-11 together with a gain spectrum obtained at high injection. When the level of pumping is sufficient, the gain curve meets the loss spectrum. The point at which this occurs corresponds to the wavelength at which a laser would emit under these conditions and it does not necessarily coincide with the gain peak. The gain requirement at wavelengths above this dramatically increases and hence emission at longer wavelengths is not possible.

This method of modifying the loss spectrum of the short section using the centre grating allows for a greater separation of emission wavelengths, increasing the 44 nm achieved with the coupled-cavity to 61.5 nm as depicted in Figure 6-12.

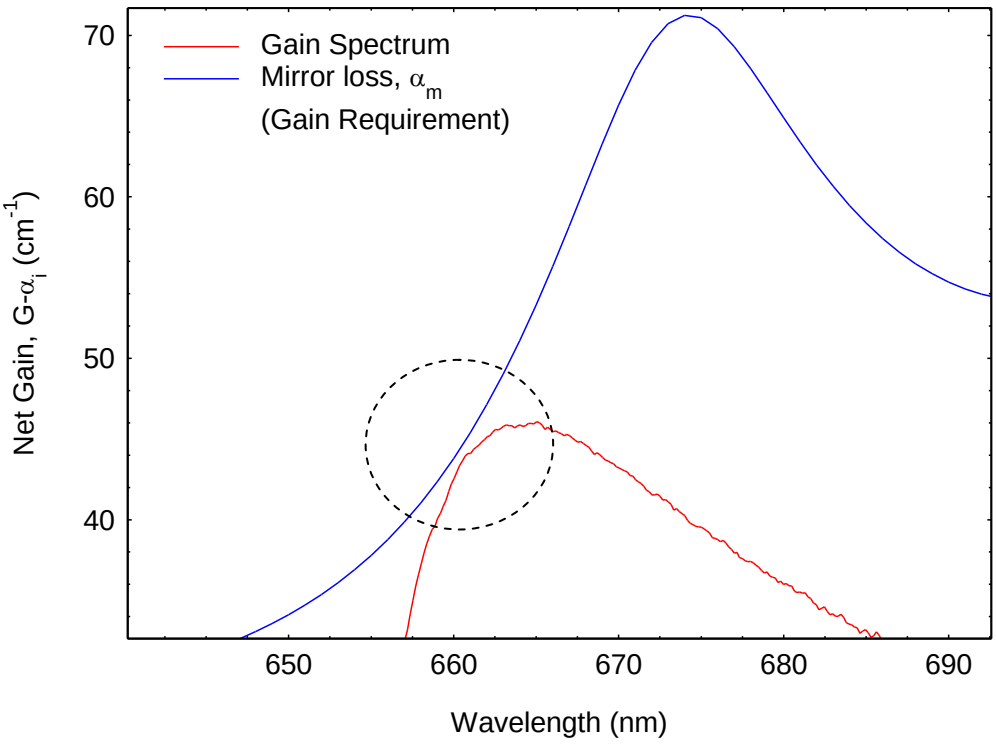

Figure 6-11: Peak of the net-gain spectra (G-α_i) plotted with mirror loss spectra (α_m) obtained from equation Equation 6-1 using the reflectivity spectra in Figure 6-10. When the level of pumping is sufficient, the gain meets the loss spectra (inside dashed circle) and laser action occurs.

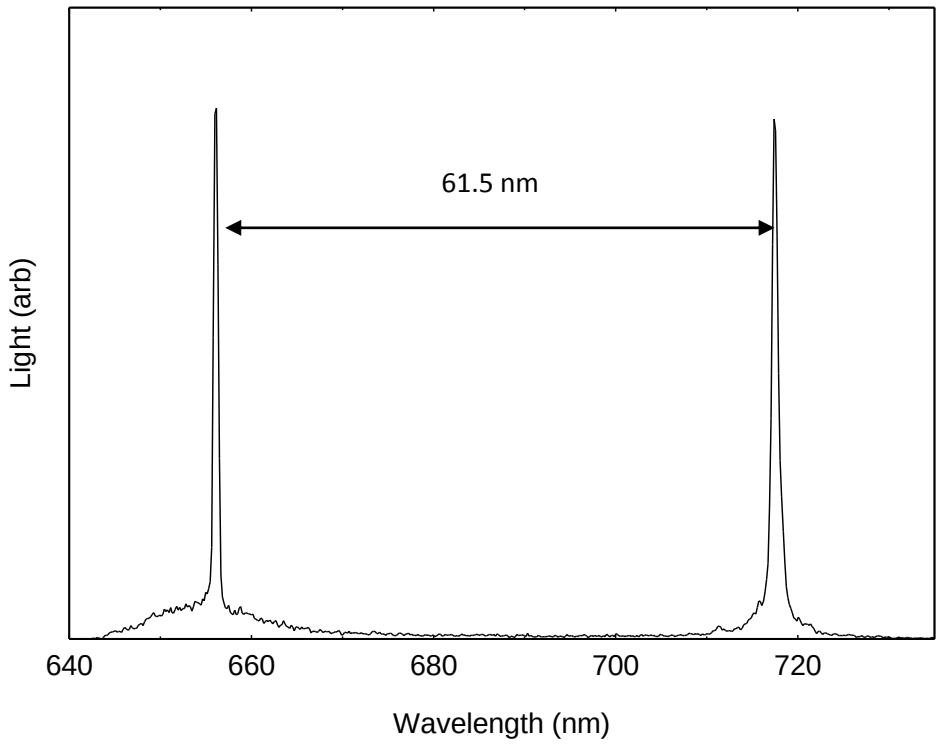

Figure 6-12: An emission spectrum from a coupled-cavity DBR laser with an S1 length of 300 µm, showing dual-λ operation from the same active layer, with a separation of 61.5 ± 0.2 nm.

As described in Equation 6-1, the mirror loss is inversely proportional to the cavity length. The effect of increasing the cavity length from 300 to 500 µm is shown in Figure 6-13 and results in a lower gain requirement. Since the loss spectrum is shifted down, the point at which the gain first matches the loss, (threshold in short section) occurs at a longer wavelength and this reduces the separation in the two emission wavelengths as shown in Figure 6-14.

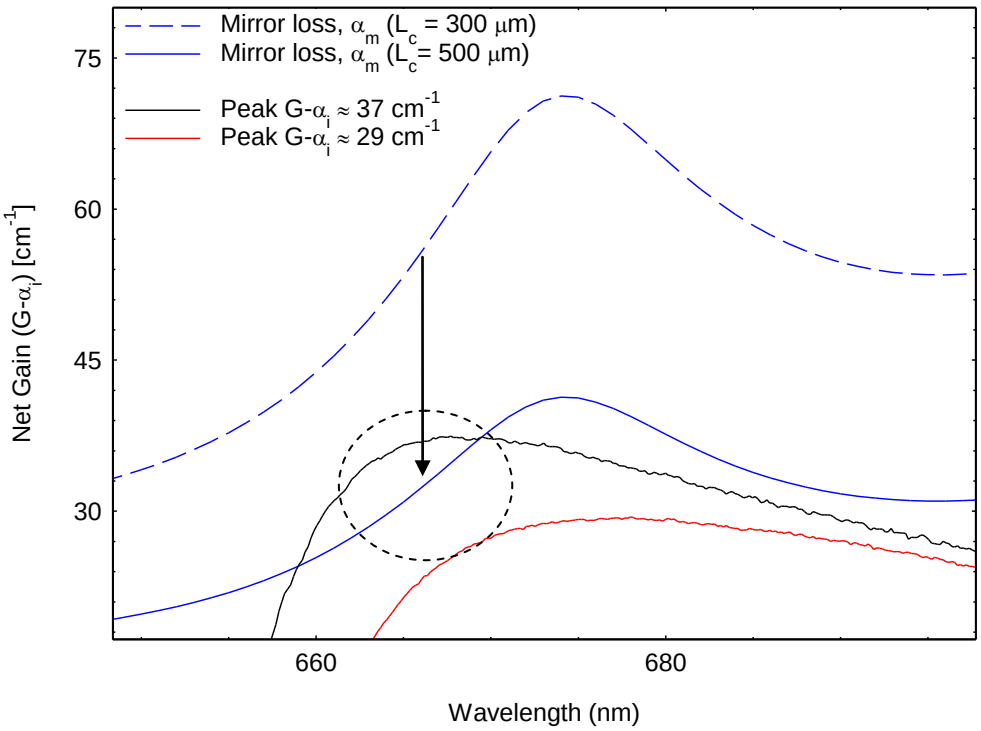

Figure 6-13:Shows the peaks of two gain spectra (G-α_i) plotted with mirror loss spectra (α_m) obtained from equation Equation 6-1 using the reflectivity spectra in Figure 6-10. The solid blue line shows how the loss spectrum is modified from the dashed line when the cavity length is increased. Arrow illustrates that the loss spectrum is shifted down for a longer cavity.

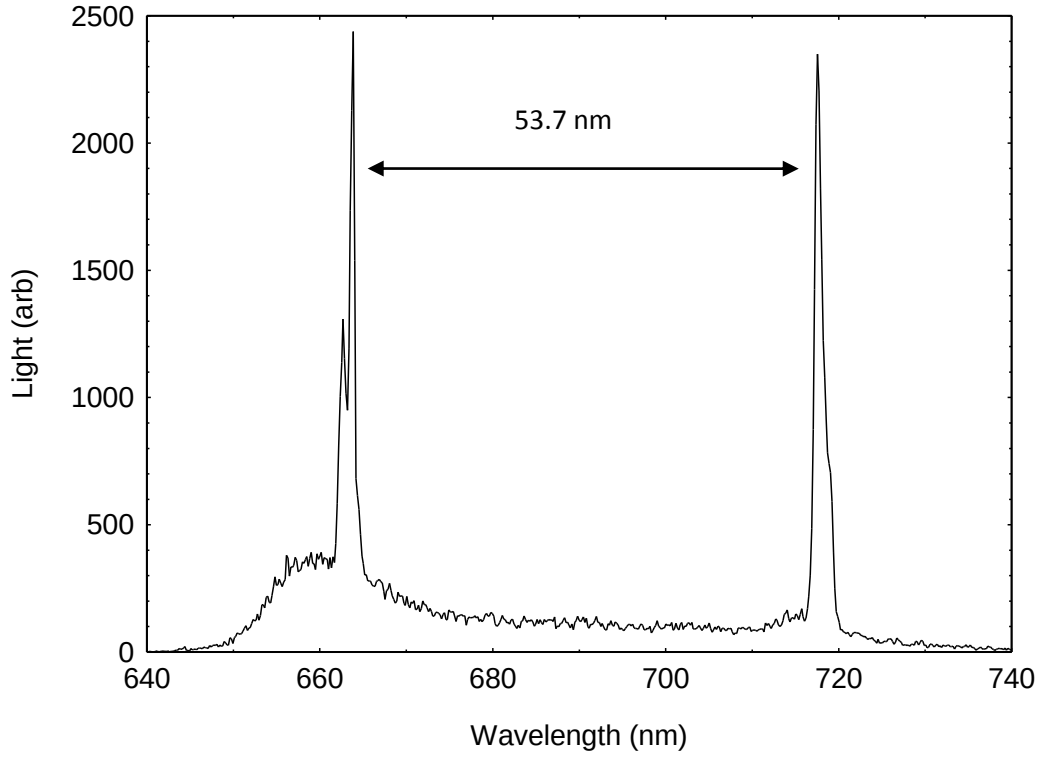

Figure 6-14: An emission spectrum from a coupled-cavity DBR laser with a longer (500 μm) S1, showing dual-λ operation with a separation of 53.7 ± 0.2 nm.

The light output at the short wavelength has good stability, even when the output at the longer wavelength is varied. For example, the plot in Figure 6-15 shows the fractional change in light output at each wavelength as the injection into the long wavelength section of the device is increased. The current providing the short wavelength emission was initially set to 10 % above threshold. As the light output at the long wavelength increases the short wavelength output remains relatively unaffected, suggesting that carrier competition between the dots states involved here is not significant enough to suppress dual-λ operation. The inhomogeneous nature of QDs is known to reduce the fluctuations in power between lasing modes and this is an important feature as it improves the stability of a dual-wavelength source [Capua et al. 2007; Daghestani et al. 2011]. The fluctuation in power of each mode is related to how the optical transitions involved compete for the available carriers. Interestingly, suppression of the short wavelength observed here is less for the larger wavelength separation. This may suggest that the carriers supplying the two modes in this case are sourced from states which are populated independently. In terms of wavelength variations with drive current, the long and short wavelengths remain constant to within a 0.17 nm tolerance. At higher temperatures this was observed to increase slightly for the long wavelength emission; for example over a S2 current range of 22 mA there was a red-shift in the peak wavelength of 0.49 ± 0.17 nm. The cause of this is uncertain, but may be due to self-heating effects which occur at higher injection currents.

An advantage of this device over the coupled-cavity design without DBRs is the relatively low threshold current at which the device can be operated as a single laser. When driving both sections together (emission at the long wavelength), the room temperature threshold current was measured to be 144 Acm^{-2}, lower than the projected J_{th} of an equivalent length oxide-isolated stripe laser and substantially less than the coupled-cavity device, which operated at 580 Acm^{-2}. This performance enhancement is due to a combination of the increased reflectivity offered by the rear DBR and the intention of the centre grating having minimal reflectance at the long wavelength.

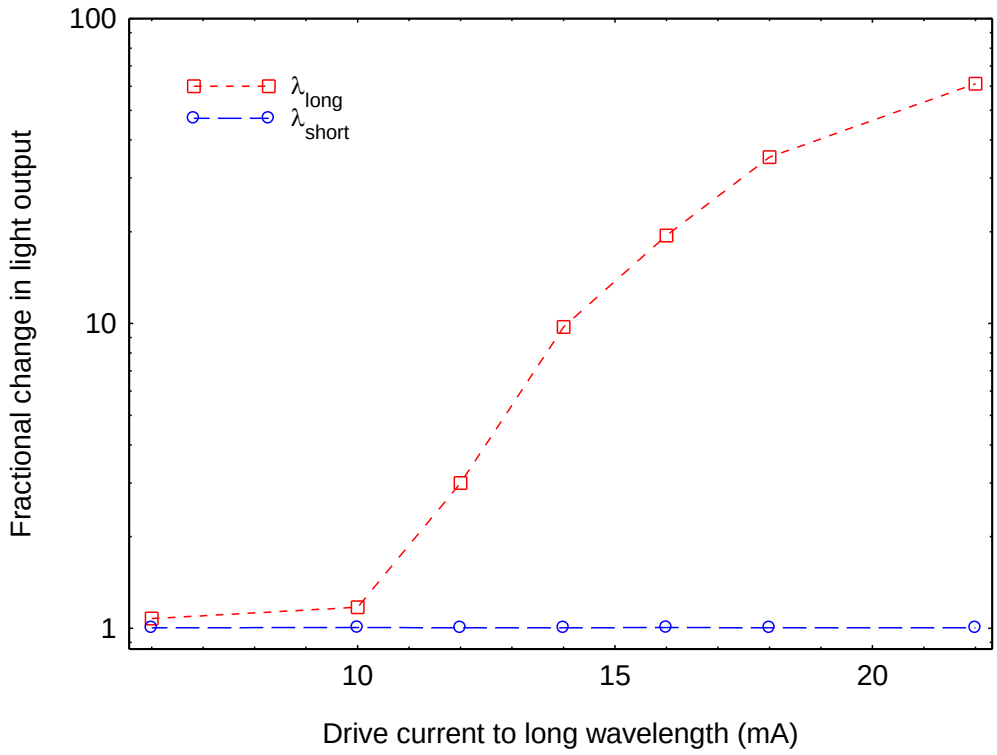

Figure 6-15: Illustrates the fractional change in the light emitted at λ_{short} (blue circles) and λ_{long} (red squares) with drive current to S2.

It is apparent that the stability, or range of pumping conditions over which dual-mode operation can be achieved is dependent on the difference in the gain requirement of the two modes, the way carriers distribute amongst the dot states involved, and how effectively the centre grating operates as a selective filter.

To gain further insight into the intensity stability at the two wavelengths, the light level from each mode was initially set to be equal, and then the fractional change in light at each mode was monitored as the current in each section was varied. Figure 6-16 shows that, as expected from the previous experiment (Figure 6-15), the light level at the short wavelength remains relatively fixed for changes in current applied to section two. Conversely, varying the current applied to section one causes the light output at both wavelengths to change, and as discussed previously, this is due to two effects. Firstly, increasing the current in section one increases the number of carriers available to recombine at each wavelength, and secondly, a proportion of the light generated from the high energy states of section one is transmitted through the centre DBR optically pumping section two.

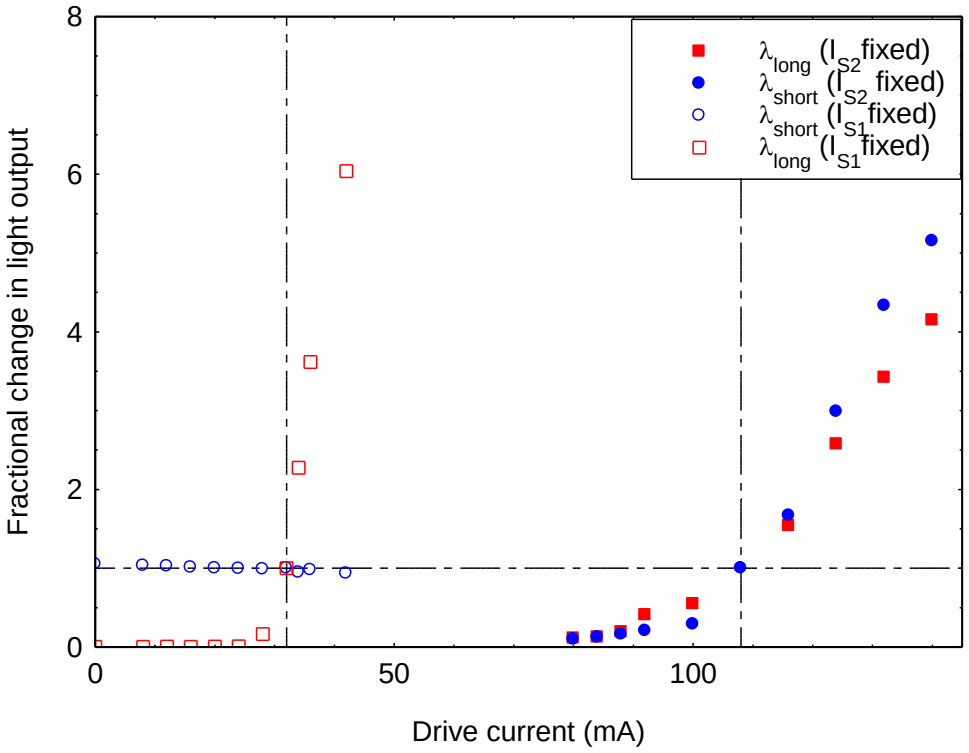

Figure 6-16: Fractional change in light intensity at each wavelength (λ_1, λ_2) when fixing the current in one section while varying the current applied to other. The point at which the dashed lines cross corresponds to the initial conditions where the light intensity in each mode was equal. The wavelength separation was measured to be 61.5 nm.

The gain requirement of the mode which emits at the long wavelength is relatively low, and so the level of injection required to reach threshold is much less than that of the short wavelength. Therefore, the number of carriers that the long wavelength mode is competing for over the length of section one is small compared to the number required to sustain lasing at the short wavelength. This effect can be appreciated by considering that recombination at the short wavelength is supplied with carriers from dots with a higher density of states, with operation occurring at a more saturated region of the gain-current curve. Therefore, any variation in the number of carriers will have little influence on the light output compared with the long wavelength, which operates with low injection on the steeper region of the gain-current curve.

To investigate how wavelength separation affects mode stability, the same experiment was performed on a device with a 17 nm separation and the results are shown in Figure 6-17. As with the wider (61.5 nm) wavelength separation, the light intensity at both wavelengths has a similar dependence when varying the current supplied to

section one. However, when the current to section two is increased, there is a reduction in the light intensity at the short wavelength and carrier competition between lasing modes is higher than that seen for the device with a larger wavelength separation. This is because the carrier densities utilised by the different dot states are more comparable as the wavelength separation is reduced i.e. the modes operate with a similar gain-current dependence.

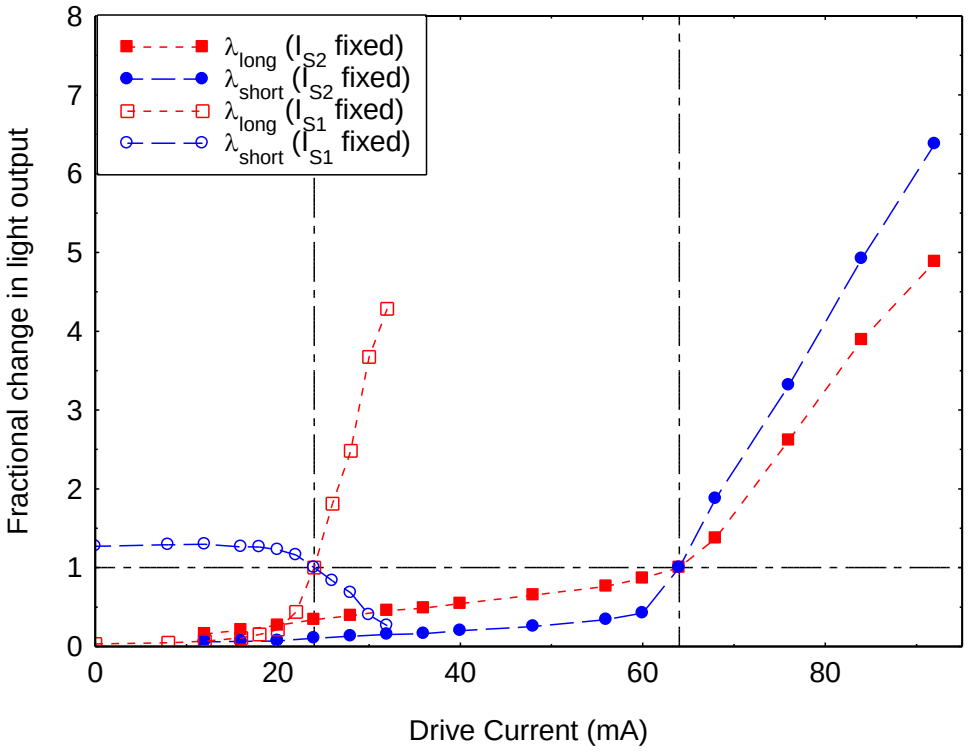

Figure 6-17: Fractional change in light intensity at each wavelength (λ_1, λ_2) when fixing the current in one section while varying the current applied to other. The point at which the dashed lines cross corresponds to the initial conditions where the light intensity in each mode was equal. The wavelength separation was measured to be 17 nm.

6.4.2. Temperature dependence of emission wavelength

The separation of wavelengths does vary with temperature and this is attributed to both the gain-peak wavelength dependence and the relative change in position of the gain-peak to the reflectivity stop-band. The peak reflectivity of the long wavelength stop-band was intentionally positioned at the longer wavelength limit of the gain spectra at 300 K (close to the band edge), to ensure that the emission would occur from the larger dot states. In doing so, the increase in threshold current with

temperature at the long wavelength should be reduced, as the gain spectrum is red-shifted with temperature. Although this does not improve the temperature dependence of the long wavelength emission, it does mean that lasing up to 380 K can be achieved with a reasonably low threshold current density of ≈ 800 Acm^{-2}.

The temperature dependence of emission wavelengths is shown in Figure 6-18 and as with the coupled-cavity device the absolute separation can be controlled by the temperature. For example, for the device shown here the change in separation of wavelengths with temperature is 0.11 nm/K.

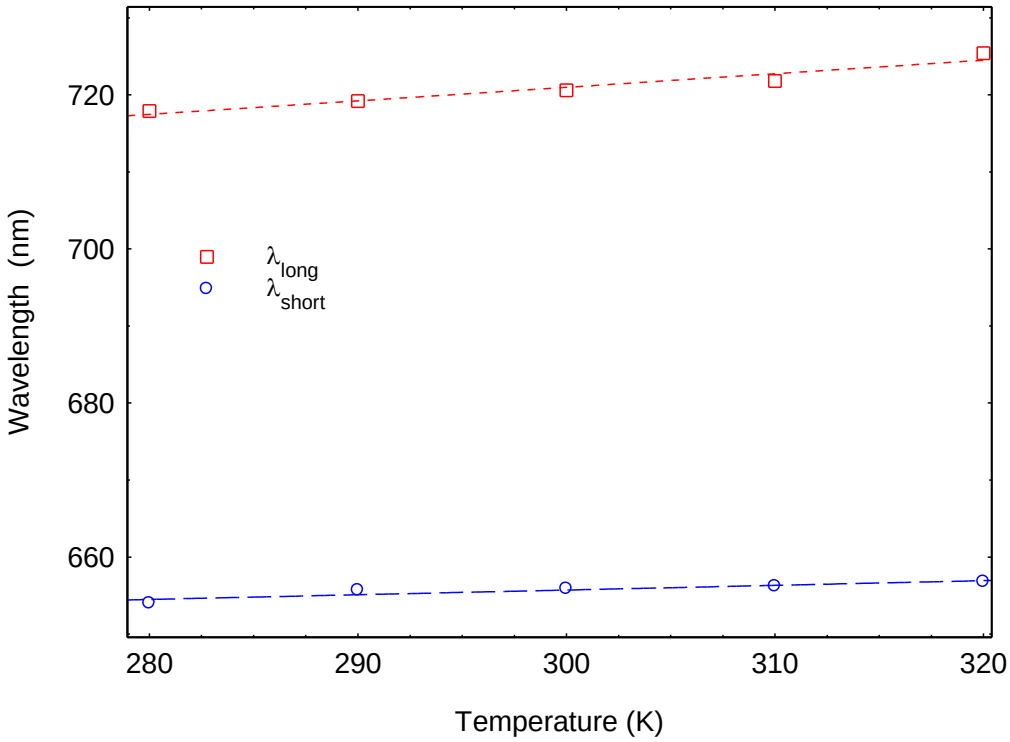

Figure 6-18: Temperature dependence of each wavelength when emitted simultaneously. The dependence is ≈ 0.17 and 0.06 nm/K for λ_{long} and λ_{short} respectively.

6.4.3. Light-Current Characteristics

The optical power output at each wavelength was measured as a function of drive current using an integrating sphere, as described in Chapter 3. Figure 6-19 shows a plot of the resulting *P-I* curves for driving the two sections (S1, S2) separately and together (S1 + S2). Despite being the shortest section, the threshold current of S1 (≈ 100 mA) is much higher than that observed for S2. The increase in drive current as cavity lengths become increasingly shorter was explained in the previous chapter. In addition, here

the loss of the cavity is also governed by the reflectivity stop-band of the gratings. Due to the higher operating current of S1 there will also be an increase in carriers recombining via parasitic processes and possible leakage paths, which consequently reduces the slope efficiency above threshold. The spontaneous emission will also be higher in S1 and the effect of this is evident by the increase in optical power produced by the ASE, as seen in *P-I* curve before threshold is reached.

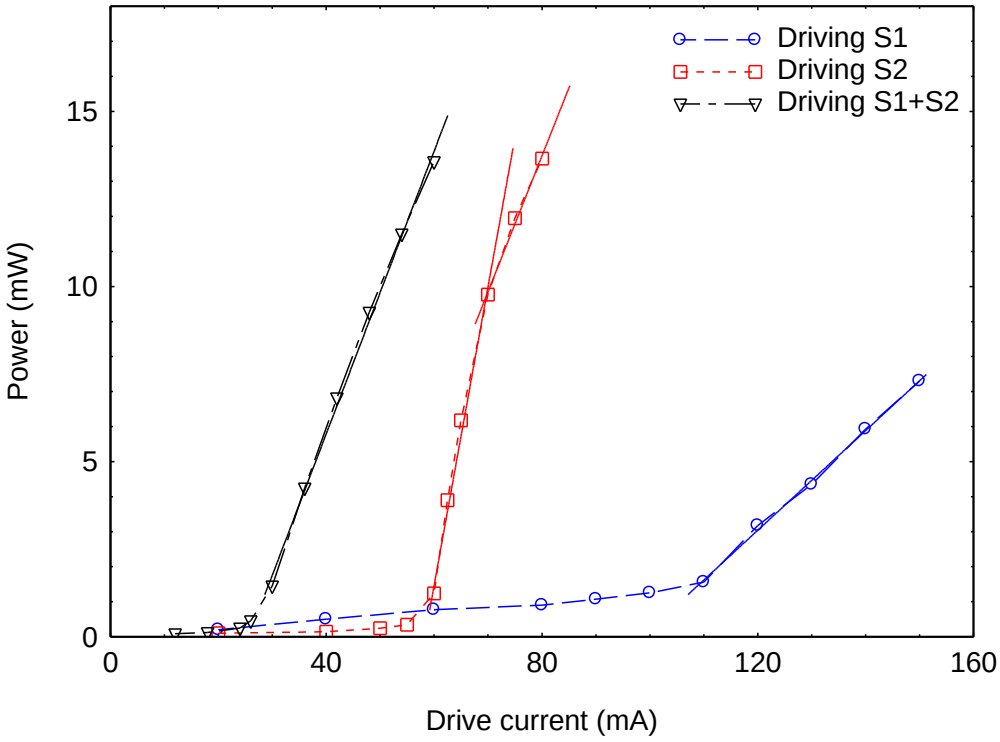

Figure 6-19: *P-I* curves for dual-λ DBR laser, driving S1 only (blue circles), S2 only (red squares) and S1+S2 (black triangles).

The *P-I* curve corresponding to the case when both sections are driven together has the lowest threshold current. As mentioned above, this is much lower than the threshold current of an equivalent length coupled-cavity device, due to preferential feedback provided by the two gratings. The slope efficiency above threshold is higher than in the case where only S1 due to the higher injection level. When operating S2, whilst leaving the electrical connection to S1 as an open circuit, the threshold current is increased relative to pumping the device as a whole. In this regime, S1 acts as a passive absorber to the light entering from S2. This effectively increases the loss of the

cavity and threshold can only be reached once a certain level of inversion is achieved in S1. As threshold is reached, the loss of the cavity is reduced (via optical pumping from S2), until it is low enough that feedback from the front facet is sufficient to sustain laser action. Initially, as the current is increased beyond threshold, there is a sharp rise in the optical output and this is due to a loss varying mechanism in the absorber section (S1). Even though laser light propagates over the entire length of the device, transparency in S1 is not yet reached in this regime of operation. An increase in the current delivered to S2 leads to an increased optical pumping of the absorber section and hence the loss continues to reduce until transparency is reached. The point at which this occurs is signified by the kinked feature observed in the *P-I* characteristic seen in Figure 6-19. At currents above this, the slope of the *P-I* curve is similar to when S1 and S2 are pumped together.

By only injecting current into S2, the principle of operation is similar to that employed in Q-switched devices. These lasers use a saturable absorber section, which is either active or, as in this case, passive. By lowering the attenuation of the absorber, for example by optically pumping it, the loss of the cavity reduces and this corresponds to an increase in the *quality factor* or *Q-factor*. When the Q-factor increases, a situation occurs where the level of gain exceeds the loss of the cavity and results in a sharp rise in the light output.

6.4.4. Spatial and Temporal Coherence

From an application perspective, it is beneficial if the emission of both wavelengths coexist both spatially and temporally. In terms of spatial coherence in the near-field profiles, the task of collecting light from the same region of the facet can be done easily using a simple lens system. Incidentally, characterising the resulting far-field is important since the light may be coupled into an optical fibre. The amount by which light spreads out as it evolves into the far-field will be governed, to some extent, by the emission wavelength and efficiency in collection will depend on how different the resulting profile widths are.

Temporal coherence is also an important issue, not only concerning the impact on certain device applications, for example generating Terahertz emission, but also the

implications on the physics of population dynamics and carrier competition of the dot states. In this section, results are presented in an attempt to ascertain the spatial and time dependent behaviour of each wavelength emitted. It was determined that in all cases of device operation, the emission was dominated by the Transverse electric (TE)-mode. All experiments were performed with a polariser orientated to accept TE emission.

i). Optical Near-Fields

The setup described in Chapter 3 was used to measure the near-fields of a dual-λ device at both emission wavelengths. The data plots in Figure 6-20 show the near-field profiles obtained in the plane of the active (y-direction) and in the direction of confinement (z-direction) as depicted in the schemas. The four profiles in each orientation correspond to different regimes of operation. From bottom to top: S1 only, S2 only (S1 absorbing), S1+S2 (symmetrical pumping of S1 and S2) and S1, S2 (asymmetric pumping for dual-λ).

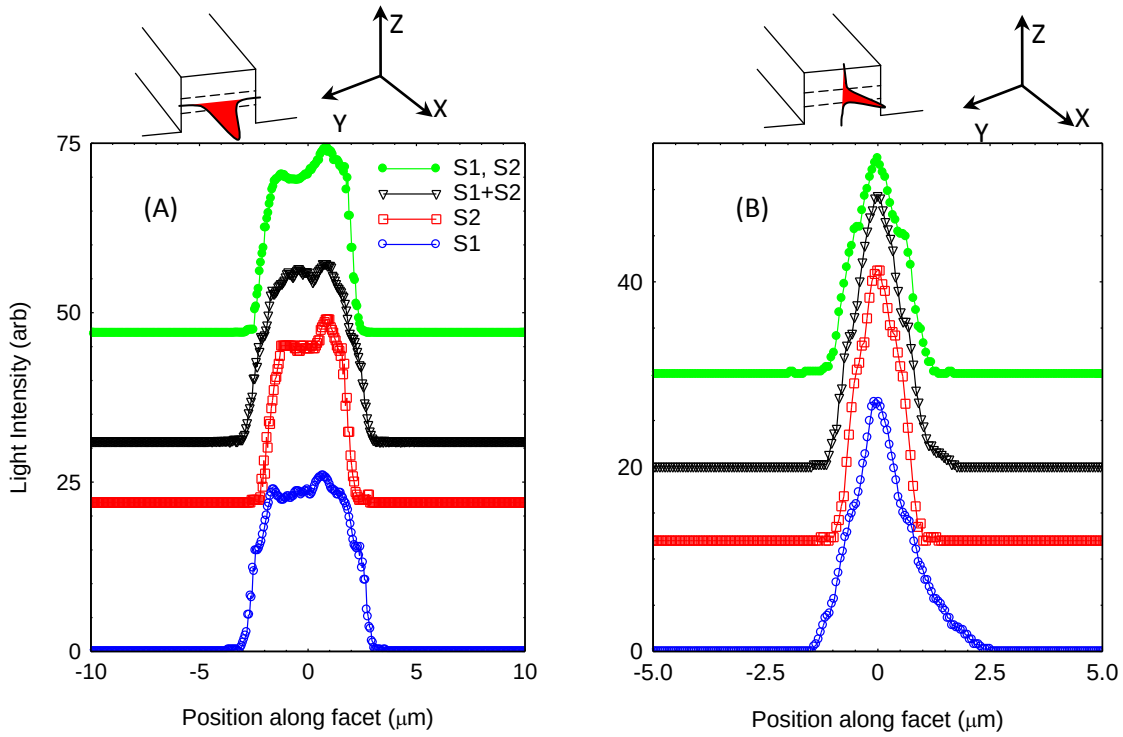

Figure 6-20: Near field profiles for different regimes of operation measured at the facet in the plane of active (a) and in growth direction of the active (b), as shown in the relevant schematic. Each data plot is offset for clarity.

Concentrating firstly in the y-direction, the near-fields show a sharp rise in light level defined by the boundary of the ridge sidewalls: significantly more abrupt change than in gain-guided devices. The advantage of the ridge design is that the light is confined laterally, so limits the tendency for multiple filaments to form, again a characteristic of broad area gain-guided devices. There is however, a slight asymmetry in the profiles seen in all regimes of operation. The dominant peak appearing to the right (≈ +1 µm from centre) is most pronounced when pumping S2 only or S1 and S2 asymmetrically. The question arises as to whether the ridge supports two spatially separated modes, each associated with a different wavelength. The feature may be due to non-uniformity within the structure of the device and to within the resolution of the experiment (±0.08 µm), there does not appear to be two clearly defined modes. The fact that the S1 profile has a similar shape, albeit to a lesser extent, suggests that wavelength-dependent multimodal behaviour may not be present. It is likely that the asymmetry is exaggerated by the emission at the long-wavelength as this is a favourable region for propagation of the optical field.

The FWHM of the near-fields in the y-direction are not that different in the various regimes of operation apart from the case of pumping S2 only. The FWHM is observed to be narrower and this is ascribed to the effect of absorption experienced by the mode as it traverses S1. When the light from S2 enters S1, it is most intense at the centre of the profile and the projection of this is seen in the degree of optical pumping along the length of S1. This effect results in a laterally varying loss profile, the magnitude of which depends on the S2 drive current. As the current increases, the level of optical pumping increases and S1 becomes progressively less absorbing. This, coupled with the fact that the trailing wave-train is also most intense at the centre, creates a narrowed profile at the facet of S1, an effect which is similar to the self-focussing observed in gain-guided devices.

The near-field profiles in the transverse (z) direction (Figure 6-20.B.) relate to the same regimes of operation as the lateral (y-direction) near-fields. These profiles are much narrower due to the confinement of the optical waveguide. The FWHM varies between 1.1 and 1.6 µm, with the narrowest and widest corresponding to driving either S2 or S1 respectively. The wider profile observed from driving S1 can be attributed to the

increased ASE and unguided spontaneous emission associated with the relatively high drive currents. The narrowing of the optical field seen when operating S2 only is the same effect occurring in the lateral plane, explained above. Under each regime of operation, or importantly for each wavelength, light emission from the front facet occurs in the same spatial region. As mentioned previously, this may not be the case if a surface grating was used, as then the mode would tend to be pushed down towards the substrate due to the vertically varying refractive index. The extent to which this occurs is likely to be wavelength dependent and therefore not so attractive for dual-λ devices.

ii). Optical Far-Fields

The transverse (z-direction) far-field distributions of both wavelengths were measured using the setup described in Chapter 3. The Gaussian-like profiles obtained from these measurements are shown in Figure 6-21, where the characteristic FWHM are very similar at 45 and 48 ± 1.5 ° for the long and short wavelengths respectively. In terms of collection issues due to beam divergence, it is the transverse far-field which is the limiting factor, with the divergence being much greater than in the lateral plane (y-direction). The far-field pattern, referred to as Fraunhofer diffraction, evolves from the near-field pattern (Fresnel diffraction) as described by the Huygens-Fresnel principle and the mathematical functions describing each of them are Fourier transform pairs. It therefore follows that a narrow near-field width gives rise to a wide angular far-field and vice-versa. As confirmed by the near-field profiles, the transverse confinement of the heterostructure (defined by the dimensions of the epitaxial layers) is much greater than the lateral confinement (defined by the ridge walls). The far-field angular width in the lateral direction was measured to be within 15° for both wavelengths, significantly less than the transverse far-fields.

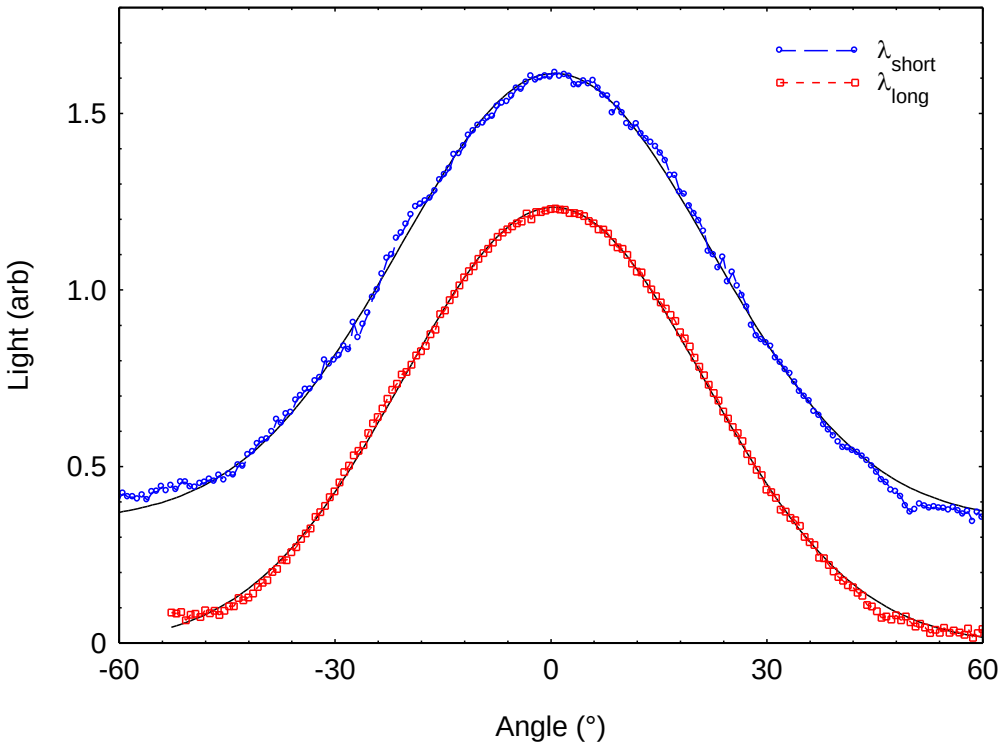

Figure 6-21: Gaussian profiles obtained from Far-field emission for each wavelength at room temperature. λ_{long} (circles) and λ_{short} (squares) have a FWHM of 45 and 48° respectively.

iii) Temporal measurements

Measurements of the lateral and transverse near-fields revealed that the optical modes associated with both wavelengths co-exist in the same spatial region. If this is the case, then it invokes the question about whether or not, under these levels of injection, the material can support emission at both wavelengths simultaneously. Time-resolved images of emission spectra were obtained using the streak camera system described in Chapter 3.

Whilst capturing images of the light emission it was noticed that the intensity fluctuated over its pulse duration. It was revealed that these fluctuations correlated with variations in the current pulse. An example of this is shown below in Figure 6-22, where the current pulse, as measured using an oscilloscope, is plotted with a time-resolved emission spectrum at threshold. The sharp spikes occurring at the start and end of the current pulse coincide with the 'hot spots' at each end of the emission spectrum and similarly for the fluctuations in between. Subsequent time-resolved measurements were therefore taken within the stable portion of the current pulse.

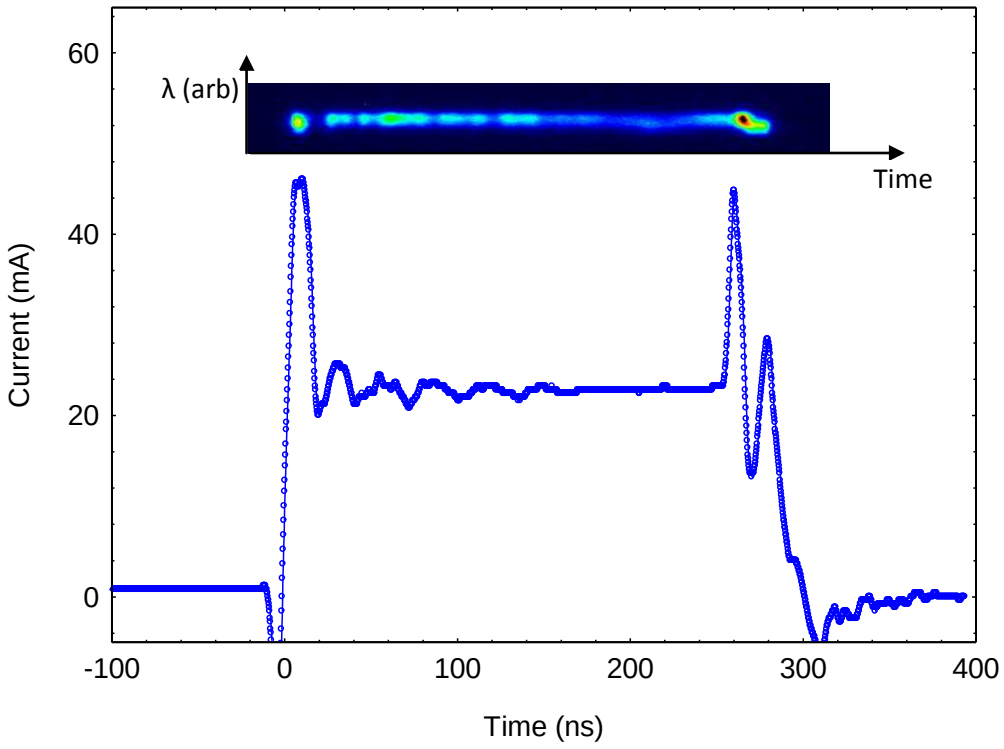

Figure 6-22: Current pulse taken from oscilloscope together with time-resolved laser emission. Fluctuations in the light intensity correspond to spikes in current pulse.

Two separate constant current sources were used to 'asymmetrically pump' each section of the device, with one source being triggered by the other to ensure synchronised pulses. A plot of the emission spectra over 200 ns are shown for two levels of injection in Figure 6-23 (A-B).

By applying the appropriate injection ratio to achieve dual-λ operation it is evident from the images that emission of both wavelengths occurs simultaneously. This also holds true as the injection level is increased further as shown in second image. This rather compelling evidence for synchronised emission not only invokes intriguing questions on how dot states are populated but also on the potential applications, for example terahertz generation, which is left for discussion in the section on future work in Chapter 7.

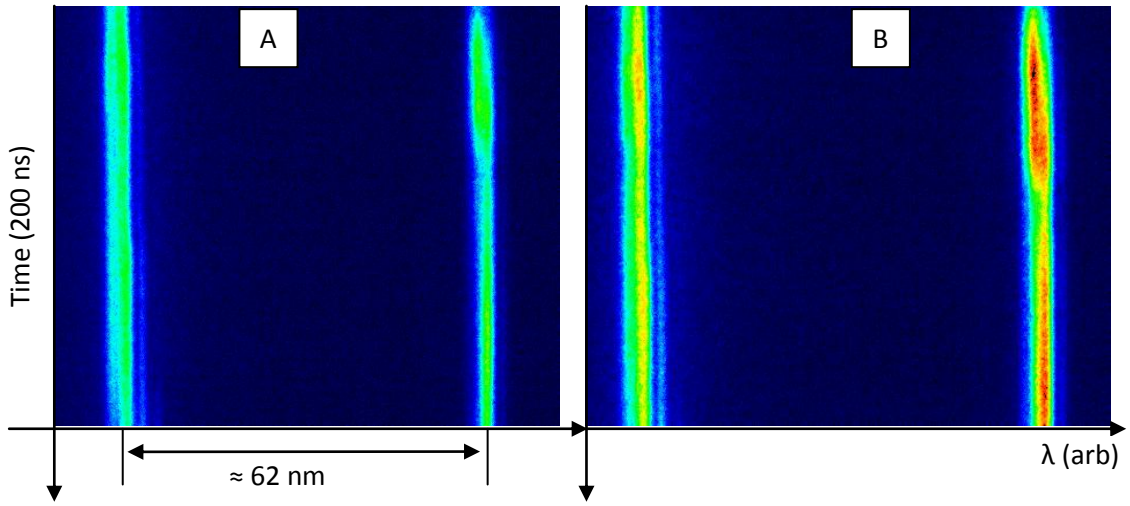

Figure 6-23: Time evolution of emission spectra when operating in dual-λ mode (A) and for increased injection (B).

As discussed earlier, the laser device can be operated with S1 acting as a saturable absorber. Under this regime the *P-I* characteristics were indicative of a Q-switched type behaviour, which under the right conditions, could also give rise to a *self-pulsating* lasing mode. To investigate this, time-resolved spectra were taken over a 20 ns period at a current which corresponds to the point in the *P-I* curve (Figure 6-19) where a sharp rise in the light level is observed. The image obtained from the Streak camera is shown in Figure 6-24, where clearly defined pulses are observed at a period of approximately 1.9 ns. A profile plot taken from a cross-section of the spectra, shown in Figure 6-25, illustrates the abrupt changes in the light level, which at its minima falls very close to the background level (indicated by the red line) signifying that the laser 'switches off' during the time between pulses. As the current is increased, above the 'kinked' feature in the *P-I* curve, the self-pulsing behaviour ceases and the light pulse returns to a relatively steady light level for the duration of the current pulse. Although the self-pulsating effect seen here is an interesting phenomenon, it was not the intended purpose of the device. As such, it has not been thoroughly investigated in this thesis. Despite this, the conditions that achieved self-pulsation here do provide useful information from which additional (optimised) devices could be fabricated. For example, it was realised that the most well defined pulses occurred when a small bias was applied to S1. If a self-pulsating device is required, then this immediately tells us that S1 is too absorbing at its current length. However, since it can be difficult to

estimate the appropriate length or ratio of section lengths, it is envisaged that by making S1 longer (more absorbing) than required, the optimal absorption can be achieved by simply biasing S1 until self-pulsation occurs.

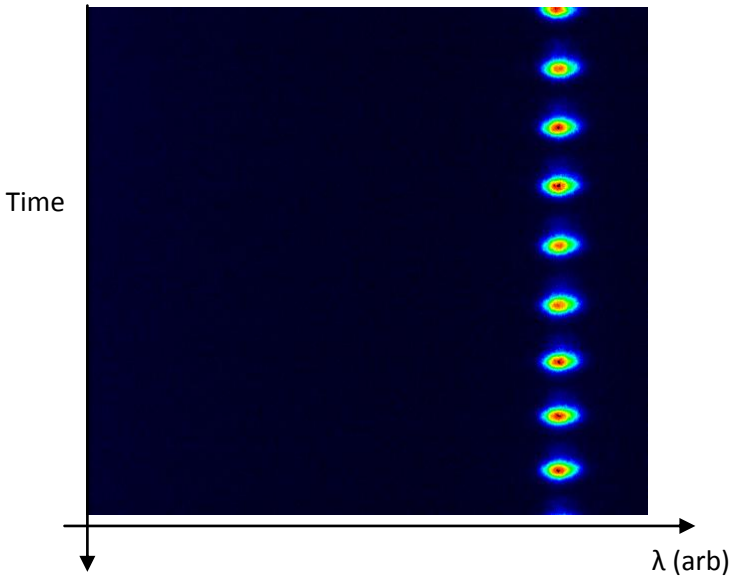

Figure 6-24: Streak camera image showing self-pulsation of the optical mode over a 20 ns window.

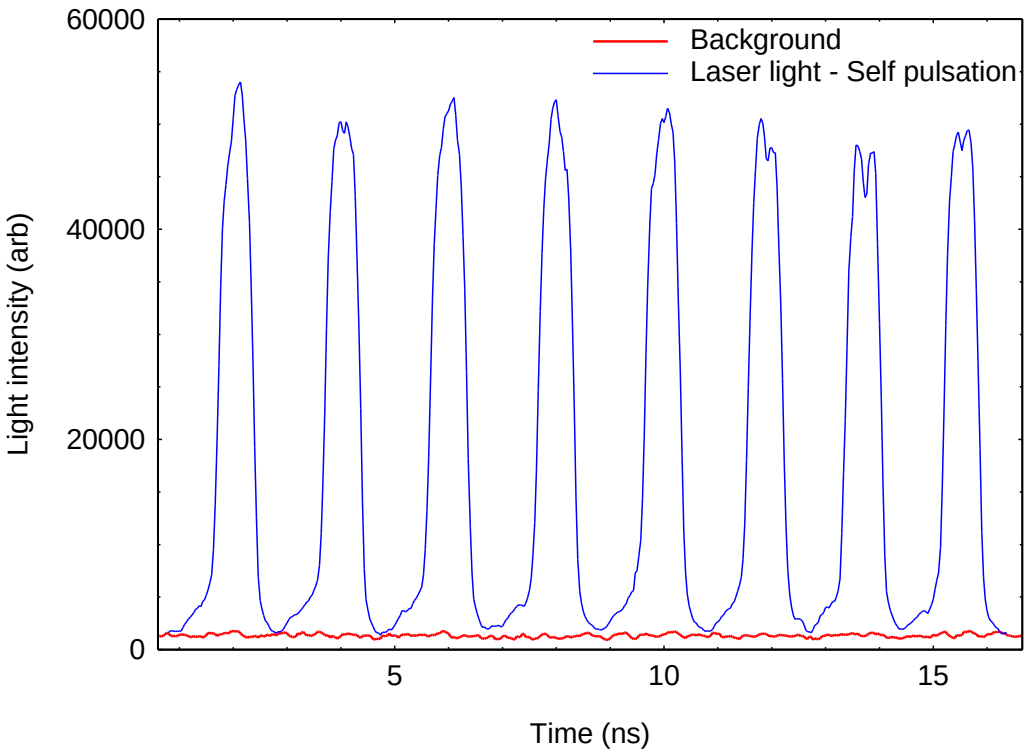

Figure 6-25: Profile plot of Streak camera image given in Figure 6-24 (Blue line) and background light level (red line)

6.5. Summary

This chapter described the process of developing a novel dual-λ laser based on the knowledge obtained through material characterisation (Chapter 5) and the developments made on fabricating submicron features in an InP/AlGaInP material system. At the beginning of the chapter it was explained how DBRs formed at the end of RWGs were used to blue-shift the operating wavelength without significantly affecting the threshold current density. Following this, the principle of how a coupled-cavity design with unequal length sections could be used to source multiple wavelengths was explained and measurements revealed that simultaneous dual-λ emission can be achieved using this method. A design improvement to the coupled-cavity design was then proposed which made use of DBR gratings placed between the two sections and at the rear of the longer section. The centre grating modified the loss spectrum of the cavity to provide preferential feedback at shorter wavelengths. The added advantage of the centre grating was that reflectance at long wavelengths was low, improving transmission of light from the longer section. A wavelength separation of 61.5 nm was achieved at 300 K and this was found to vary with temperature due to the different temperature dependence of each wavelength. This is a useful feature of the device, as the absolute separation can be controlled by varying the temperature.

Studies of the *P-I* characteristics were performed under three regimes of device operation. It was found that the current required to achieve threshold at the short wavelength was highest due to the level of inversion required to meet the gain requirement of the cavity. Driving the two sections together, to produce emission at the long wavelength only, required the lowest injection current of ≈ 20 mA at 25°C. In the third regime of operation, the contact to S1 was left floating so that it would act as a saturable-absorber for light entering from the second section. As expected, the threshold current was higher than it was when driving the two sections together due to the loss incurred by passive absorption of S1. The *P-I* curve was found to be reminiscent of that observed in a Q-switched device, with a sharp rise in the light level after threshold.

Finally, measurements were conducted to access the spatial and temporal coherence when in dual-mode operation. Near-field observations made in both the lateral and transverse directions show that the light from both optical modes is emitted in the same spatial region, but with a slightly asymmetric profile in the lateral direction. Within the resolution of the experiment, the two wavelengths appeared not be spatially separated, however the width of the RWG suggests that there are likely to be transverse spatial modes that are unresolved. The beam profiles obtained in the far-field were also found to be very similar and as a result the device presents itself as an attractive means to couple multiple wavelengths into a optical fibre or simple lens system. Temporal measurements also yielded interesting results with the two modes seen to be emitting simultaneously. This is a promising result as it tells us that quantum dots exhibit the characteristics necessary to fulfil the criteria of various device applications, in particular its potential use as a terahertz source. In addition, it has been demonstrated that the design of the device can be used to exploit the broad gain spectrum of the QD material to achieve a wide range of lasing wavelengths. In the context of the InP/AlGaInP wavelength regime (suitable for bio-medical applications), the device could be engineered to emit at, for example, the peak absorption wavelength of several different fluorescent dyes (e.g. Alexa Fluor series).

Chapter 7. Summary

7.1. Conclusions of this work

This thesis includes studies of the optoelectronic properties of InP-based quantum dot lasers structures and the development of a dry-etch process suitable for producing high aspect ratio sub-micron features. This enabled the design and fabrication of a monolithic dual-wavelength laser.

Using an Ar/Cl ICP gas composition and appropriate choice of RIE and ICP powers InP/ AlGaInP RWG structures were etched with vertical sidewalls to a depth of ≈ 5 µm. These process parameters could also be used to etch closely spaced high aspect ratio features in a single stage, which was not previously possible due the severe aspect-ratio dependent etching (ARDE) of the GaAs-cap. The maximum etch rate with this plasma chemistry was achieved at 220 °C and led to a reduction in the ARDE, which was ascribed to the enhanced removal of the etch product $InCl_3$. However, etching of laser devices was limited to 200 °C because above this the Ni used to form the etch mask inter-diffused with the GaAs-cap, and as a result could not be removed from the etched features. The etch recipe derived in this study proved to be a reliable etch process and was pivotal in fabricating the architecture of a dual-wavelength laser.

Chapter 5 described the work which has been carried out to establish a suitable epitaxial structure from which to fabricate multi-wavelength sources. It focussed on how changes in the growth temperature *(T_{gr})* and the epitaxial structure could be used to enhance device performance. In addition, the mechanisms responsible for the rise in threshold current with temperature were discussed, and the effect state filling can have on the gain-peak wavelength was explored.

The effect T_{gr} has on the nature of dot formation was studied using optical loss measurements. It was revealed that as T_{gr} increases there is a reduction in the density of the larger dots and this is accompanied by a shift in the dot states to higher energy. In terms of threshold current density, there was an improvement in

device performance with a reduction in the T_{gr} and this was true for a range of operating temperatures. Modal gain measurements made on the samples showed that the highest T_{gr} (750° C) had the lowest increase in gain with current. The modal gain of the samples grown at 710 and 730° C were very similar for each value of current injection and any difference in the threshold current densities of the lasers was attributed to the difference in internal optical loss (α_i) values. The measured α_i values were found to be 2.5 and 5 cm^{-1} for the samples grown at 710 and 730 °C respectively and 4.5 cm^{-1} for a T_{gr} of 750°C.

Whilst studying the origin of threshold current dependence, it was established that the major culprit responsible for the super-linear rise with temperature was the thermal spread of carriers between the ensemble of dot states, and any increase in the inhomogeneous broadening would exacerbate this effect. A sample with strain incorporated into the upper confining layer helped reduce the temperature dependence of the threshold current relative to an unstrained comparator sample, and this ascribed to a reduction in asymmetry between the conduction-valence bands. Improvement in threshold current was found to be most significant for short cavities. This is particularly beneficial when accessing short wavelengths as this requires very short sections where threshold currents are inherently high. In addition, it was found that the dot states in the strained sample were shifted to higher energies and this, together with the growth temperature, could be used to further extend the accessible range of lasing wavelengths. Taking into account all the structures tested in this work, a wavelength range extending from 655 to 740 nm could be achieved.

Over the temperature range investigated, the threshold current increased monotonically in all cases except with the 8 nm wide barrier sample grown at 750 °C. Here a rise and fall in the threshold current was observed between 200 and 260 K, before increasing again superlinearly. It was found that the level of injection did not follow this dependence, but instead increased almost linearly with temperature, similar to a comparator sample where the effect was not present. Measurements of spontaneous emission made over the temperature range of interest revealed that a thermal redistribution of carriers coincided with the fall in

threshold current above 260 K. This effect was observed for photon energies higher than those that contribute to the optical gain, and hence why there was no influence on the injection level dependence with temperature.

The final discussion on material characterisation was concerned with the effect that state-filling and temperature has on the gain-peak wavelength for the tensile strained sample. In the context of lasers which emit multiple wavelengths, it is important to quantify and understand how the stability of each wavelength will be governed by temperature. In addition it also revealed the range of wavelengths offered by the structure and this proved useful in designing the dual-wavelength laser.

At low injection it was observed that the temperature dependence followed that of the band-gap (≈ 17 nm/K) but became relatively insensitive to temperature as injection increased. In the sample tested, the minimum sensitivity corresponded to a net gain of ≈ 28 cm^{-1}. Based on these gain measurements a 400 µm long laser device with uncoated facets was demonstrated with a temperature dependence as low as 0.03 nm/K. Studies of the gain spectra showed that short cavities can be used to access short wavelengths (via the effects of state filling) and the added benefit is the enhanced wavelength stability. This is particularly important for sources which use spectrally preferential feedback. However, the compromise to be made here is the relatively high threshold currents.

Finally, Chapter 6 described the principle of using state filling to source two wavelengths from a coupled-cavity device with unequal length sections. The separation of emission wavelengths achieved using this design was 44 ±0.2 nm. By incorporating distributed Bragg reflectors (DBR)s into the structure, this separation could be extended to 61.5 ± 0.2 nm. The intention of placing a DBR grating between the two sections of the device was to modify the loss spectrum to provide preferential feedback at short wavelengths and provide a relatively low level of reflectance at long wavelengths. An additional grating placed at the rear of the device was intended to increase the feedback at long wavelengths.

Power-current *(P-I)* characteristics were obtained for three regimes of device operation. Due to the high level of inversion required to meet the gain requirement of the short section, it was found to have the highest threshold current and the lowest slope efficiency. Driving the two sections together gave a threshold current of ≈ 20 mA at 25° C, significantly lower than the simple coupled-cavity device. This improvement was attributed to the presence of the DBRs. In the third regime of operation the electrical contact to the short section was left floating so that it acted as a passive absorber for light entering from the longer section. As expected, this increased the threshold current, relative to driving both sections together, and the *P-I* characteristic was reminiscent of that observed in Q-switched devices.

Measurements were taken to assess the spatial and temporal coherence of each wavelength when in dual-mode operation. Near-field observations revealed that the emission at both wavelengths occurred within the same spatial region with a slight asymmetry in the lateral profile. The resulting far-field profiles were observed to have a Gaussian-like form, with characteristic FWHM values of 45 and 48 ± 1.5 ° for the long and short wavelengths, respectively. Finally, time resolved spectra were taken of a device operating with a wavelength separation of 61.5 nm using a streak camera system. It was found that emission at both wavelengths occurred simultaneously and this is a promising result as it suggests that this device could potentially be used as a compact terahertz source. , or explore the possibilities of using the device for biomedical imaging and sensing

By virtue of the inhomogenously broadened distribution of energy states offered by this material system and the relatively flat-topped gain spectrum, a wide range of operating wavelengths can be sourced. Although there is scope for enhancing device performance, a monolithic dual-wavelength laser has been demonstrated which fulfils the aims envisaged in the introduction to this thesis.

7.2. Future work

The goal of this PhD was to understand the optical properties of InP QD laser structures and use this knowledge to design and fabricate a novel dual-wavelength laser. Realising such a device has laid the foundation for further developments into

more specific applications. A multi-wavelength source can prove beneficial for a number of applications, such as those in bio-medical imaging and sensing (such as detecting oxygenation of haemoglobin and blood flow) [Qin et al. 2012; Allen et al. 2007]. Although it has many associated challenges, the potential to generate terahertz (THz) radiation is becoming an popular area of research for dual-wavelength diode lasers.

The range of frequencies referred to as THz is typically 0.1 - 10 THz, sandwiched between infra-red and microwaves. There are several high-impact applications including surveillance, security scanning, *in-vivo* biomedical imaging (e.g. for cancer diagnoses) and fast wireless communication. Although the technological potential of THz has been known for a number of years, it was too costly to exploit due to the limited available sources and only recently are devices now production, albeit in a limited niche of the market. One of the main producers of terahertz sources is Teraview Ltd, who has a number of patented technologies using both continuous wave (cw) and pulsed emission for a variety of imaging and detection applications.

Current methods of producing Terahertz commonly employ the use of photoconductive switches. These consist of a semiconductor which exhibits a short carrier lifetime, with high mobility and high resistivity, such as low temperature grown GaAs [McIntosh et al. 1995; Gregory et al. 2005], on which a metal strip-line is deposited with a small gap at the centre. A femto-second (fs) laser pulse impinging on the gap creates electro-hole pairs which are then accelerated to either section of the strip-line under an applied bias. This produces a sharp transient current which radiates terahertz. To generate appreciable powers, setups like this usually require the use of mainframe fs-lasers such as a titanium-sapphire (Ti:Sa), which are much more costly and less compact than diode lasers.

More recently, efforts have been made to enhance the efficiency of constant-wave (c.w.) terahertz photo-mixers by using nanogap electrodes as the active region of a photoconductive antenna [Tanoto et al. 2012]. Excitation of terahertz emission in these devices was generated using two separate DFB diode lasers tuned to slightly different wavelengths. Other promising sources of c.w. terahertz emission include

quantum cascade lasers (QCLs) [Kumar et al. 2011]. The lasers themselves have the advantage of being compact; the only issue is that these sources must be cryogenically cooled, which is costly and increases device footprint. Single edge-emitting diode lasers as well as VCSELs operating at two wavelengths capable of producing terahertz have also been investigated, and room temperature powers of tens of milliwatts have been reported [O'Brien et al. 2010; Schellar et al. 2010].

The premise of a potential future project envisaged here is to optimise the existing device for producing terahertz via a *difference-frequency generation* (DFG) method. The advantage of this monolithic device is that the wavelengths are emitted from the same active region and are concurrent both temporally and spatially, with emission from a common aperture. In the context of a terahertz generation, a single device avoids the issue of a drifting beat frequency associated with using separate sources. It also reduces the difficulty of aligning optics to couple the optical modes into a photomixer and the concomitant power loss.

Due to the complex non-linear interactions that occur in inside semiconductor lasers the concept of direct emission of terahertz has been explored [Hoffman et al 2004], but one of the major drawbacks of using this method is the low output power of ≈ 100 pW. However, this value is associated with lasers which were not optimised for THz generation. For efficient conversion to be achieved the THz mode must be positioned so that it has sufficient overlap with the optical mode and this involves careful waveguide design. This is a challenging problem to overcome, since the THz mode is not guided by the optical waveguide of the laser and is extended over a much larger region of space. This gives rise to strong absorption in the substrate of the laser structure and as such, the epitaxy must be grown on semi-insulating substrates if suitable power levels are to be reached. In addition to improving the overlap of the fields, a phase-matched condition between the two optical frequencies must be satisfied as well as a method of radiating the difference-mode from the device. One such method uses a metallic diffraction grating on the surface of the waveguide through which the terahertz is radiated [Afonenko et al. 2005]. It has been suggested that if all these factors can be addressed and a high power laser design is used, an improvement of 10^6 in the

output power could be possible which would yield an output power of ≈ 100 µW [Hoffman et al 2007].

The largest separation of wavelengths that has been achieved using this device would give a beat note of 40 THz. By virtue of the broad, relatively flat-topped gain spectrum, it should be possible to produce emission at a multitude of frequencies down to approximately 3 THz, by simply varying the section lengths and the Bragg frequency of the gratings. Since the temperature dependence of each wavelength is slightly different, fine tuning could be achieved by varying the temperature of the device using a thermo-electric cooler or alternatively via micro-heaters situated on each of the two sections [Kim et al].

Further device optimisation would also benefit from a waveguide modelling software package that can more accurately describe the nature of reflectivity and diffraction loss within the grating regions. In addition, it would useful to model the design criteria for optimising optical-to-terahertz conversion efficiency as well as exploring alternate device architectures such as those which incorporate laterally coupled (LC) DFBs.

With respect to the active QD material, it is intriguing to consider the process by which population dynamics can accommodate for the emission of multiple wavelengths, which are concurrent both spatially and temporally. Modelling this experimentally observed behaviour could provide some new insight into the fundamental physics of how dots are populated and the mechanisms of carrier recombination, with the endeavour to further enhance device performance.

Chapter 8. Appendix A

8.1. Laser fabrication process flow

Step	Process	Details
1	Cleave and clean samples	Trichloroethylene, Acetone, Methanol, IPA (hotplate at 80℃)
2	Spin on PMMA	6000rpm, 45s (950 K)
3	Bake PMMA	3min at 180℃
4	Expose Pattern in using EBL	
5	Develop	1 parts MIBK : 3 parts IPA (30 s)
6	Deposit Ni mask	~ 60 nm for deep etch ridges
7	Lift-off	Warm Acetone, clean in IPA
8	Etch sample in ICP	200 W RIE, 500 W ICP, 90% Ar 10% Cl_2 at 200℃
9	Ni etch	5% nitric acid and 95% DI water (2 min initially – inspect)
10	Descum in ICP (If required)	100 W RIE, 40 sccm O2 for 1 min at 25℃
11	Dehydration bake	2 min on hotplate at 100℃
12	Apply Adhesion promoter (AP3000)	Spread 200 rpm 5 s ramp to 2500 rpm 20 s
13	Spin on BCB (Cyclotene 3022)	spread 600 rpm 6 s ramp to 5000 rpm 30 s
14	Bake BCB	2 min on hotplate at 100℃
15	Soft Cure BCB in N_2 environment	Ramp temp slowly from 100℃ to 210℃, 40 min cure time
16	Back etch BCB in ICP	75W RIE, 1000 W ICP, 12 sccm C_4F_8, 28 sccm O_2, 25℃
17	Deposit Cr/Au p-contact	10 nm Cr, 200 nm Au.
18	Spin on photo-resist	6000 rpm, 45 s
19	Bake Photo-resist	3 min, 100℃
20	Expose 50 μm in between stripes	3.2 s
21	Develop	15 s (11/66 ml Microposit 2401/DI water)
22	Bake photo-resist	2 min on hotplate at 100℃
23	Au Etch	~1min
24	Remove photo-resist	Hot acetone for 5 - 10 min, clean in IPA
25	Fully Cure BCB	300℃ for 60 min
26	Lap sample	Achieve thickness of 100 μm
27	n-contact evaporation	100 nm AuGe, 28 nm Ni, 300 nm Au
28	Anneal contacts	355℃ for 3 min
29	Cleave into laser chips	

References

- Afenenko, A.A., Aleshkin, V.Y., Dubinov, (2005) "Parametric generation of a mid-infrared mode in semiconductor waveguides using a surface diffraction grating", Semiconductor science and technology, vol. 20 pp. 357-362.

- Al-Ghamdi, M.S, Smowton, P.M., Blood, P., (2011) “Dot Density Effect by Quantity of Deposited Material in InP/AlGaInP Structures”, IEEE Photonics Technology Letters, vol. 23, no. 16, 1169 - 1171

- Allen, J.T., Beard, P.C., "Dual wavelength laser diode excitation source for 2D photoacoustic imaging", Proceedings of the society of photo-optical instrumentation engineers (SPIE) vol. 6437.

- Asada, M., Miyamoto, Y., Suematsu, Y., (1986) "Gain and the Threshold of Three-Dimensional Quantum-Box Lasers" IEEE Journal of Quantum Electronics, vol. 22, no. 9, 1915 - 1921

- Avary, K., Rennon, S., Klopf, F., Reithmaier, J.P., Forchel, A., (2001) "Reactive ion etching of deeply etched DBR-structures with reduced air-gaps for highly reflective monolithically integrated laser mirrors", Microelectronic Engineering, vol. 57-59, 593-598.

- Blood, P. (1991) Heterostructures in semiconductor lasers, Chapter 7 in Physics and technology of Heterojunction devices, Edited by D.V. Morgan and R.H.Williams, Peter Perigrinas.

- Blood, P., Lewis, G.M, Smowton, P.M, Summers, H.D, Thomson, J.D and Lutti, J. (2003) “Characterisation of Semiconductor Laser gain Media by the Segmented Contact Method”, IEEE Journal of Selected Topics in Quantum Electronics, vol. 9, no. 5, 1275-1282.

- Blood, P., (2009) "Gain and recombination in quantum dot lasers", IEEE Journal of selected topics in quantum electronics, vol. 15, no. 3, 808 - 818

- Burrus, C.A., Linke, R.A., Kaminow, I.P., Ko, J.S., Dentai, A.G., Logan, R.A., Miller, B.I., (1983) "Short coupled-cavity (SCC) InGaAsP injection lasers for CW and high-speed single longitudinal mode operation", Electronics Letters vol. 19, no. 5, 561 – 562

- Capua, A., Rozenfeld, L., Mikhelashvili, V., Eisenstein, G., Kuntz, M., Laemmlin, M., Bimberg, D. (2007) “Direct correlation between a highly damped modulation response and ultra low relative intensity noise in InAs/GaAs quantum dot laser”, Optics Express, vol. 15, no. 9, 5388-5393

- Chin, D., Dhong, S.H., Long, G.J., (1986) "Structural effects on a submicron trench process", Journal of Electrochemical Society", vol. 132, no. 7, 1705-1707

- Coburn, J.W., Winters, H.F., (1979) "Plasma etching - A discussion of mechanisms", Journal of vacuum science and technology, vol. 16, no. 2, 391-403

- Coldren, L.A & Corzine, S.W., (1995) "Diode Lasers and Photonic Intergrated Circuits", Wiley series in Microwave and Optical Engineering.

- Crawford, M.H., Schneider, R.P., Jr., Choquette, K.D., Lear, K.L., (1995) "Temperature-dependent characteristics and single-mode performance of AlGaInP-based 670-690-nm vertical-cavity surface-emitting lasers," Photonics Technology Letters, IEEE , vol.7, no.7, 724-726

- Daghestani, N.S., Cataluna, M.A., Ross, G., Rose, M.J., (2011) "Compact Dual-Wavelength InAs/GaAs Quantum-Dot External-Cavity Laser Stabilized by a Single Volume Bragg Grating," Photonics Technology Letters, IEEE , vol. 23, no. 3, 176-178

- Deppe, D.G., Shavritranuruk, K., Ozgur, G., Chen, H., Freisem, S., (2009) "Quantum dot laser diode with low threshold and low internal loss," Electronics Letters , vol.45, no.1, 54-56

- Dogan, H., Yildirim, N., Turut, A., (2008) "Thermally annealed Ni/n-GaAs(si)/In Schottky barrier diodes", Microelectronic Engineering vol. 85, no. 4, 655-658.

- Edwards, G.T., Westwood, D.I., Smowton, P.M., (2006) "Selective etching of AlGaInP laser structures in a BCl_3/Cl_2 inductively coupled plasma", Semiconductor science and technology, vol. 21, no. 4, 513-519

- Edwards, G.T., (2007a) "The fabrication of deep-etched distributed Bragg reflectors in AlGaInP/GaAs laser structures", PhD Thesis, Cardiff University.

- Edwards, G.T., Sobiesierski, A., Westwood, D.I., Smowton, P.M., (2007b) "Fabrication of high-aspect-ratio, sub-micron gratings in AlGaInP/GaAs laser structures using a $BCl_3/Cl_2/Ar$ inductively coupled plasma", Semiconductor science and technology, vol. 22, no. 9, 1010-1015.

- Edwards, G.T., Smowton, P.M., Westwood, D.I., (2008) "Dry etching of anisotropic microstructures for distributed Bragg reflectors in AlGaInP/GaAs laser structures", IEEE Journal of Selected Topics in Quantum Electronics, vol. 14, no 4, 1098 - 1103

- Francis, D.A., Chang-Hasnain, C.J., Eason, K., (1996) “Effect of facet roughness on etched-facet semiconductor laser diodes”, Applied Physics Letters, vol. 68 no. 12, 1598 - 1600

- Elliott, N.S (2010) “High Power Semiconductor Lasers” PhD Thesis, Cardiff University

- Elliott, S.N., Smowton, P.M, Krysa, A.B., (2012) “Strained confinement layers in InP quantum dot lasers”, Novel In-Plane Semiconductor Lasers IX, Editors: Alexey A. Belyanin, Peter M. Smowton, Proceedings of the society of photo-optical instrumentation engineers (SPIE) vol. 8277

- Goldstein, L., Glas, F., Marzin, J.Y., Charasse, M.N., Le Roux, G., (1985) "Growth by molecular beam epitaxy and characterization of InAs/GaAs strained-layer superlattices", Applied Physics Letters, vol. 47, no. 10, 1099-1101,

- Gottsho, R.A., Jurgensen, C.W., Vitkavage, D.J., (1992) "Microscopic uniformity in plasma etching", Journal of Vacuum Science and Technology B, vol. 10, no. 5, 2133-2147

- Gregory, I.S., Baker, C., Tribe, W.R., Bradley, I.V., Evans, M.J., Linfield, E.H., Davies, A.G., Missous, M., (2005) "Optimization of photomixers and antennas for continuous-wave terahertz emission," Quantum Electronics, IEEE Journal of, vol. 41, no. 5, 717- 728

- Griffiths, K (1992) “Automated Laser Diode Measurements”, Mphil Thesis, UWCC

- Hamamatsu Photonics, K. K., systems division, “Guide to Streak Cameras” [online, cited: June 2012.] http://sales.hamamatsu.com/

- Hamilton, A. L., West, R. M., Briggs, M. S. J., Cummins, W. J. , and Bruce, I. E. (1997) "Squarate dyes and their use in fluorescent sequencing method". PCT Pat. WO 97/40104, (Amersham Int. plc)

- Hecht, E., "Optics", third edition, Addison Wesley Longman (1998).

- Hofmann, M.R., Hoffmann, S., (2007), “ Generation of Terahertz radiation with two color semiconductor lasers”, Laser and Photonics Rev., vol. 1, no. 1, 44-56.

- Hoffmann, S., Hofmann, M.R., Brundermann, E., Havenith, M., Matus, M., “ Four-wave mixing and direct terahertz emission with two-color semiconductor lasers”, Applied Physics Letters vol. 84, no. 18, 3585-3587.

- Jianglin, W., Hanyi, Z., Qun, W., Bingkun, Z., (1987) "Single-mode characteristics of short coupled-cavity semiconductor lasers", IEEE Journal of Quantum Electronics, Vol. QE-23, No. 6, 1005 - 1009

- Klopf, F., Deubert, S. Reithmaier, J. P., Forchel, A., (2002) “Correlation between the gain profile and the temperature-induced shift in wavelength of quantum-dot lasers” Applied Physics Letters, vol. 81, no. 2, 217 - 219

- Krysa, A.B., Liew, S.L., Lin, J.C., Roberts, J.S., Lutti, J., Lewis, G.M. and Smowton, P.M., (2007) “Low threshold InP/AlGaInP on GaAs QD laser emitting at similar to 740 nm”, *J. Cryst. Growth,* vol. 298, 663-666

- Kumar, S., Wang, C., Chang, I., Hu, Q., Reno, L.J., (2011) "A 1.8-THz quantum cascade laser operating significantly above the temperature of ω/kB", Nature Physics vol. 7, 166-171

- Kuntz, M., Fiol, G., Laemmlin, M., Meuer, C., Bimberg, D., (2007) "High-Speed Mode-Locked Quantum-Dot Lasers and Optical Amplifiers", Proceedings of IEEE, vol. 95, no. 9, 11767-1778,

- Liu, G.T., Stintz, A., Li, H., Malloy, K.J., Lester, L.F., (1999) "Extremely low room-temperature threshold current density diode lasers using InAs dots in In0.15Ga0.85As quantum well", Electronics Letters, vol. 35, no. 14, 1163-1165

- Lutti. J, (2005) “Optical properties of InP/AlGaInP quantum dot laser heterostructures”, PhD Thesis, Cardiff University

- Manz, Y.M., Schmidt, O. G., Eberl, K., (2000) “Room temperature lasing via ground state of current injected vertically aligned InP/GaInP quantum dots”, Applied Physics Letters, vol. 76, no. 23, 3343-3345

- Matsuura, S., Tani, M., Sakai, K., (1997) "Generation of coherent terahertz radiation by photomixing in dipole photoconductive antennas", Applied Physics Letters, , vol. 70, no. 5, 559-561.

- McIntosh, K. A., Brown, E. R., Nichols, K. B., McMahon, O. B., DiNatale, W. F., Lyszczarz, T. M., (1995) "Terahertz photomixing with diode lasers in low-temperature-grown GaAs," Applied Physics Letters , vol.67, no.26, 3844-3846

- Naderi, N.A., Grillot, F., Yanf, K., Wright, J.B., Gin, A., Lester, L.F., (2010) “Two-color multi-section quantum dot distributed feedback laser”, Optics Express vol. 18, no. 26, 27028-27035

- Naidu, D., Smowton, P.M., Summers, H.D., (2010). "Carrier injection-level dependence of lateral ambipolar diffusion in S-K quantum-dot lasers", Semiconductor Laser Conference (ISLC), 2010 22nd IEEE International, 67-68

- O'Brien, S., Osborne, S., Bitauld D., Brandonisio, N., Amann, A., (2010), "Optical Synthesis of Terahertz and Millimeter-Wave Frequencies With Discrete Mode Diode Lasers," Microwave Theory and Techniques, IEEE Transactions on , vol.58, no.11, pp.3083-3087.

- Oswald, B., Lehmann F., Simon, L., Terpetschnig, E. and Wolfbeis, O.S. (2000) "Red Laser-Induced Fluorescence Energy Transfer in an Immunosystem" Analytical Biochemistry vol. 280**,** 272–277

- Ogawa, M., (1980) "Alloying reaction in thin nickel films deposited on GaAs", Thin Solid Films, vol. 70, no. 1, 181-189.

- Pozzi, F., De La Rue, R.M., Sorel, M., (2006) " Dual-Wavelength InAlGaAs–InP Laterally Coupled Distributed Feedback Laser", IEEE Photonics Technology Letters, vol. 18, no. 24, 2563 - 2565

- Price, R.K., Verma, V.B., Tobin, K.E., Elarde, V.C., Coleman, J.J., (2007) "Y-Branch Surface-Etched Distributed Bragg Reflector Lasers at 850 nm for Optical Heterodyning," Photonics Technology Letters, IEEE , vol. 19, no. 20, 1610-1612

- Qin, J., Reif, R., Zhi, Z., Dziennis, S., Wang, R., (2012) "Hemodynamic and morphological vasculature response to a burn monitored using a combined dual-wavelength laser speckle and optical microangiography imaging system", Biomedical Optics Express, vol. 3, no. 3

- Raffaele, L., De La Rue, R.M., Roberts, J.S., Krauss, F.T., (2001) “Edge-emitting semiconductor microlasers with ultrashort-cavity and dry-etched high-reflectivity photonic microstructure mirrors”, IEEE photonics technology letters, vol. 13, no. 3, 176 - 178

- Rai-Choudhury, P. (Editor) (1997) “Handbook of Microlithography, Micromachining and Fabrication”. SPIE, Volume 1: Microlithography

- Reithmaier, J.P., Forchel, A., (2002) "Single-mode distributed feedback and microlasers based on quantum-dot gain material", IEEE Journal of selected topics in quantum electronics, vol. 8, no. 5, 1035-1044

- Roh, S.D., Swint, R.B., Jones, A.M., Yeoh, T.S., Huber, A.E., Hughs, J.S., Coleman, J.J., (1999) "Dual-wavelength asymmetric cladding InGaAs-GaAs ridge waveguide distributed Bragg reflector lasers", IEEE Photonics Technology Letters, vol. 11, no. 1, 15 - 17

- Sadick, S.N., (2002), "A dual wavelength approach for laser/intense pulsed light source treatment of lower extremity veins", Journal of American Academy of dermatology vol. 46, no. 1, 66-72.

- Saito, H., Nishi, K.m Kamei, A., Sogou, S., (2000) "Low Chirp Observed in Directly Modulated QuantumDot Lasers", Photonic Technology Letters, vol. 12, no. 10, 1298 - 1300

- Scheller, M., Yarborough J.M., Moloney, J.V., Fallahi, M., Koch, M., Koch, S.W., (2010) "Room temperature continuous wave milliwatt terahertz source", Optics Express vol. 18, no. 26, 27112-27117.

- Smowton, P.M., Lutti, J., Lewis, G.M., Krysa, A.B., Roberts, J.S., and Houston, P.A., (2005) “InP-GaInP Quantum-Dot Lasers Emitting Between 690-750 nm”, IEEE Journal of Selected Topics in Quantum Electronics, vol. 11, no 5, 1035 - 1040

- Smowton, P.M., Sandell, I.C, Mowbray, D.J., Liu, H.Y., Hopkinson, M., (2007) “Temperature-Dependent Gain and Threshold in P-Doped Quantum Dot Laser”, IEEE Journal of Selected Topics in Quantum Electronics, vol. 13, no 5, 1261 - 1266

- Smowton, P.M., Al-Ghamdi, M.S., Shutts, S., Edwards, G., Hutchings, M., Krysa, A.B., (2010) "Effect of Growth Temperature on InP QD Lasers," *Photonics Technology Letters, IEEE* , vol. 22, no. 2, 88-90

- Smowton, P.M., Elliott, S.N., Shutts, S., Al-Ghamdi, M.S., Krysa, A.B., (2011) “Temperature-Dependent Threshold Current in InP Quantum-Dot Lasers”, IEEE Journal of Selected Topics in Quantum Electronics, vol. 17, no 5,

- Tanoto, H., Teng, J.H., Wu, Q.Y., Sun, M., Chen, Z.N., Maier, S.A., Wang, B., Chum, C.C., Si, G.Y., Danner, A.J., Chua, S.J. (2012) "Greatly enhanced continuous-wave terahertz emission by nano-electrodes in a photoconductive photomixer", Nature Photonics vol. 6, 121-126

- Thomas L. Paoli, (1997) "Multiple wavelength, surface emitting laser with broad bandwidth distributed Bragg reflectors", US Patent 5699375

- Thomas, R., (2012) “Monolithic coupled-cavity laser diodes for bio-sensing application”, PhD Thesis, Cardiff University

- Thomson, J. D., Summers, H. D., Hulyer, P. J., Smowton, P. M., and Blood, P. (1999) “Determination of single-pass optical gain and internal optical loss using a multisection device”, Applied Physics Letters, vol. 75, no. 17, 2527-2529

- Thomson, J. D., Summers, H. D., Smowton, P. M., Hermann, E., Blood, P, and Hopkinson, M., (2001) “Temperature dependence of the lasing wavelength of InGaAs quantum dots”, Journal of applied physics, vol. 90, no. 9, 4859-4861

- Tsang, W.T., Olsson, N.A., Logan, R.A., (1983) "High-speed direct single-frequency modulation with large tuning rate and frequency excursion in cleaved-coupled-cavity semiconductor lasers", Applied Physics Letters, vol. 42 no. 8

- Ustinov, V.M., Zhukov, A.E., Egorov A. Yu., Maleev, N.A., (2003) “Quantum Dot Lasers”, Oxford University Press, Oxford

- Walter, G., Elkow, J., Holonyak, N., Heller, R. D., Zhang, X.B., Dupuis, R.D., (2004), "Visible spectrum (645 nm) transverse electric field laser operation of InP quantum dots coupled to tensile strained $In_{0.46}Ga_{0.54}P$ quantum wells," Applied Physics Letters , vol.84, no.5, pp.666-668

- Williams, R.E, Gallium Arsenide Processing Techniques, Artech House, Inc., Dedham, Massachusetts, U.S.A. (1984)

- Yablonovitch, E., and Kane, E.O., (1986) “Reduction of lasing threshold current density by the lowering of valence band effective mass”, Journal of Lightwave Technology, vol. 4, no. 5, 504 - 506

- Yuan, Y., Brock, T., Bhattacharya, P., Caneau, C., Bhat, R., (1997) “Edge-emitting lasers with short-period semiconductor/air distributed Bragg reflector mirrors”, IEEE photonics technology letters, vol. 9, no. 7

- Zundel, M.K., Jin-Phillipp, N.Y., Phillipp, F., Eberl, K., Riedl, T., Fehrenbacher, E. and Hangleiter, A., (1998) “Red-light-emitting injection laser based on InP/GaInP self assembled quantum dots”, Applied Physics Letters, vol. 73, no. 13, 1784-1786

Conferences

- Shutts, S., Al-Ghamdi, M.S., Edwards, G., Smowton, P.M., (2009) The Origin of the Temperature Dependence of Threshold Current Density in InP/AlGaInP QD Laser Structures", Semiconductor and Integrated OptoElectronics (SIOE) Conference 2009

- Shutts, S., Edwards, G., Elliott, S.N., Smowton, P.M., (2011) "Deep etched Distributed Bragg Reflector (DBR) InP / AlGaInP Quantum Dot Lasers", Photonics West 2011, San Francisco, California, USA

- Shutts, S., Edwards, G., Elliott, S.N., Smowton, P.M., (2011) "Deep etched Distributed Bragg Reflector (DBR) InP / AlGaInP Quantum Dot Lasers", Semiconductor and Integrated OptoElectronics (SIOE) Conference 2011

- Shutts, S., Smowton, P.M., (2012) "Temperature Dependence of λ in InP Quantum Dot Lasers", Semiconductor and Integrated OptoElectronics (SIOE) Conference 2012

- Shutts, S., Smowton, P.M., (2012) "Achieving temperature-insensitive λ in InP quantum dot lasers", International Semiconductor Laser Conference (ISLC), 2012 23rd IEEE International

- Shutts, S., Smowton, P.M., (2012) "Dual-λ InP/AlGaInP quantum dot laser", International Semiconductor Laser Conference (ISLC), 2012 23rd IEEE International

Publications

- Smowton, P.M., Al-Ghamdi, M.S., Shutts, S., Edwards, G., Hutchings, M., Krysa, A.B., (2010) "Effect of Growth Temperature on InP QD Lasers," *Photonics Technology Letters, IEEE* , vol. 22, no. 2, 88-90

- Smowton, P.M., Elliott, S.N., Shutts, S., Al-Ghamdi, M.S., Krysa, A.B., (2011) “Temperature-Dependent Threshold Current in InP Quantum-Dot Lasers”, IEEE Journal of Selected Topics in Quantum Electronics, vol. 17, no 5,

- Smowton, P.M., Al-Ghamdi, M., Edwards, G., Shutts, S., Krysa, A.B. (2009) "InP quantum dot 7xxnm laser diodes", Nanotechnology, 2009. IEEE-NANO 2009, 9th IEEE Conference, 508-509